

UNCLASSIFIED

AD NUMBER

ADB005697

LIMITATION CHANGES

TO:

Approved for public release; distribution is unlimited.

FROM:

Distribution authorized to U.S. Gov't. agencies only; Test and Evaluation; JUL 1975. Other requests shall be referred to Air Force Armament Lab., Eglin AFB, FL.

AUTHORITY

AFATL ltr 21 Dec 1977

THIS PAGE IS UNCLASSIFIED

AUG 13 1975

OCT 15 1975
NOV 26 1976
MAY 11 1979

Cy2



**AERODYNAMIC INTERFERENCE EFFECTS ON VARIOUS
WEAPON SHAPES IN THE FLOW FIELD OF
A TRANSONIC WING CONFIGURATION AT
MACH NUMBERS FROM 0.5 TO 1.3**

MAR 21 1991

**PROPULSION WIND TUNNEL FACILITY
ARNOLD ENGINEERING DEVELOPMENT CENTER
AIR FORCE SYSTEMS COMMAND
ARNOLD AIR FORCE STATION, TENNESSEE 37389**

TECHNICAL REPORTS

July 1975

Final Report

Final Report for Period December 9, 1974 — March 4, 1975

This document has been approved for public release

its distribution is unlimited. TAB 78-12 6/9/78

Distribution limited to U.S. Government agencies only; this report contains information on test and evaluation of military hardware; July 1975; other requests for this document must be referred to Air Force Armament Laboratory (AFATL/DLJC), Eglin Air Force Base, Florida 32542.

Prepared for

**AIR FORCE ARMAMENT LABORATORY (AFATL/DLJC)
EGLIN AIR FORCE BASE, FLORIDA 32542**

PROPERTY OF U. S. AIR FORCE
AEDC LIBRARY
F49600-75-C-0001

NOTICES

When U. S. Government drawings specifications, or other data are used for any purpose other than a definitely related Government procurement operation, the Government thereby incurs no responsibility nor any obligation whatsoever, and the fact that the Government may have formulated, furnished, or in any way supplied the said drawings, specifications, or other data, is not to be regarded by implication or otherwise, or in any manner licensing the holder or any other person or corporation, or conveying any rights or permission to manufacture, use, or sell any patented invention that may in any way be related thereto.

Qualified users may obtain copies of this report from the Defense Documentation Center.

References to named commercial products in this report are not to be considered in any sense as an endorsement of the product by the United States Air Force or the Government.

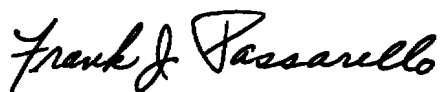
APPROVAL STATEMENT

This technical report has been reviewed and is approved for publication.

FOR THE COMMANDER



LAMAR R. KISSLING
Lt Colonel, USAF
Chief Air Force Test Director, PWT
Directorate of Test



FRANK J. PASSARELLO
Colonel, USAF
Director of Test

UNCLASSIFIED

REPORT DOCUMENTATION PAGE		READ INSTRUCTIONS BEFORE COMPLETING FORM
1 REPORT NUMBER AEDC-TR-75-92 AFATL-TR-75-88	2 GOVT ACCESSION NO.	3 RECIPIENT'S CATALOG NUMBER
4 TITLE (and Subtitle) AERODYNAMIC INTERFERENCE EFFECTS ON VARIOUS WEAPON SHAPES IN THE FLOW FIELD OF A TRANSONIC WING CONFIGURATION AT MACH NUMBERS FROM 0.5 TO 1.3	5 TYPE OF REPORT & PERIOD COVERED Final Report, Dec 9, 1974 - Mar 4, 1975	
	6 PERFORMING ORG REPORT NUMBER	
7 AUTHOR(s) G. R. Mattasits, ARO, Inc.	8 CONTRACT OR GRANT NUMBER(s)	
9 PERFORMING ORGANIZATION NAME AND ADDRESS Arnold Engineering Development Center (XO) Arnold Air Force Station, TN 37389	10 PROGRAM ELEMENT, PROJECT TASK AREA & WORK UNIT NUMBERS Program Element 62602F Project 2567 Task 02	
11 CONTROLLING OFFICE NAME AND ADDRESS Air Force Armament Laboratory (AFATL/DLJC) Eglin Air Force Base, FL 32542	12 REPORT DATE July 1975	
	13 NUMBER OF PAGES 132	
14 MONITORING AGENCY NAME & ADDRESS (if different from Controlling Office)	15 SECURITY CLASS (of this report) UNCLASSIFIED	
	15a DECLASSIFICATION DOWNGRADING SCHEDULE N/A	
16 DISTRIBUTION STATEMENT (of this Report) Distribution limited to U.S. Government agencies only; this report contains information on test and evaluation of military hardware; July 1975; other requests for this document must be referred to Air Force Armament Laboratory (AFATL/DLJC), Eglin Air Force Base, Florida 32542.		
17 DISTRIBUTION STATEMENT (of the abstract entered in Block 20, if different from Report)		
18 SUPPLEMENTARY NOTES Available in DDC.		
19 KEY WORDS (Continue on reverse side if necessary and identify by block number) <div style="display: flex; justify-content: space-between;"> <div style="width: 45%;"> aircraft separation interference flow fields aerodynamic characteristics </div> <div style="width: 45%;"> test methods transonic flow M-117 bomb maximum volume bomb </div> </div>		
20 ABSTRACT (Continue on reverse side if necessary and identify by block number) Tests were conducted in the Aerodynamic Wind Tunnel (4T) to evaluate the validity of weapon aerodynamics acquired from theoretical calculations which employed mathematical models to simulate actual test hardware and to assess the problems encountered during the separation of various weapon shapes, at transonic flight conditions, from the number one TER position. The data will also be used to aid in the development of a mathematical		

UNCLASSIFIED

UNCLASSIFIED

20. ABSTRACT (Continued)

method for predicting store separation characteristics. Data were obtained at Mach numbers from 0.5 to 1.3. Force and pressure distribution measurements were obtained to assess the influence of angle of attack and both linear and angular store displacements from the carriage position. Store models were separated from a TER mounted on the inboard pylon of a half-span wing similar in planform to the wing of the F-4 aircraft. Data were obtained on 0.10-scale models of the M-117 and maximum volume bombs. Test results showed that large nose-down pitching-moment coefficients were encountered by all store models at the number one TER carriage position. Complete separation trajectories were obtained only at a Mach number of 0.5 for all 16-in.-diam store models. Decreasing store model diameter increased the maximum Mach number at which complete trajectories were obtained.

UNCLASSIFIED

PREFACE

The work reported herein was conducted by the Arnold Engineering Development Center (AEDC), Air Force Systems Command (AFSC), at the request of the Air Force Armament Laboratory (AFATL/DLJC), AFSC, under Program Element 62602F. AFATL Project Monitor was Capt. V. Arajs. The results presented were obtained by ARO, Inc. (a subsidiary of Sverdrup & Parcel and Associates, Inc.), contract operator of AEDC, AFSC, Arnold Air Force Station, Tennessee, under ARO Project No. P41C-63A. The author of this report was G. R. Mattasits, ARO, Inc. The manuscript (ARO Control No. ARO-PWT-TR-75-67) was submitted for publication on May 23, 1975.

CONTENTS

	<u>Page</u>
1.0 INTRODUCTION	7
2.0 APPARATUS	
2.1 Test Facility	7
2.2 Test Articles	8
2.3 Instrumentation	9
3.0 TEST DESCRIPTION	
3.1 Test Conditions	9
3.2 Data Acquisition	10
3.3 Corrections	11
3.4 Precision of Data	11
4.0 RESULTS AND DISCUSSION	
4.1 Free-Stream Data	13
4.2 Induced Aerodynamic Loads Data	13
4.3 Trajectory Data	16
4.4 Induced Aerodynamic Pressure Data	17
5.0 SUMMARY OF RESULTS	18
REFERENCES	19

ILLUSTRATIONS

Figure

1. Isometric Drawing of a Typical Store Separation Installation and Block Diagram of the Computer Control Loop Used During Captive Trajectory Testing	21
2. Schematic of the Tunnel Test Section Showing Model Location	22
3. Details and Dimensions of the Force and Moment Models	23
4. Details and Dimensions of the Pressure Distribution Models	26
5. Details and Dimensions of the Geometrically Scaled Triple Ejection Rack Model	28
6. Details and Dimensions of the Mathematically Simulated Triple Ejection Rack Model	29
7. Details and Dimensions of the F-4 Inboard Pylon Model	30
8. Details and Dimensions of the Flat-Plate, Half-Wing Model	31
9. Photograph of a Typical Test Configuration Installed in the Tunnel	32
10. Free-Stream Force Data for the M-117 Bombs, $\Delta\phi = 0$	33

<u>Figure</u>	<u>Page</u>
11. Free-Stream Force Data for the Maximum Volume Bombs, $\Delta\phi = 0$	35
12. Free-Stream Pressure Distribution Data for the M-117 Bombs	38
13. Free-Stream Pressure Distribution Data for the Maximum Volume Bombs	40
14. Carriage Position Airloads of the Standard M-117 Bomb Configuration in the Flow Field of the Isolated Simulated TER, $\Delta\phi = 0$	43
15. Carriage Position Airloads of the Standard M-117 Bomb Configuration in the Flow Field of the Isolated Geometrical TER, $\Delta\phi = 0$	44
16. Carriage Position Airloads of the Standard M-117 Bomb Configuration in the Flow Field of the Wing-Pylon (without TER) Configuration, $\Delta\phi = 0$	45
17. Carriage Position Airloads of the M-117 Bombs in the Flow Field of the Wing-Pylon-TER Configuration, $\Delta\phi = 0$	46
18. Carriage Position Airloads of the Maximum Volume Bombs in the Flow Field of the Wing-Pylon-TER Configuration, $\Delta\phi = 0$	48
19. Oil-Flow Visualization Photograph of a Standard M-117 Bomb Configuration in the Flow Field of a Wing-Pylon-TER Configuration, $\alpha = 0$, $M_\infty = 0.9$	51
20. Carriage Position Airloads of the M-117 Bombs in the Flow Field of the Wing-Pylon-TER Configuration, $\Delta\phi = 45$ deg	52
21. Carriage Position Airloads of the 14-in.-diam Maximum Volume Bomb in the Flow Field of the Wing-Pylon-TER Configuration, $\Delta\phi = 45$ deg	54
22. Carriage Position Airloads of the M-117 Bombs in the Flow Field of the Wing-Pylon-TER Configuration, $\Delta\phi = 0$, $\alpha = 5$ deg	55
23. Carriage Position Airloads of the Maximum Volume Bombs in the Flow Field of the Wing-Pylon-TER Configuration, $\Delta\phi = 0$, $\alpha = 5$ deg	57
24. Carriage Position Airloads of the 12-in.-diam Maximum Volume Bomb with Fuse, in the Flow Field of the Wing-Pylon-TER Configuration, $\Delta\phi = 0$	60
25. Grid Survey Airloads of the Standard M-117 Bomb Configuration in the Flow Field of the Wing-Pylon (without TER) Configuration, $\Delta\phi = 0$	62

Figure**Page**

26. Grid Survey Airloads of the Standard M-117 Bomb Configuration in the Flow Field of the Wing-Pylon-TER Configuration, $\Delta\phi = 0$	65
27. Grid Survey Airloads of the Modified M-117 Bomb Configuration in the Flow Field of the Wing-Pylon-TER Configuration, $\Delta\phi = 0$	68
28. Grid Survey Airloads of the 16-in.-diam Maximum Volume Bomb in the Flow Field of the Wing-Pylon-TER Configuration, $\Delta\phi = 0$	71
29. Grid Survey Airloads of the 14-in.-diam Maximum Volume Bomb in the Flow Field of the Wing-Pylon-TER Configuration, $\Delta\phi = 0$	74
30. Grid Survey Airloads of the 12-in.-diam Maximum Volume Bomb in the Flow Field of the Wing-Pylon-TER Configuration, $\Delta\phi = 0$	77
31. Grid Survey Airloads of the 14-in.-diam Maximum Volume Bomb in the Flow Field of the Wing-Pylon-TER Configuration, $\Delta\phi = 0$, $Z/D = 0.5$	80
32. Grid Survey Airloads of the 14-in.-diam Maximum Volume Bomb in the Flow Field of the Wing-Pylon-TER Configuration, $\Delta\phi = 0$, $Z/D = 1.0$	82
33. Effects of Roll Orientation on the Normal-Force and Pitching-Moment Coefficients of the Standard M-117 Bomb Configuration	84
34. Effects of the FMU-110 Fuse on the Normal-Force and Pitching-Moment Coefficients of the 12-in.-diam Maximum Volume Bomb	85
35. Trajectory Data for the Standard M-117 Bomb Configuration	86
36. Trajectory Data for the Modified M-117 Bomb Configuration	88
37. Trajectory Data for the 16-in.-diam Maximum Volume Bomb	90
38. Trajectory Data for the 14-in.-diam Maximum Volume Bomb	92
39. Trajectory Data for the 12-in.-diam Maximum Volume Bomb	95
40. Pressure Distribution Data on the Standard M-117 Bomb Configuration at the Number One Carriage Position of the Wing-Pylon-TER Configuration	99
41. Pressure Distribution Data on the Modified M-117 Bomb Configuration at the Number One Carriage Position of the Wing-Pylon-TER Configuration	101
42. Pressure Distribution Data on the 16-in.-diam Maximum Volume Bomb at the Number One Carriage Position of the Wing-Pylon-TER Configuration	103
43. Pressure Distribution Data on the 14-in.-diam Maximum Volume Bomb at the Number One Carriage Position of the Wing-Pylon-TER Configuration	105

<u>Figure</u>	<u>Page</u>
44. Pressure Distribution Data on the 12-in.-diam Maximum Volume Bomb at the Number One Carriage Position of the Wing-Pylon-TER Configuration	107
45. Pressure Distribution Data on the 12-in.-diam Maximum Volume Bomb at the Number One Carriage Position of the Wing-Pylon-TER Configuration, $\alpha = 5$ deg	109
46. Effects of Store Pitch Incidence Angle for the Standard M-117 Bomb Configuration, $M_\infty = 0.5$	111
47. Effects of Store Pitch Incidence Angle for the Standard M-117 Bomb Configuration, $M_\infty = 0.9$	113
48. Effects of Store Pitch Incidence Angle for the Standard M-117 Bomb Configuration, $M_\infty = 1.1$	115
49. Effects of the FMU-110 Fuse on the 12-in.-diam Maximum Volume Bomb, $M_\infty = 0.5$	117
50. Effects of the FMU-110 Fuse on the 12-in.-diam Maximum Volume Bomb, $M_\infty = 0.9$	119
51. Effects of the FMU-110 Fuse on the 12-in.-diam Maximum Volume Bomb, $M_\infty = 1.1$	121

TABLES

1. Store Trajectory Test Conditions	123
2. Aerodynamic Loads Test Conditions	124
3. Aerodynamic Pressure Test Conditions	125
4. Identification of Full-Scale Store Parameters	127

NOMENCLATURE	128
------------------------	-----

1.0 INTRODUCTION

The Air Force Armament Laboratory (AFATL) has sponsored a continuing program to evaluate the aerodynamic characteristics of bodies in a complex flow field. Given in Ref. 1 are data obtained for the M-117 bomb at various store locations and orientations relative to an isolated triple ejection rack (TER). This report presents test results which are an extension of that work and which were obtained in the Aerodynamic Wind Tunnel (4T) of the Propulsion Wind Tunnel Facility (PWT). The validity of weapon aerodynamic characteristics in a complex flow field acquired from theoretical calculations was investigated during both wind tunnel tests. However, the present test investigated not only the aerodynamic flow field induced by an isolated TER but also the aerodynamic flow field induced by a TER mounted on a pylon of a half-span wing similar to the wing of an F-4 aircraft. The wing design, a flat plate with rounded leading edge and tapered trailing edge, was chosen to simplify fabrication requirements. The wing planform was that of the actual F-4 wing with the span extended to the point of intersection of the leading and trailing edges. The extended wing span, in conjunction with the inboard end plate, gave an effective aspect ratio equal to that of the actual F-4 wing.

Aerodynamic characteristics of 1/10-scale models of various weapon shapes were obtained at Mach numbers from 0.5 to 1.3. Free-stream aerodynamic loads and pressure distribution data were obtained for all store models at angles of attack from -20 to 20 deg. Induced aerodynamic loads and pressure distribution data were obtained at angles of attack of 0 and 5 deg. Separation trajectories were obtained for a simulated altitude of 5,000 ft at an angle of attack of zero.

2.0 APPARATUS

2.1 TEST FACILITY

Tunnel 4T is a closed-loop, continuous flow, variable density tunnel in which the Mach number can be varied from 0.1 to 1.3. At all Mach numbers, the stagnation pressure can be varied from 300 to 3700 psfa. The test section is 4 ft square and 12.5 ft long with perforated, variable porosity (0.5- to 10-percent open) walls. It is completely enclosed in a plenum chamber from which the air can be evacuated, allowing part of the tunnel airflow to be removed through the perforated walls of the test section. A more thorough description of the tunnel is given in Ref. 2.

For store separation and aerodynamic grid survey testing, two separate and independent support systems are used to support the models. The parent aircraft model is inverted in the test section and supported by an offset sting attached to the main pitch sector. The store model is supported by the captive trajectory support (CTS) which

extends down from the tunnel top wall and provides store movement (6 deg of freedom) independent of the parent-aircraft model. An isometric drawing of a typical store separation installation is shown in Fig. 1. For the present test, the parent aircraft model consisted of a half-span wing only.

Also shown in Fig. 1 is a block diagram of the computer control loop used during captive trajectory testing. The analog system and the digital computer work as an integrated unit and, utilizing required input information, control the store movement during a trajectory. Store positioning is accomplished by use of six individual d-c electric motors. Maximum translational travel of the CTS is ± 15 in. from the tunnel centerline in the lateral and vertical directions and 36 in. in the axial direction. Maximum angular displacements are ± 45 deg in pitch and yaw and ± 360 deg in roll. A more complete description of the test facility can be found in Ref. 2. A schematic showing the test section details and the location of the models in the tunnel is shown in Fig. 2.

2.2 TEST ARTICLES

During both aerodynamic loads and pressure distribution data acquisition phases, 1/10-scale models of the M-117 bomb (standard and modified boattail) and the maximum volume bombs (16-in., 14-in., and 12-in. diam) were used. Details and dimensions of the force models are shown in Fig. 3. At zero roll orientation, the fins on all force models were at 45 deg with respect to the Y_p - Z_p axis system (e.g., Fig. 3b). Also shown, in Fig. 3c, are both the FMU-56 and FMU-110 fuse shapes which were used in conjunction with both force and pressure models of the maximum volume bombs. Presented in Fig. 4 are the details and dimensions of the pressure distribution models. The pressure models were unfinned and had 25 pressure orifices distributed along their length. At zero roll orientation, the pressure orifices were adjacent to the pylon or TER surface. Two geometric configurations were used as models of the TER: one which represented the true physical geometry and another, a body of revolution, which was used to generate a flow field similar to that of the actual TER. Details and dimensions of these two TER configurations are given in Figs. 5 and 6, respectively.

A major portion of the test was conducted using the geometric TER mounted on a pylon on the flat-plate, half-wing configuration which simulated the F-4 aircraft wing with inboard pylon. Details and dimensions of the pylon and wing are shown in Figs. 7 and 8, respectively. A photograph of this test configuration installed in the tunnel is shown in Fig. 9. In this photograph, the store models are mounted at the 45-deg roll orientation.

2.3 INSTRUMENTATION

2.3.1 Captive Trajectory and Aerodynamic Loads Survey Phase

A 0.75-in.-diam, six-component, internal strain-gage balance was used to measure aerodynamic loads acting on the store models. Translational and angular positions of the store models were obtained from the CTS analog outputs.

The pylon and TER were instrumented with a spring-loaded plunger (touch wire) which extended approximately 0.10 in. below the pylon or rack surface, to provide an indication of when the store was in its carriage position. This system was electrically wired to give a visual indication on the control console when contact between the store model and touch wire was made. The system was also electrically connected to automatically stop the CTS movement if the store model or its sting support contacted the rack, pylon, wing, or its support structure.

2.3.2 Aerodynamic Pressure Survey Phase

Static pressures along the length of the store models were measured using 15-psid transducers which were referenced to the tunnel plenum chamber static pressure (approximately equal to free-stream static pressure). Store movements and positioning were accomplished in the same manner as for the captive trajectory and aerodynamic loads survey phase.

3.0 TEST DESCRIPTION

3.1 TEST CONDITIONS

Data were obtained at Mach numbers from 0.5 to 1.3 while the tunnel dynamic pressure varied from 150 to 620 psf. The wing-model angle of attack was set at 2 or 7 deg, resulting in TER and store angles of 0 or 5 deg, respectively. Wind tunnel test conditions were held constant at the desired Mach number and dynamic pressure while data were obtained. Data acquisition terminated automatically during the grid surveys when data from the preselected model positions and attitudes were obtained. Trajectories were terminated manually when sufficient data were obtained, when the CTS reached a travel limit, or when the store or its support sting contacted the wing or its support structure. A summary of trajectory test conditions at which data were obtained is presented in Table 1. A summary of aerodynamic loads and pressure surveys at which data were obtained is presented in Tables 2 and 3, respectively.

3.2 DATA ACQUISITION

To obtain captive trajectory and aerodynamic grid survey data, test conditions were established in the tunnel and the parent model was positioned at the desired angle of attack. The store model was then oriented to a position corresponding to the store carriage location. After the store was set at the desired initial position, operational control of the CTS was switched to the digital computer, which controlled the store movement through commands to the CTS analog system (see block diagram, Fig. 1). Data from the wind tunnel, consisting of measured model forces and moments, measured model static pressures, wind tunnel operating conditions, and CTS rig positions, were input to the digital computer for use in the full-scale calculations.

During captive trajectory data acquisition, the digital computer was programmed to solve the (6-deg-of-freedom) equations to calculate the angular and linear displacements of the store relative to the parent aircraft pylon. In general, the program involves using the last two successive measured values of each aerodynamic coefficient to predict the magnitude of the coefficients over the next time interval of the trajectory. These predicted values are used to calculate the new position and attitude of the store at the end of the time interval. The CTS is then commanded to move the store model to this new position and the aerodynamic loads are measured. If these new measurements agree with the predicted values, the process is continued over another time interval of the same magnitude. If the measured and predicted values do not agree within the desired precision, the calculation is repeated over a time interval one-half the previous value. This process is repeated until a complete trajectory has been obtained.

When the wind tunnel data are applied to the calculations of the full-scale store trajectories, the measured forces and moments are reduced to coefficient form and then applied with proper full-scale store dimensions and flight dynamic pressure. Dynamic pressure was calculated using a flight velocity equal to the free-stream velocity component plus the components of store velocity relative to the aircraft, and a density corresponding to the simulated altitude.

The initial portion of each launch trajectory incorporated simulated ejector forces in addition to the measured aerodynamic forces acting on the store. The ejector force was 1200 lb acting over a distance of 0.255 ft, full scale. The ejector force was considered to act perpendicular to the rack or pylon mounting surface. The locations of the applied ejector forces and other full-scale store parameters used in the trajectory calculations are listed in Table 4.

3.3 CORRECTIONS

3.3.1 Captive Trajectory and Aerodynamic Loads Survey Phase

Balance, sting, and support deflections caused by the aerodynamic loads on the store models were accounted for in the data reduction program to calculate the true store-model angles. Corrections were also made for model weight tares to calculate the net aerodynamic forces on the store model.

3.3.2 Aerodynamic Pressure Survey Phase

Support deflections caused by the aerodynamic loads on the wing were accounted for during the positioning of the wing to the desired angle of attack.

3.4 PRECISION OF DATA

Estimated uncertainties in store-model positioning resulting from the ability of the CTS to set on a specified value were ± 0.05 in. for translational settings, ± 0.15 deg in pitch and yaw, and ± 1.0 deg in roll. The Mach number was held constant within ± 0.005 of the quoted Mach number with an estimated uncertainty of ± 0.003 .

3.4.1 Aerodynamic Loads Survey

Uncertainties in the aerodynamic coefficient data were calculated taking into consideration the probable inaccuracies in the balance measurements and tunnel conditions. The uncertainties in the coefficients are based on a 95-percent confidence level, ignoring bias errors, and are as follows:

<u>Store</u>	<u>ΔC_N</u>	<u>ΔC_Y</u>	<u>ΔC_A</u>	<u>ΔC_l</u>	<u>ΔC_m</u>	<u>ΔC_n</u>
M-117	± 0.007	± 0.008	± 0.01	± 0.004	± 0.01	± 0.009
16-in.-diam Maximum Volume	± 0.007	± 0.008	± 0.01	± 0.004	± 0.01	± 0.007
14-in.-diam Maximum Volume	± 0.008	± 0.010	± 0.02	± 0.006	± 0.02	± 0.010
12-in.-diam Maximum Volume	± 0.009	± 0.020	± 0.02	± 0.009	± 0.03	± 0.020

The uncertainty in setting wing-model angle of attack was ± 0.1 deg. However, at a wing angle of attack of 7 deg (TER angle of 5 deg), bias errors attributable to aerodynamic loading of the wing were estimated to be on the order of 0.3 deg.

3.4.2 Captive Trajectory Data

Extrapolation tolerances in the trajectory integration procedure were ± 0.1 for all aerodynamic coefficients. Estimates of the uncertainties in the trajectory data attributable to balance precision limitations were made for the store models at given times in the trajectory and were found to be as follows:

Store	t, sec	ΔX_P , ft	ΔY_P , ft	ΔZ_P , ft	$\Delta \theta$, deg	$\Delta \psi$, deg	$\Delta \phi$, deg
M-117	0.2	± 0.01	± 0.006	± 0.003	± 0.3	± 0.2	± 1.0
	0.4	± 0.04	± 0.02	± 0.01	± 1.0	± 0.7	± 5.0
16-in.-diam							
Maximum Volume	0.2	± 0.009	± 0.006	± 0.003	± 0.2	± 0.1	± 1.0
	0.4	± 0.04	± 0.02	± 0.01	± 0.9	± 0.5	± 5.0
14-in.-diam							
Maximum Volume	0.2	± 0.01	± 0.007	± 0.004	± 0.3	± 0.2	± 2.0
	0.4	± 0.05	± 0.03	± 0.02	± 1.0	± 0.7	± 8.0
12-in.-diam							
Maximum Volume	0.2	± 0.02	± 0.01	± 0.006	± 0.4	± 0.2	± 3.0
	0.4	± 0.07	± 0.04	± 0.02	± 2.0	± 1.0	± 14.0

The uncertainty in setting wing-model angle of attack was estimated to be ± 0.1 deg with a bias error attributable to aerodynamic loads at 0 angle of attack on the order of 0.1 deg.

3.4.3 Aerodynamic Pressure Phase

Uncertainties in the data were calculated taking into consideration the probable inaccuracies in the pressure transducer measurements and tunnel conditions. The uncertainties in the pressure coefficients are based on a 95-percent confidence level, ignoring bias errors, and are as follows:

M_∞	0.5	0.8	0.9	1.10	1.30
ΔC_P	± 0.020	± 0.007	± 0.006	± 0.005	± 0.004

Pressures were monitored in order to obtain the appropriate lag times, which were used to set data acquisition time intervals. These time intervals allowed pressure transducer stabilization to occur before data were recorded. The estimated uncertainty in setting angle of attack was ± 0.1 deg. Estimates of aerodynamic wing loading were used to eliminate bias errors in setting angle of attack during this phase of testing.

4.0 RESULTS AND DISCUSSION

4.1 FREE-STREAM DATA

Free-stream force data for the M-117 and maximum volume bombs are presented in Figs. 10 and 11, respectively, as a function of store-model angle of attack. Nonlinear variations of C_N and C_m with respect to angle of attack are evident for all Mach numbers. Static margins of the M-117 store models were approximately one caliber, whereas the static margins of the maximum volume bombs increased from approximately 0 to 0.8 calibers as body diameter decreased. These static margins are based on the cg locations given in Table 2.

Longitudinal pressure distribution data obtained with each pressure model in the free stream at $\alpha = 0$ are presented in Figs. 12 and 13. The flow expansion which occurs on the standard M-117 configuration at an X/L value of 0.48 is eliminated by use of the modified boattail. The overexpansion of the flow on the hemisphere nose and the local shock wave formation at an X/L value of 0.2 on the 16-in.-diam pressure model at a Mach number of 0.9 are attenuated with decreasing model diameter. Similar, but less pronounced, effects are also present at Mach numbers of 0.5 and 1.1. Although no explanation of this change is available based on the present data, the effect is similar to that seen on smooth spheres in subsonic flow with similar variations in Reynolds number (150,000 to 400,000, based on diameter).

4.2 INDUCED AERODYNAMIC LOADS DATA

The M-117 model was tested with two boattail geometries. One of these theoretically reduces store separation trajectory problems encountered at the number one station of the TER at transonic flight speeds by eliminating flow separation over the store afterbody. This should make the tail section more aerodynamically effective. The maximum volume bombs were tested with and without the two fuse shapes shown in Fig. 3c.

4.2.1 Carriage Position Data

Presented in Figs. 14 through 24 are data obtained on all store models at the number one TER carriage position. Aerodynamic coefficients for the standard M-117 configuration

in the flow field of the isolated (without the wing-pylon configuration) simulated and geometrical TER shapes are presented in Figs. 14 and 15, respectively, as a function of Mach number. The data presented in Fig. 15 were taken from Ref. 1. A comparison of the data indicates that there are differences between the loads measured near the simulated TER model and those measured near the geometrical TER model at the number one carriage position.

Shown in Fig. 16 are the aerodynamic coefficients of the standard M-117 configuration at the carriage position on the pylon (without TER) of the wing as a function of Mach number. No large force or moment coefficients can be seen throughout the Mach number range.

Aerodynamic coefficients as a function of Mach number for the M-117 and maximum volume bombs at the number one carriage position of the geometrical TER shape mounted on the pylon of the wing are shown in Figs. 17 and 18, respectively. Unlike the pylon carriage configuration, the normal-force, pitching-moment, side-force, and yawing-moment coefficients exhibit large variations with increasing Mach number. This is the apparent result of induced aerodynamic interactions plus local shock wave formations between the rack components. An analogy can be made between the large nose-down pitching-moment coefficients seen at Mach numbers above 0.5 and the oil-smear flow visualization photograph shown in Fig. 19. This photograph shows large aerodynamically induced downwash at the nose accompanied by upwash on the tail of the M-117 bomb at the number one TER carriage position. The photograph was obtained from tests conducted by and at the Air Force Academy.

The effect of altering the boattail of the M-117 bomb is shown in Fig. 17. A significant effect in the yawing-moment coefficient can be seen although the anticipated reduction of the negative pitching-moment coefficient does not occur. Store model body diameter effects are shown in Fig. 18. Again, the magnitude of the negative pitching-moment coefficients is not significantly affected even though the normal-force coefficients change drastically as the store diameter is decreased at the higher Mach numbers.

The large negative pitching-moment coefficients which occur for all store body shapes would seem to indicate that body geometry is not a predominant factor in producing the pitching-moment coefficients at the number one TER carriage position.

Data were obtained for both of the M-117 shapes and the 14-in.-diam maximum volume bomb at the number one TER carriage position with $\Delta\phi = 45$ deg (fins parallel to the Y_P and Z_P coordinate axes). These data are presented in Figs. 20 and 21 as a function of Mach number. A comparison of these data with data given in Figs. 17

and 18 ($\Delta\phi = 0$) shows only small variations in aerodynamic coefficients with the exception of normal-force coefficients for the 14-in.-diam store model.

Airloads data for all store models at 5 deg angle of attack are presented in Figs. 22 and 23. These data, compared with data given in Figs. 17 and 18 ($\alpha = 0$), show decreased negative pitching-moment coefficients for all store models at the carriage position. Increasing angle of attack alters the induced aerodynamic flow field about the store in the number one TER carriage position. Data obtained in this induced flow field, Fig. 23, show that pitching-moment coefficients become sensitive to changes in body diameter. In general, normal-force coefficients did not increase with increasing angle of attack but did show a reduction in their variation with increasing Mach number.

The effects of the two fuse shapes (see Fig. 3c) on the aerodynamic characteristics of the 12-in.-diam maximum volume bomb are presented in Fig. 24 as a function of Mach number. The addition of the FMU-110 fuse reduced the nose-down pitching-moment coefficients at the carriage position at all Mach numbers. Similar effects were seen on the 16-in.-diam bomb; however, no effects of the fuses were seen on the 14-in.-diam bomb.

4.2.2 Grid Survey Data

Presented in Figs. 25 through 34 are data obtained on store models at various vertical and angular displacements relative to the number one TER carriage position. Typical of the aerodynamic coefficient data obtained on the standard M-117 configuration in the flow field of the wing plus pylon (without TER) are the plots presented in Fig. 25. The data are shown as a function of store pitch incidence angle at various Z/D values. The aerodynamic coefficients were relatively insensitive to changes in Z/D . Data at subsonic Mach numbers were close to free-stream values. Changes in some aerodynamic coefficients at supersonic Mach numbers can be seen.

Aerodynamic coefficient data obtained for each store model in the flow field of the TER mounted on the pylon of the wing are shown in Figs. 26 through 30. Again, the data are given for various Z/D values as a function of store pitch incidence angle. Unlike data obtained near the carriage position of the pylon alone, these data show variations in all aerodynamic coefficients with changes in store vertical displacement. Nose-down pitching-moment coefficients increased as the store approached the number one TER carriage position. Data obtained at Mach numbers greater than 0.5, $\Delta\theta = 0$, show that the largest positive normal-force coefficient occurred at a Z/D value of 0.5 and not at the carriage position.

A comparison of data in Figs. 26 and 27 shows that the modified M-117 boattail did not produce any general improvement of the large nose-down pitching-moment

coefficients which occurred at and near the carriage position. However, a reduction in the axial-force coefficient is evident at all Mach numbers; this would seem to indicate that the M-117 boattail modification did alter the flow over the store afterbody.

Angle-of-attack effects for the 14-in.-diam maximum volume bomb displaced vertically from the carriage position can be seen in Figs. 31 and 32. The decreased normal-force and pitching-moment coefficients typify the effects of increased angle of attack on all store models.

Data obtained near the carriage position showing the effects of roll orientation are presented in Fig. 33 as a function of Mach number. These data are for the M-117, standard boattail store model but are representative of data obtained for both the M-117, modified boattail, and the 14-in.-diam maximum volume bomb. Changing $\Delta\phi$ from 0 to 45 deg produced a decrease in both the normal-force and pitching-moment coefficients. Other aerodynamic coefficients were relatively insensitive to roll and therefore are not presented.

Fuse effects near the carriage position are shown in Fig. 34 as a function of Mach number. Data are given only for the 12-in.-diam maximum volume bomb with and without the FMU-110 fuse. These data show that reduced normal-force and pitching-moment coefficients were obtained with the addition of the FMU-110 fuse; similar effects were seen for the 16-in.-diam bomb, while no effects were seen for the 14-in.-diam bomb. The FMU-56 fuse produced little, if any, effects on the aerodynamic characteristics of the maximum volume bombs.

4.3 TRAJECTORY DATA

Shown in Figs. 35 through 39 are the trajectory data for all store models. Test conditions and full-scale store parameters are identified in Tables 1 and 4. The 16-in.-diam store models were found to separate only at a Mach number of 0.5. The 14-in.-diam store model separated at Mach numbers of 0.5 and 0.8, and the 12-in.-diam store model separated for Mach numbers from 0.5 to 0.9. The inability of the stores to release cleanly from the number one TER position was a result of large angular pitch rates which increased as the Mach number was increased. The rapid pitch resulted in contact between the released store and the adjacent stores.

Major factors which influenced the above store separation characteristics are the pitch inertia and the pitch-damping derivative. With these parameters in mind, a review of the store properties given in Table 4, along with the data presented in Figs. 17 and 18, indicate that the largest nose-down pitching-moment coefficient allowable to obtain store separation without impingement would be no greater than -1.1 for releases up to Mach number 0.9 at an altitude of 5,000 ft.

4.4 INDUCED AERODYNAMIC PRESSURE DATA

Aerodynamic pressure distribution data were obtained in order to verify theoretical pressure distributions from which the theoretical store aerodynamic forces and moments and separation characteristics were calculated. Grid surveys were used to obtain pressure distributions around the store model in 45-deg increments from -135 to 180 deg at and near the number one TER carriage position. Pressure distribution data shown in Figs. 40 through 51 were obtained in the flow field of the geometrical TER mounted on the pylon of the wing configuration.

4.4.1 Carriage Position Data

Pressure coefficient data for each model at selected Mach numbers are given in Figs. 40 through 44. Pressure coefficient data obtained at $\Delta\phi = 180$ deg (pressure orifices away from the TER) show relatively small deviations from those pressure coefficients obtained in the free stream. However, pressure coefficients obtained at $\Delta\phi = 0$ (pressure orifices adjacent to the TER) show large differences from the pressure coefficients obtained in the free stream. Pressure coefficients obtained on the top surface are larger at the nose of the model than those seen on the bottom surface. These pressure differentials increase with increasing Mach number and give rise to large nose-down pitching moments, similar to those which were observed in the force and moment data. Large top-to-bottom pressure differentials are also seen between X/L values of 0.2 and 0.5. However, the forces associated with these differentials are centered about the cg and, therefore, have little effect on the pitching-moment characteristics.

Presented in Fig. 45 are the pressure coefficient distributions of the 12-in.-diam maximum volume bomb at an angle of attack of 5 deg. Unlike data obtained at an angle of attack of zero, these data show that increasing the Mach number did not cause large increases in the pressure differentials at the model nose. The reduced pressure differential at the model nose decreased the nose-down pitching moment and correlated well with trends observed in the force and moment data.

4.4.2 Grid Survey Data

Effects of store pitch incidence angle at a vertical displacement of 0.5 body diameters on the M-117, standard boattail pressure model are shown in Figs. 46 through 48. Decreasing the store incidence angle produced an increase in the pressure differential between the top and bottom surfaces at X/L values from 0 to 0.2. This increase was primarily responsible for both the increased pitching-moment and decreased normal-force coefficients which were seen in the force and moment data. The remaining pressure models showed similar incidence angle effects.

A comparison of these data and the data presented in Fig. 40 shows that the pressure differentials for X/L values from 0 to 0.2 were indeed larger at the carriage position than the pressure differentials obtained away from the carriage position. Therefore, larger nose-down pitching-moment coefficients at the carriage position would be expected.

Presented in Figs. 49 through 51 are the pressure coefficient distributions obtained on the 12-in.-diam maximum volume bomb pressure model with and without the FMU-110 fuse at a Z/D value of 0.5. The data show that the flow generally decelerated around the model nose due to the addition of the fuse. The deceleration was more pronounced on the bottom surface ($\Delta\phi = 180^\circ$), contributing to the reduction of the nose-down pitching-moment coefficient which was seen in the force and moment data.

5.0 SUMMARY OF RESULTS

Results of an investigation of aerodynamic loads and pressure distributions on the M-117 bomb and maximum volume bomb store models in the flow field of a triple ejection rack (TER) on a simulated aircraft wing are as follows:

1. Data obtained with the M-117, standard boattail store model at the number one carriage position of the geometrical TER shape exhibited trends similar to data obtained for the same store model at the number one carriage position of the simulated TER shape, although coefficient magnitudes differed.
2. Neither the M-117 boattail alteration nor the maximum volume bomb body-diameter variations significantly reduced the large nose-down pitching-moment coefficients encountered at the number one TER carriage position.
3. Data obtained at the number one TER carriage position indicated that increasing wing angle of attack caused a reduction in nose-down pitching-moment coefficients for all store models. This reduction increased as the model diameter was decreased.
4. Data obtained at and near the carriage position showed that the addition of the FMU-110 fuse to the 16-in.-diam and 12-in.-diam maximum volume bombs caused the normal-force and pitching-moment coefficients to decrease. Negligible effects were seen on the 14-in.-diam model.
5. Decreased nose-down pitching-moment coefficients accompanied increased vertical displacements from the carriage position.

6. Large outboard side-force coefficients developed at a TER angle of attack of 5 deg for data obtained on store models away from the carriage position.
7. Pressure coefficient data showed that the nose-down pitching-moment coefficients were due in large part to large pressure differentials that occurred near the model nose. These pressure differentials increased as the Mach number increased and the vertical displacement decreased.
8. Complete separation trajectories were obtained only at a Mach number of 0.5 for all 16-in.-diam store models. The 14-in.-diam store model separated for Mach numbers of 0.5 and 0.8. The 12-in.-diam store model separated for Mach numbers from 0.5 to 0.9.
9. The inability of store models to separate cleanly from the number one TER position was a result of large angular pitch rates.

REFERENCES

1. Summers, W. E. "Aerodynamic Loads Data on the M-117 Bomb in the Flow Field of the Triple Ejection Rack at Mach Numbers from 0.5 to 1.3." AEDC-TR-72-81 (AD894886L), June 1972.
2. Test Facilities Handbook (Tenth Edition). "Propulsion Wind Tunnel Facility, Vol. 4." Arnold Engineering Development Center, May 1974.

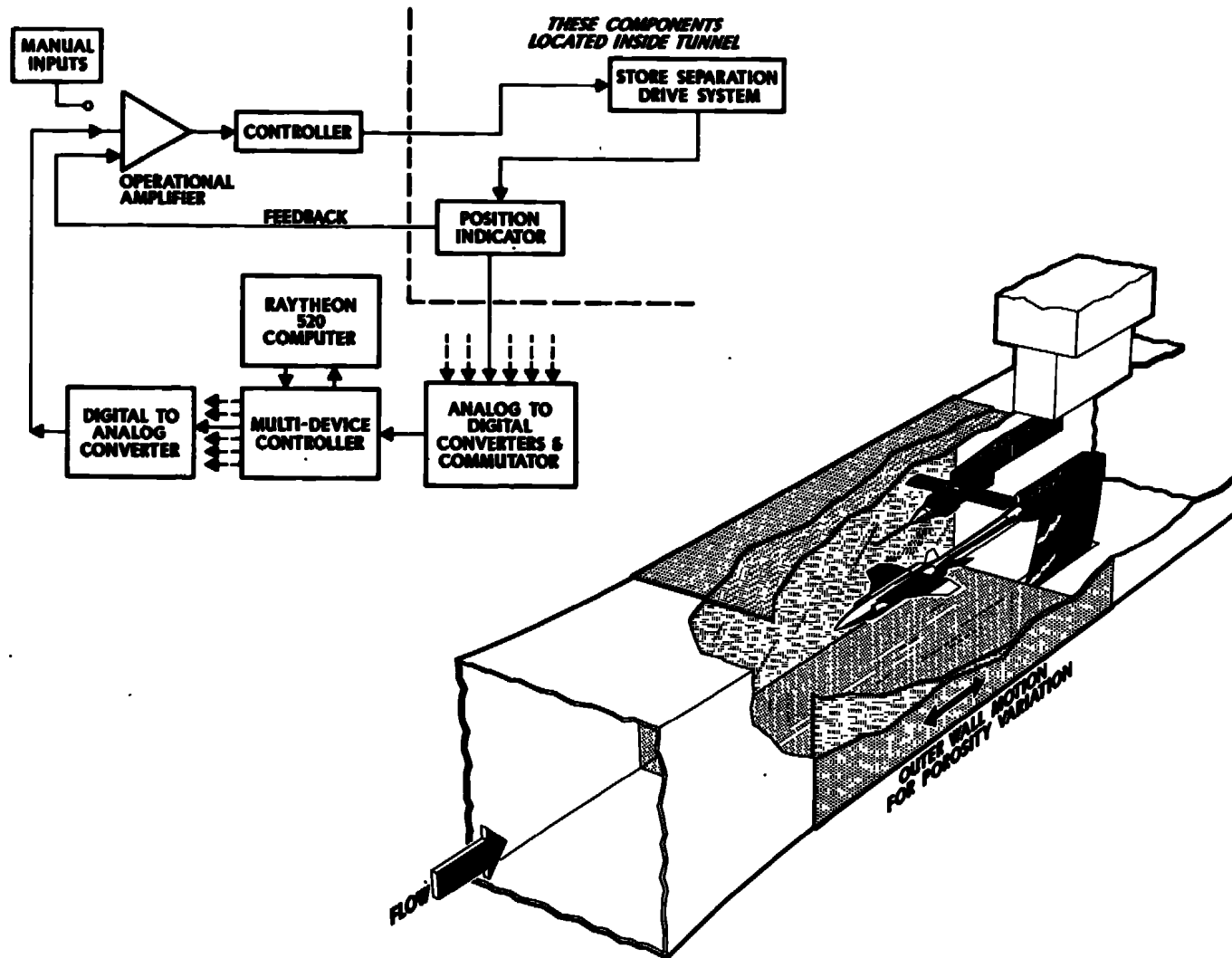


Figure 1. Isometric drawing of a typical store separation installation and block diagram of the computer control loop used during captive trajectory testing.

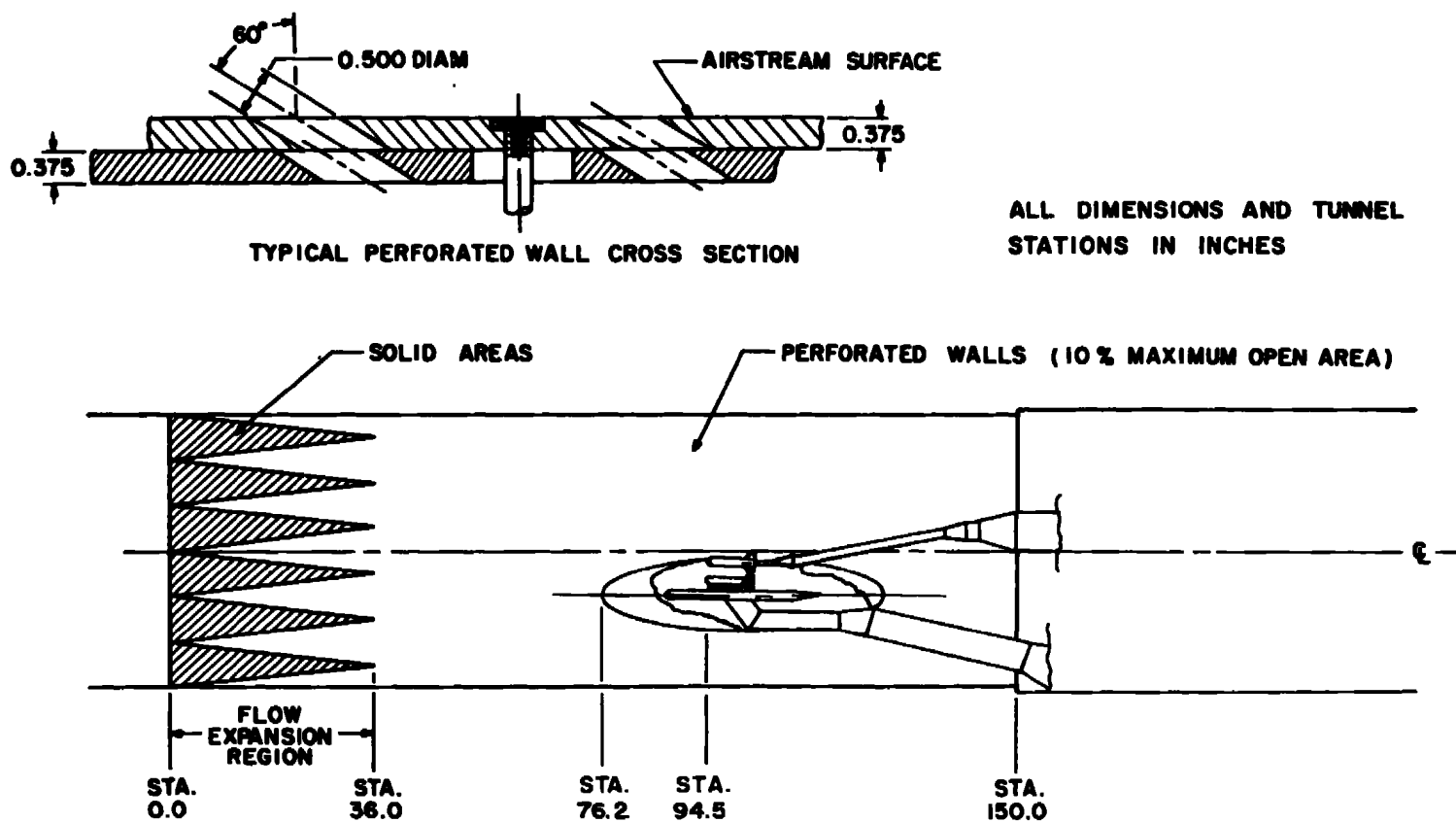
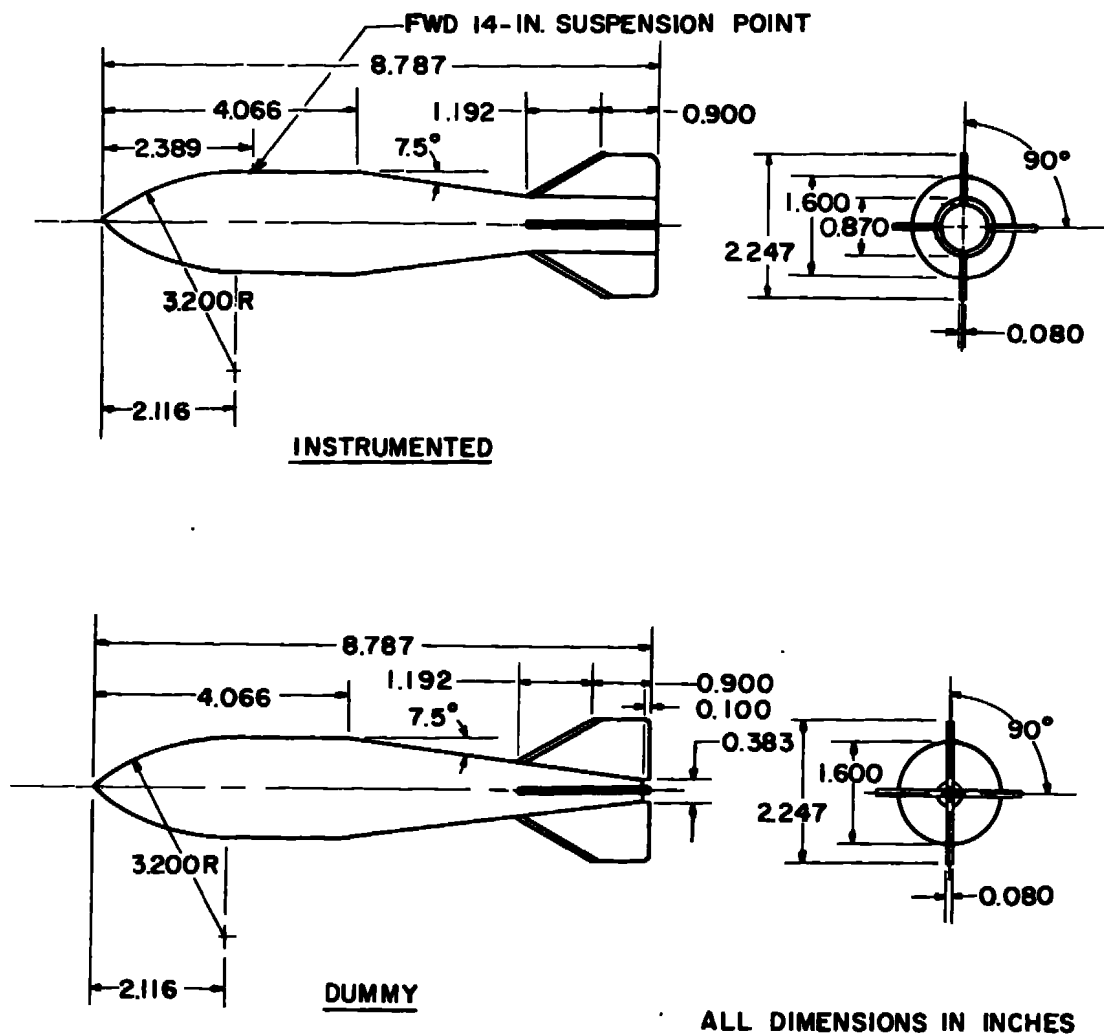
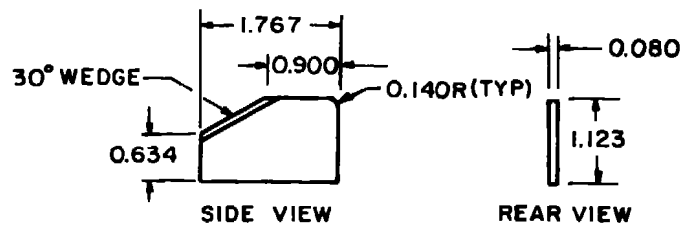


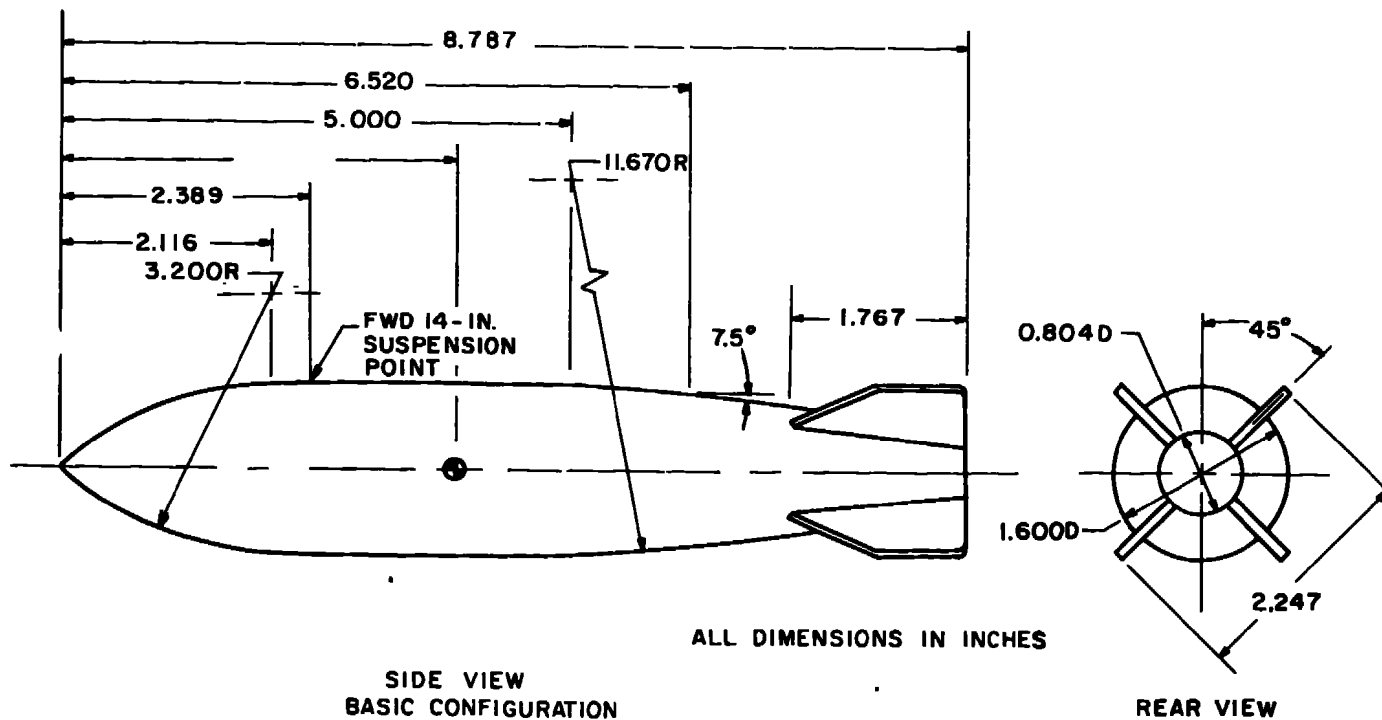
Figure 2. Schematic of the tunnel test section showing model location.



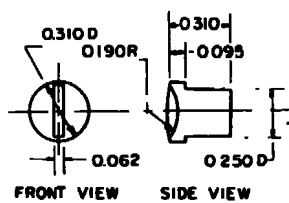
a. Standard M-117 bomb configuration
 Figure 3. Details and dimensions of the force and moment models.



FIN DETAILS

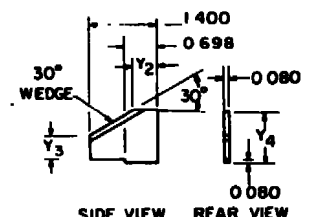


b. Modified M-117 bomb configuration
Figure 3. Continued.

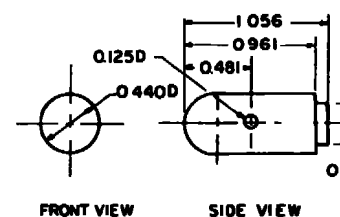


NOSE PLUG DETAILS

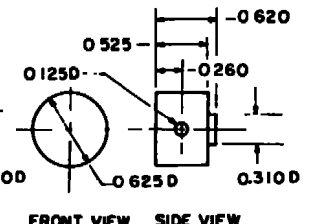
FIN	Y_2	Y_3	Y_4
16-IN.	0.507	0.585	1.100
14-IN.	0.557	0.539	1.025
12-IN.	0.606	0.492	0.950



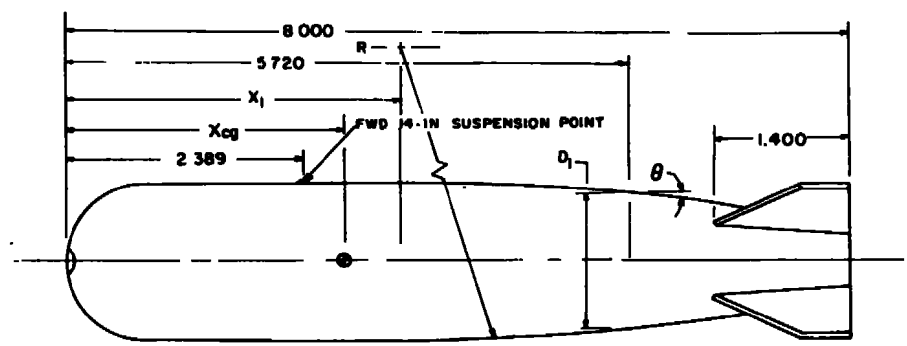
FIN DETAILS



FMU-56 FUZE DETAILS



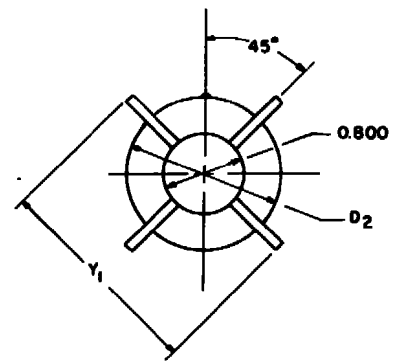
FMU-110 FUZE DETAILS



ALL DIMENSIONS IN INCHES

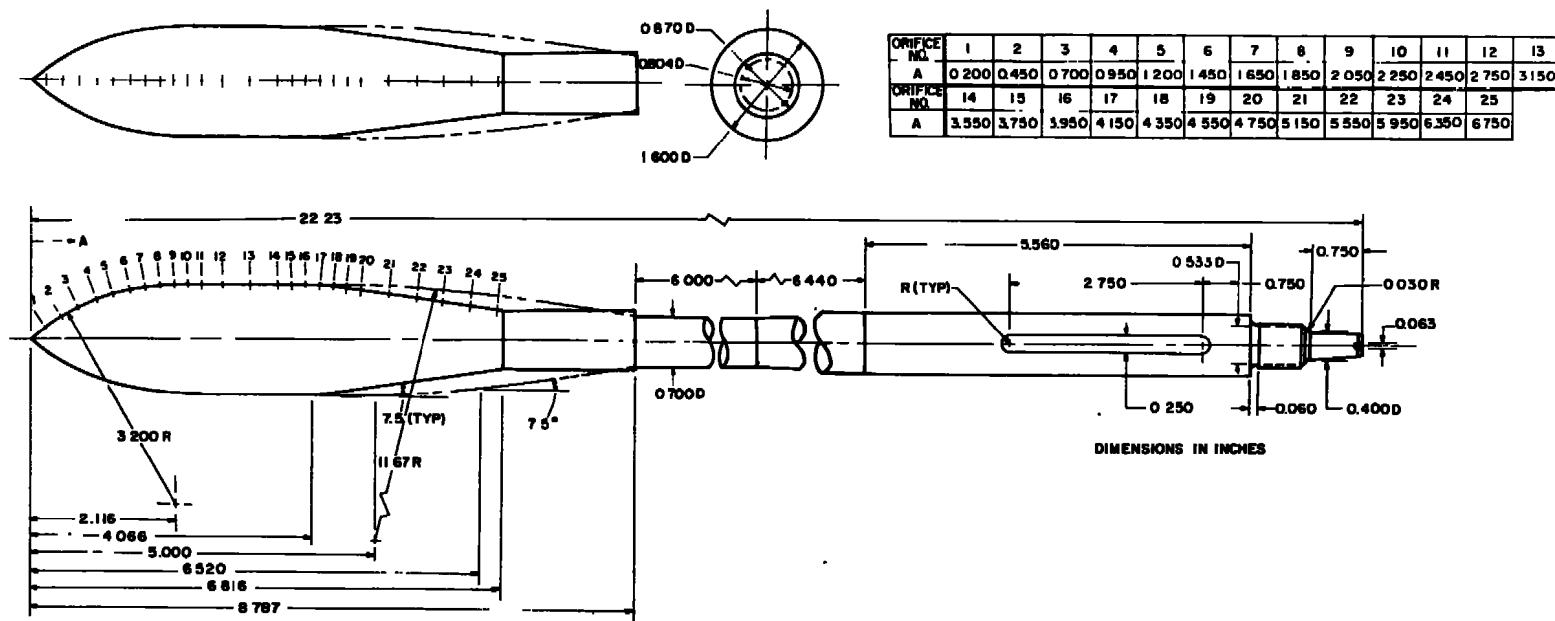
MODEL	X_1	X_{cg}	Y_1	D_1	D_2	θ	R
16-IN.	4.197	VAR.	2.200	1.400	1.600	7.50°	11.67
14-IN.	4.184	VAR.	2.050	1.250	1.400	5.63°	15.77
12-IN.	4.176	VAR.	1.900	1.099	1.200	3.75°	23.62

SIDE VIEW
BASIC CONFIGURATION



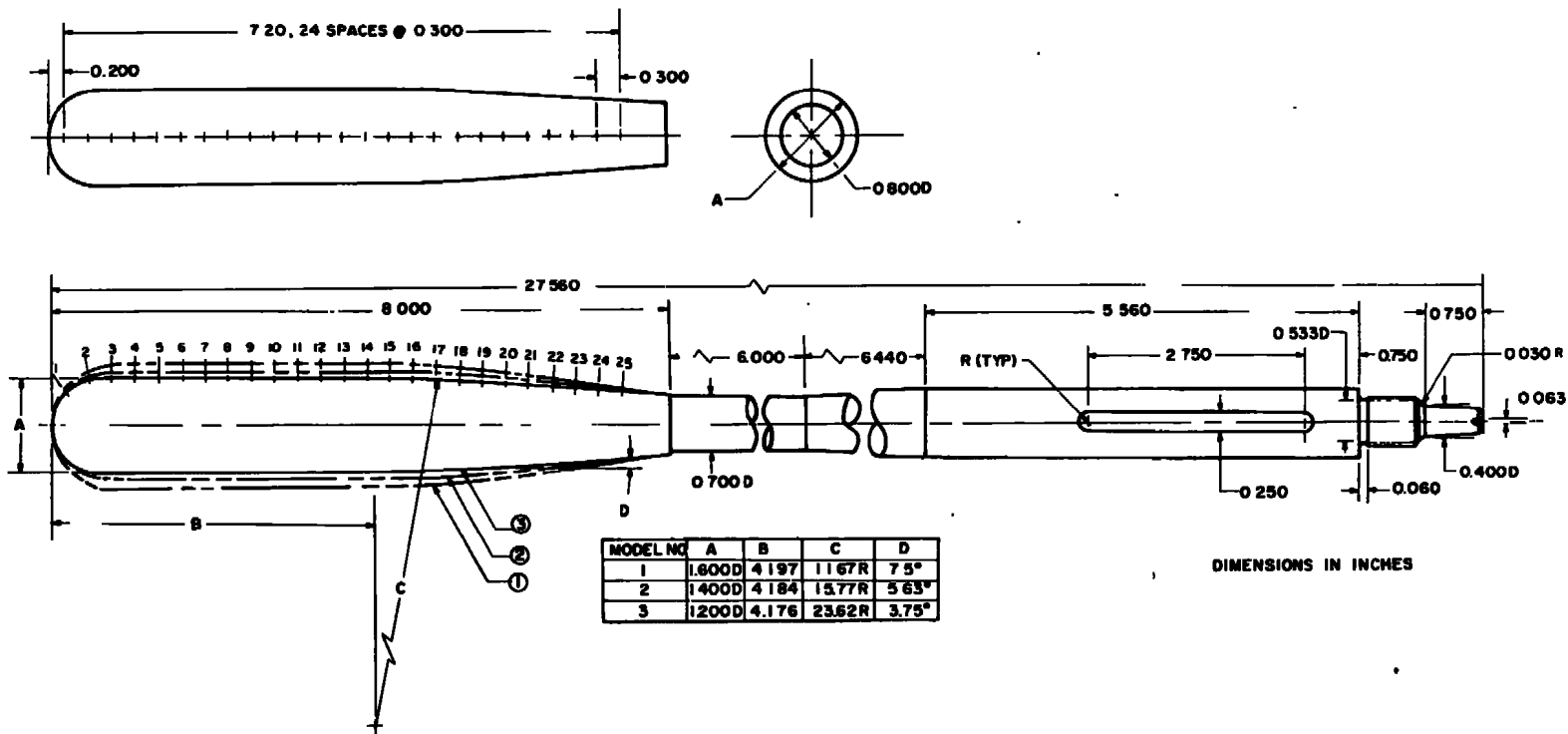
REAR VIEW

c. Maximum volume bomb
Figure 3. Concluded.

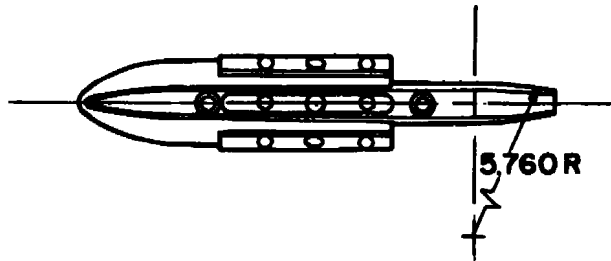
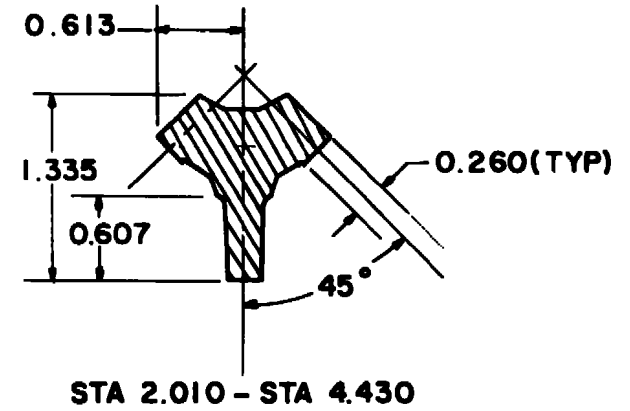
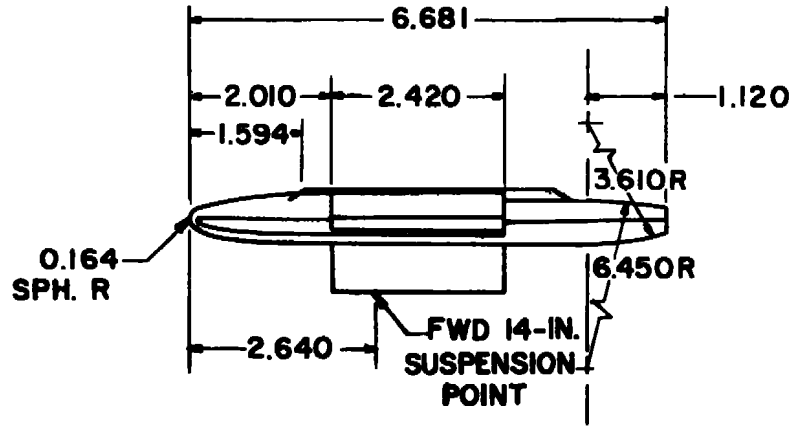


a. M-117 bomb

Figure 4. Details and dimensions of the pressure distribution models.

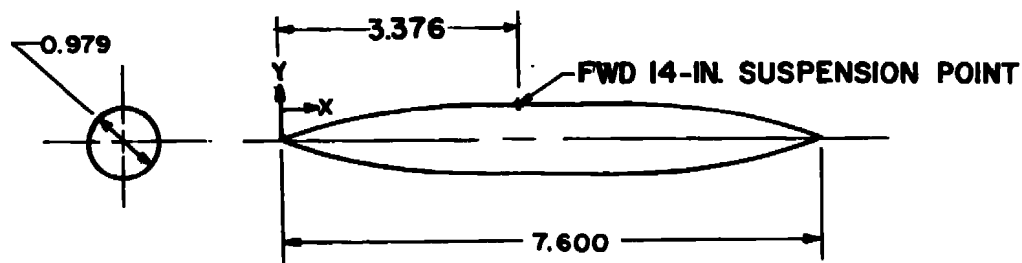


b. Maximum volume bomb
Figure 4. Concluded.



ALL DIMENSIONS IN INCHES

Figure 5. Details and dimensions of the geometrically scaled triple ejection rack model.



ALL DIMENSIONS IN INCHES

COORDINATES

X	Y	X	Y
0.0000	0.0000	4.8800	0.4882
0.0800	0.0292	4.9600	0.4870
0.1600	0.0576	5.0400	0.4850
0.2400	0.0850	5.1200	0.4822
0.3200	0.1115	5.2000	0.4786
0.4000	0.1372	5.2800	0.4742
0.4800	0.1619	5.3600	0.4691
0.5600	0.1857	5.4400	0.4631
0.6400	0.2087	5.5200	0.4563
0.7200	0.2307	5.6000	0.4487
0.8000	0.2518	5.6800	0.4403
0.8800	0.2721	5.7600	0.4312
0.9600	0.2914	5.8400	0.4212
1.0400	0.3098	5.9200	0.4104
1.1200	0.3080	6.0000	0.3992
1.2000	0.3232	6.0800	0.3865
1.2800	0.3598	6.1600	0.3733
1.3600	0.3746	6.2400	0.3594
1.4400	0.3885	6.3200	0.3446
1.5200	0.4016	6.4000	0.3291
1.6000	0.4137	6.4800	0.3127
1.6800	0.4250	6.5600	0.2956
1.7600	0.4353	6.6400	0.2776
1.8400	0.4448	6.7200	0.2589
1.9200	0.4533	6.8000	0.2393
2.0000	0.4609	6.8800	0.2190
2.0800	0.4677	6.9600	0.1978
2.1600	0.4735	7.0400	0.1759
2.2400	0.4785	7.1200	0.1532
2.3200	0.4825	7.2000	0.1296
2.4000	0.4857	7.2800	0.1053
2.4800	0.4879	7.3600	0.0802
2.5600	0.4893	7.4400	0.0542
2.6400	0.4896	7.5200	0.0223
4.8000	0.4896	7.6000	0.0000

Figure 6. Details and dimensions of the mathematically simulated triple ejection rack model.

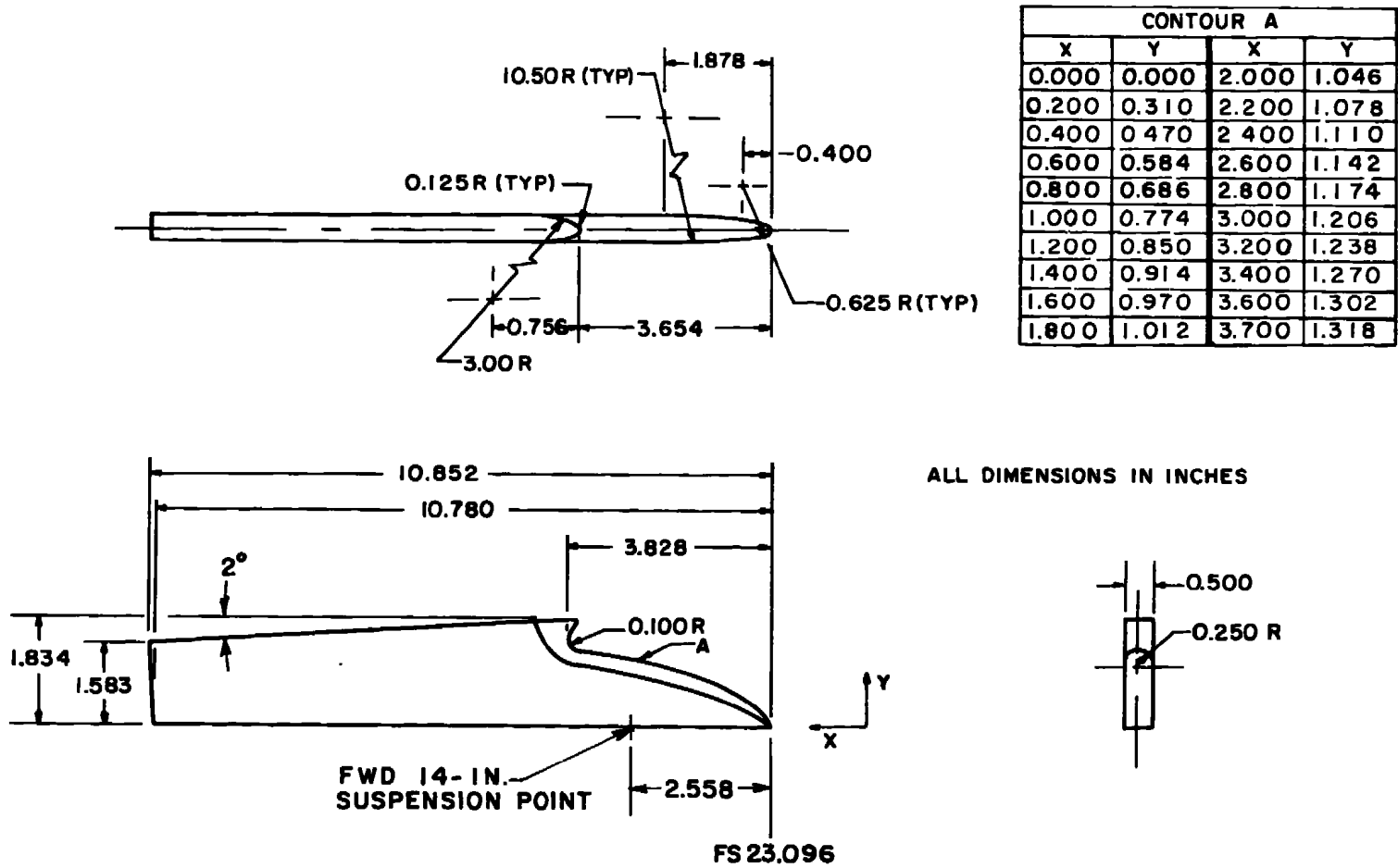


Figure 7. Details and dimensions of the F-4 inboard pylon model.

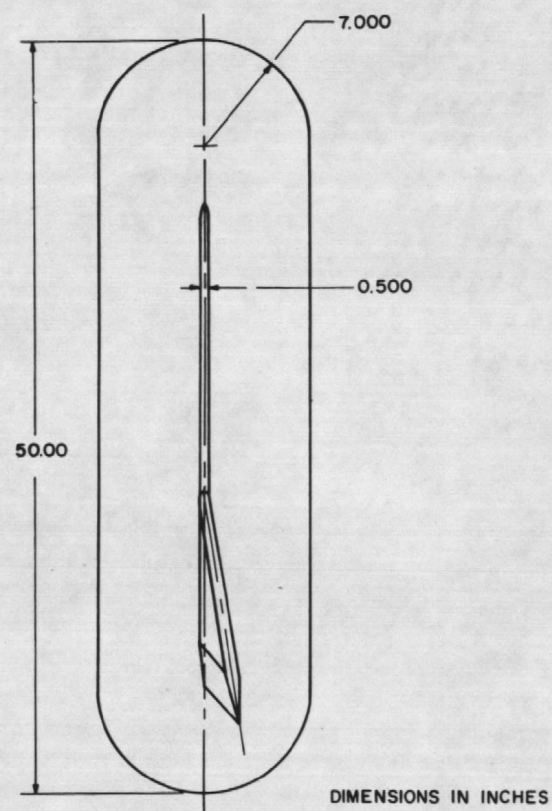
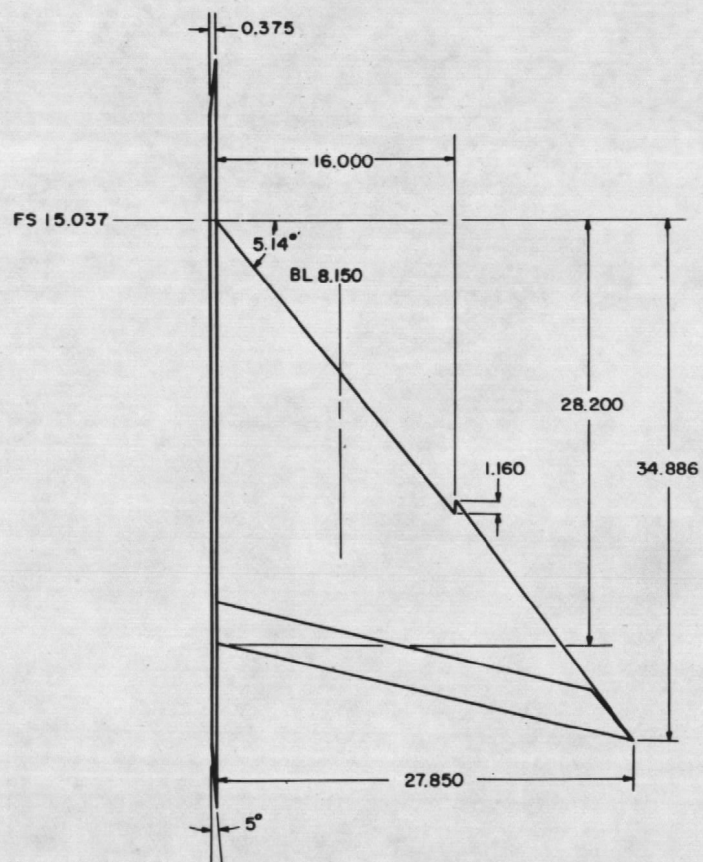


Figure 8. Details and dimensions of the flat-plate, half-wing model.

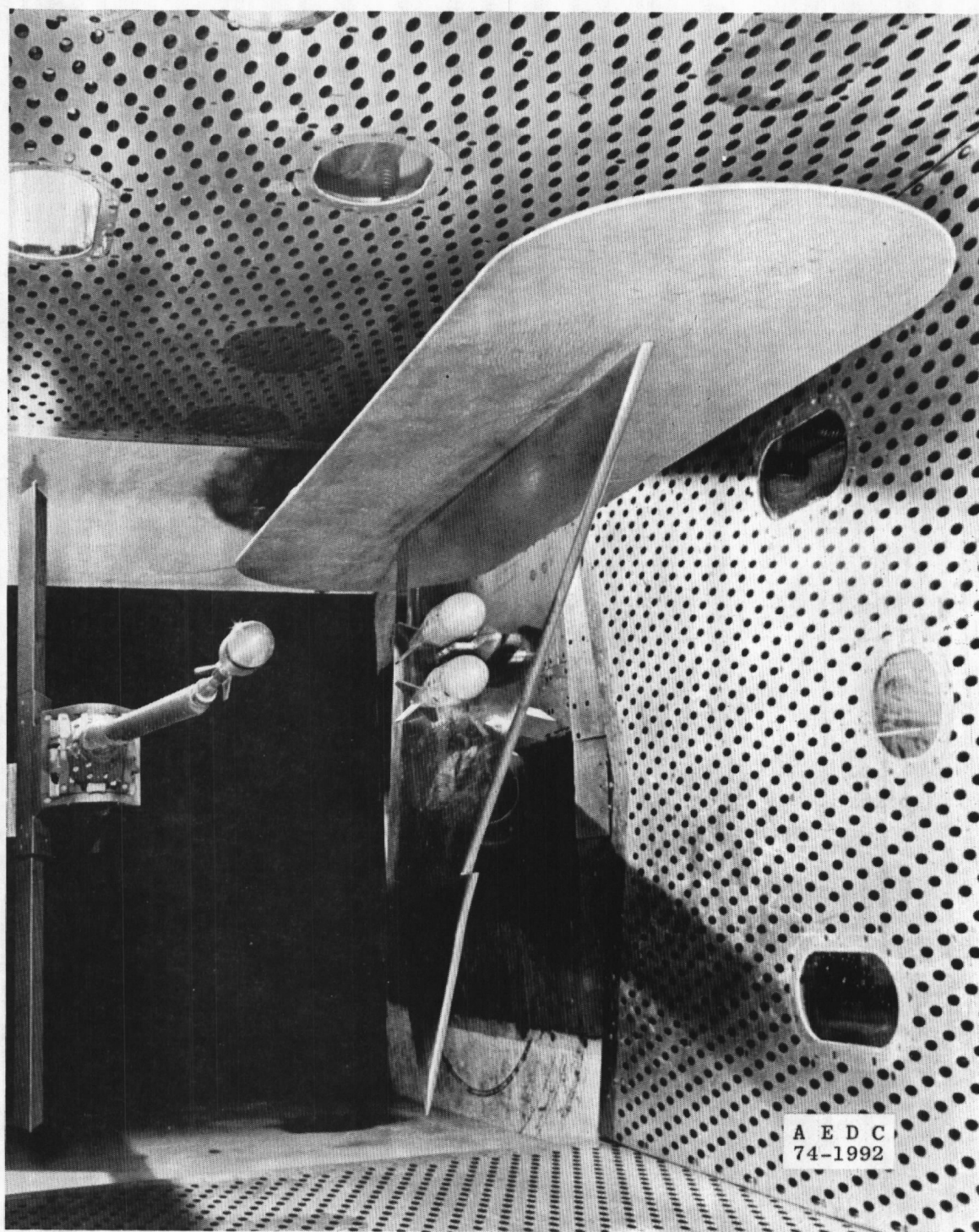
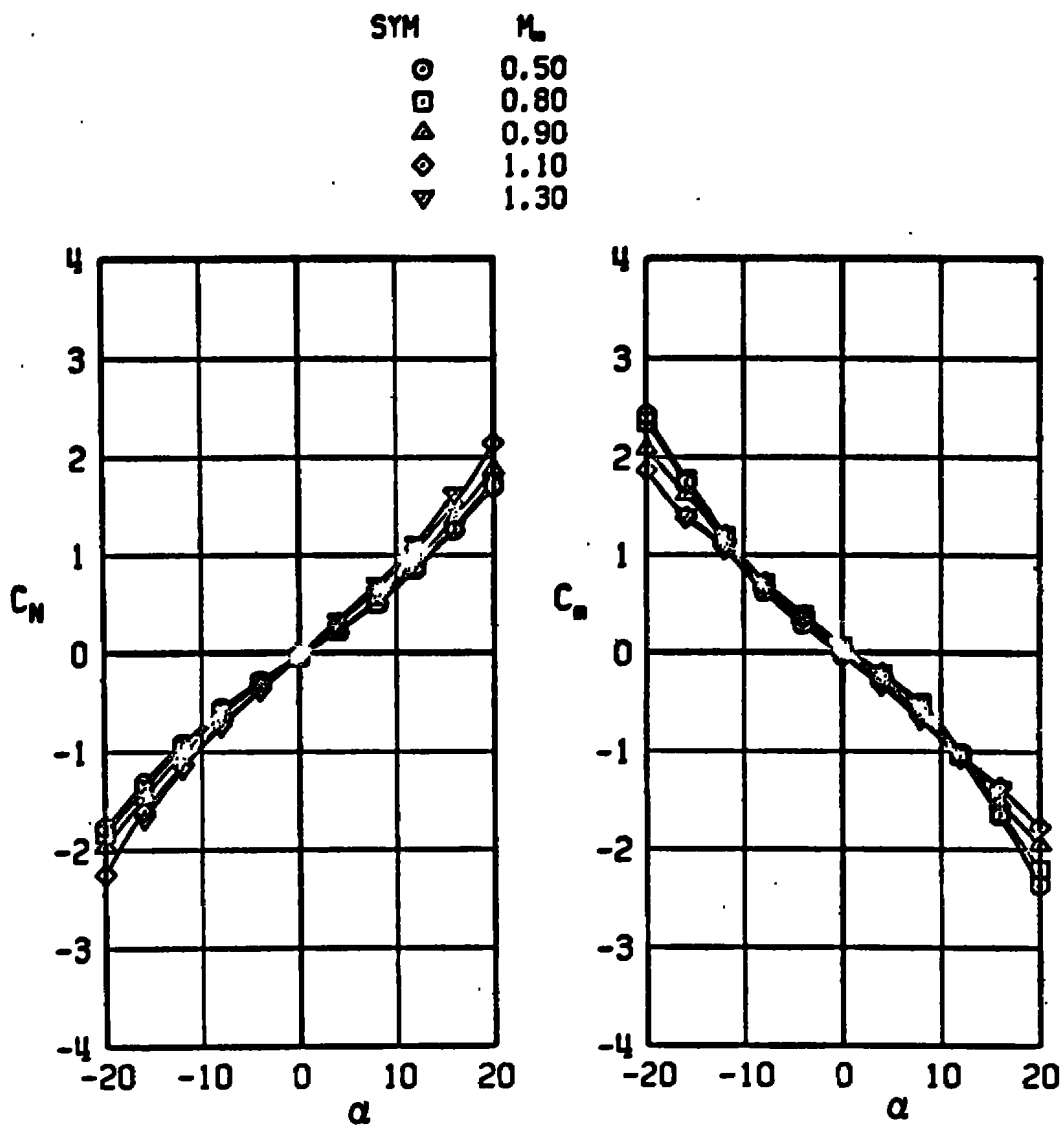


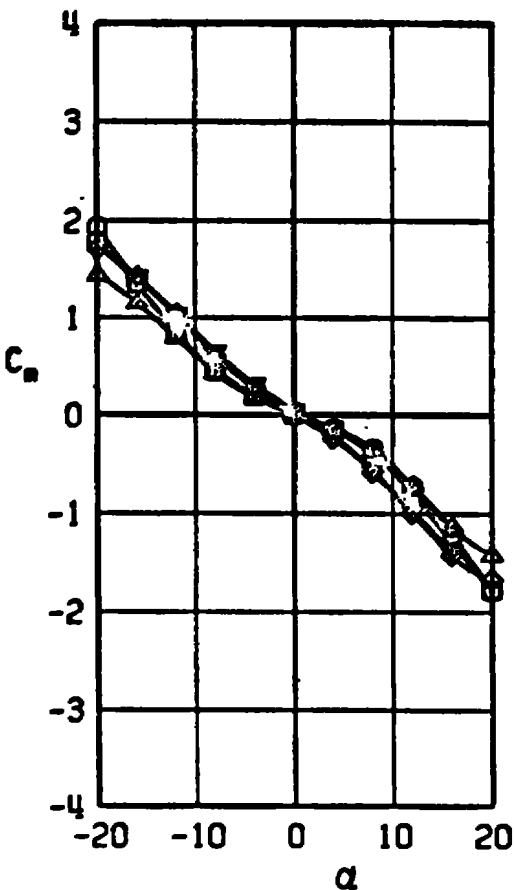
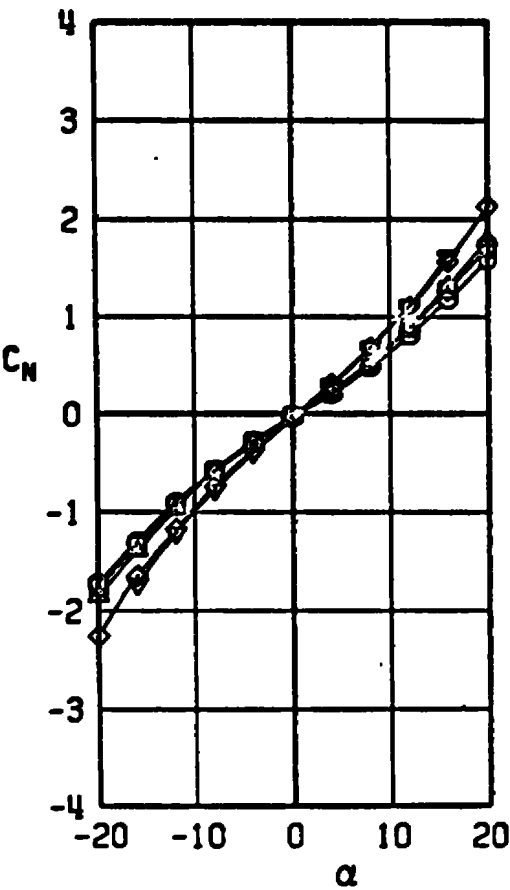
Figure 9. Photograph of a typical test configuration installed in the tunnel.



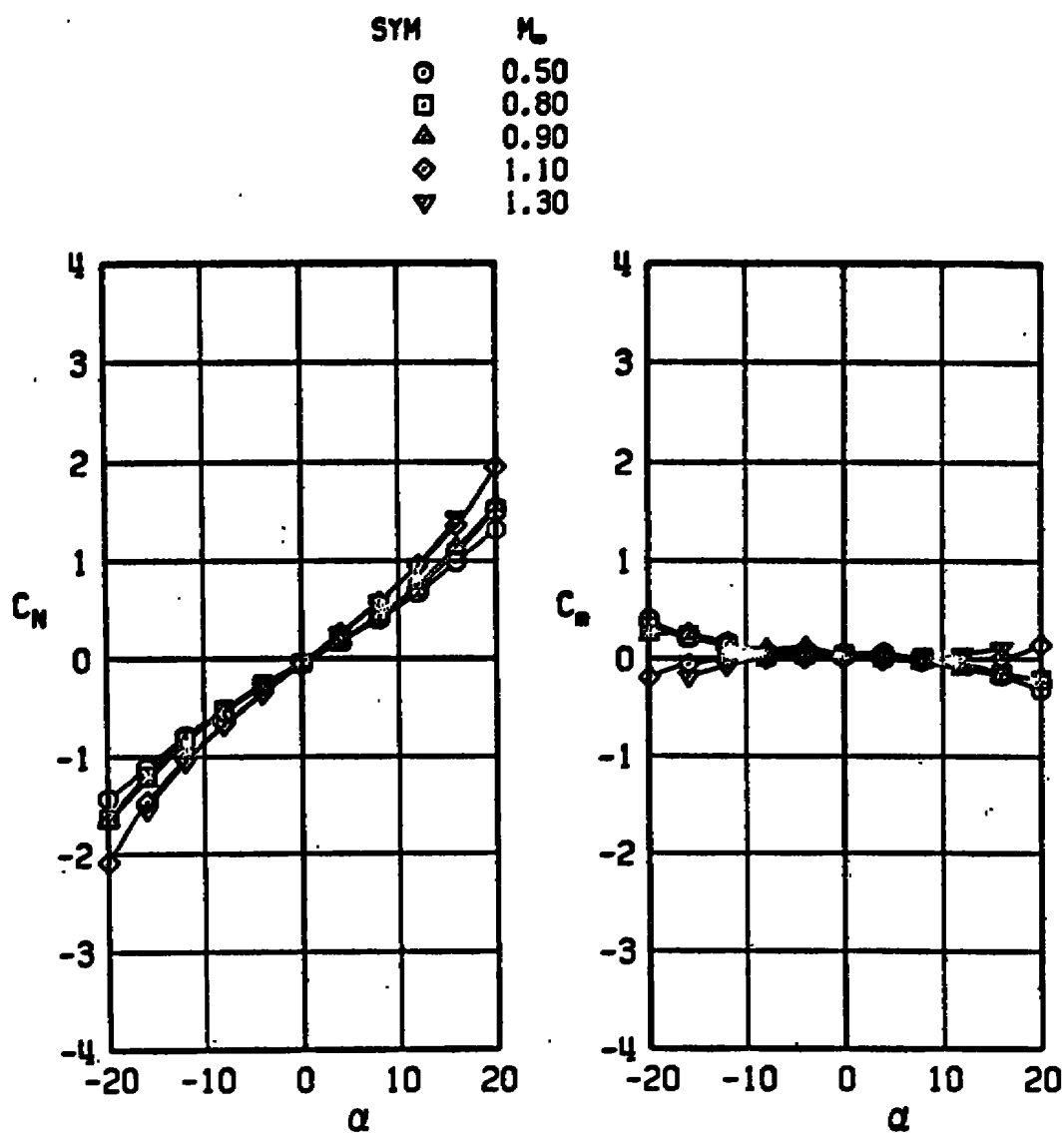
a. Standard M-117 bomb configuration

Figure 10. Free-stream force data for the M-117 bombs, $\Delta\phi = 0$.

SYM	M_∞
○	0.50
□	0.80
△	0.90
◇	1.10
▽	1.30

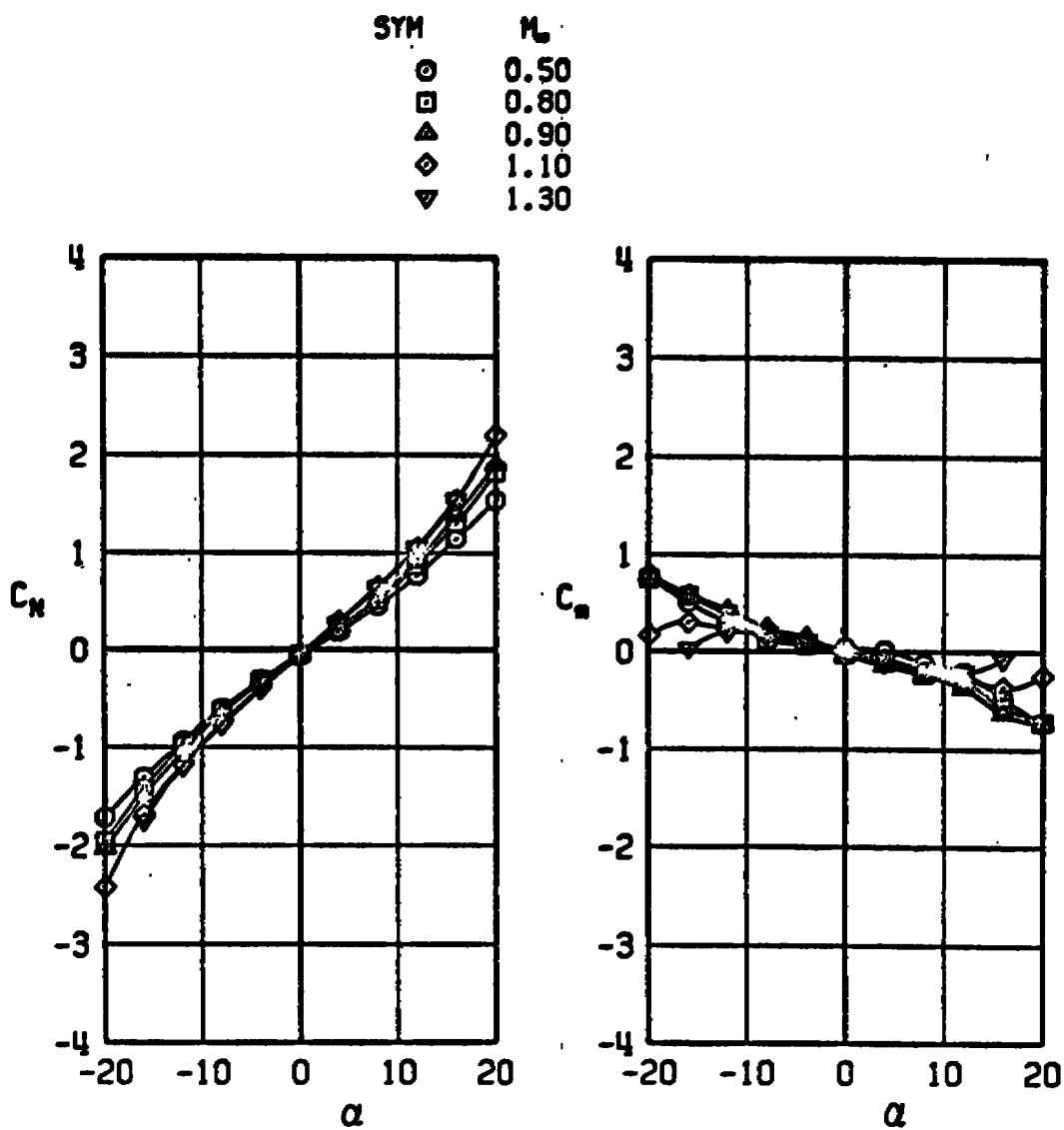


b. Modified M-117 bomb configuration
Figure 10. Concluded.

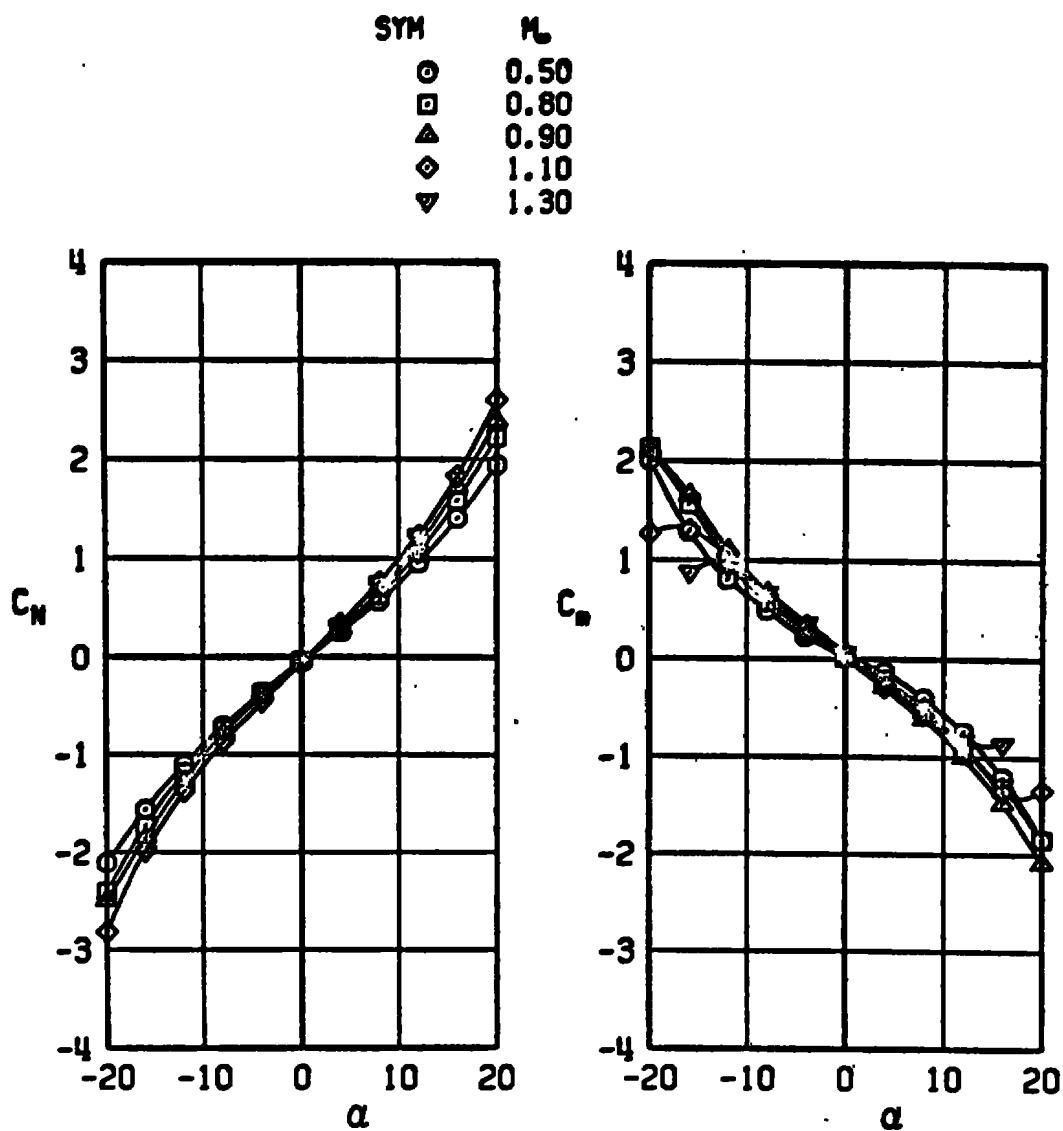


a. 16-in.-diam maximum volume bomb

Figure 11. Free-stream force data for the maximum volume bombs, $\Delta\phi = 0$.

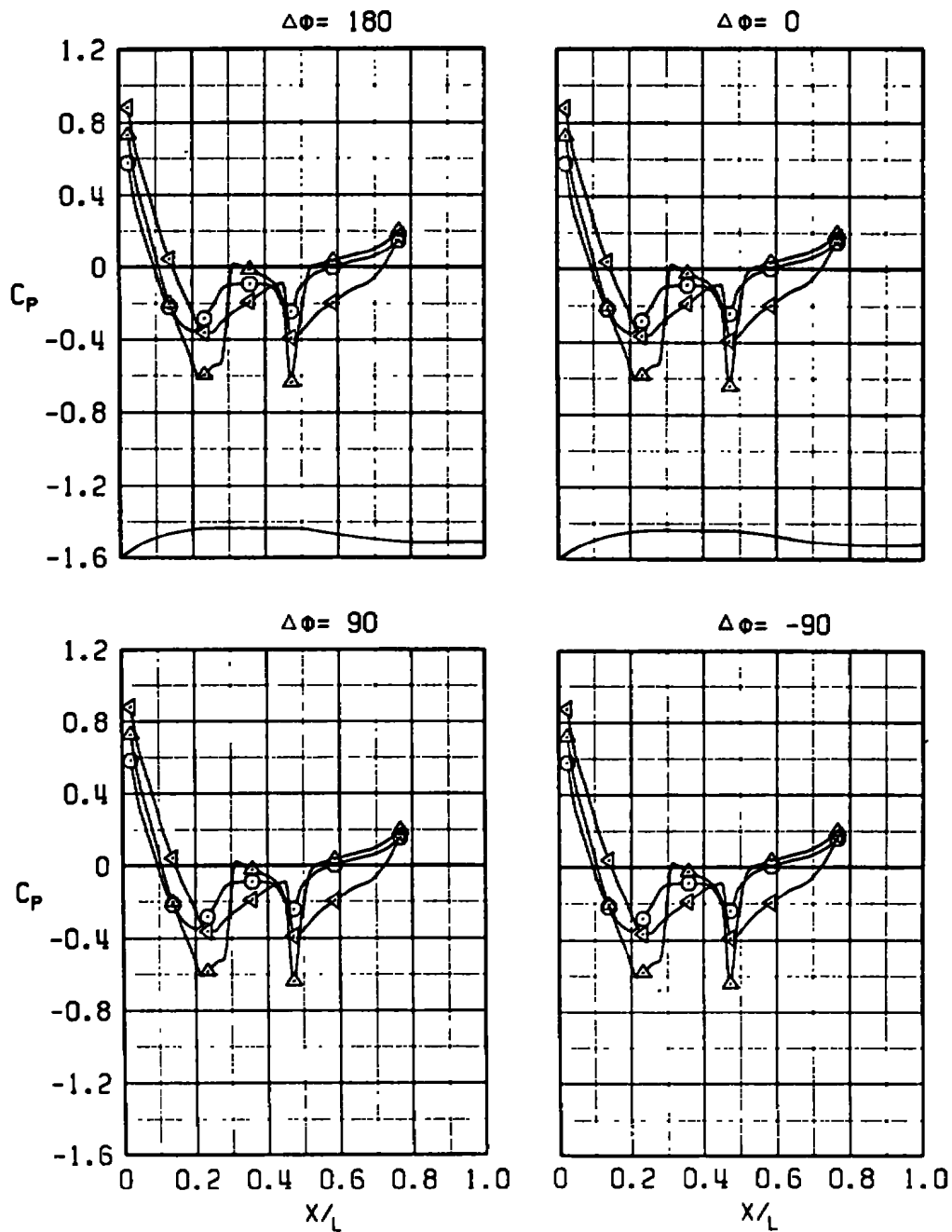


b. 14-in.-diam maximum volume bomb
Figure 11. Continued.



c. 12-in.-diam maximum volume bomb
Figure 11. Concluded.

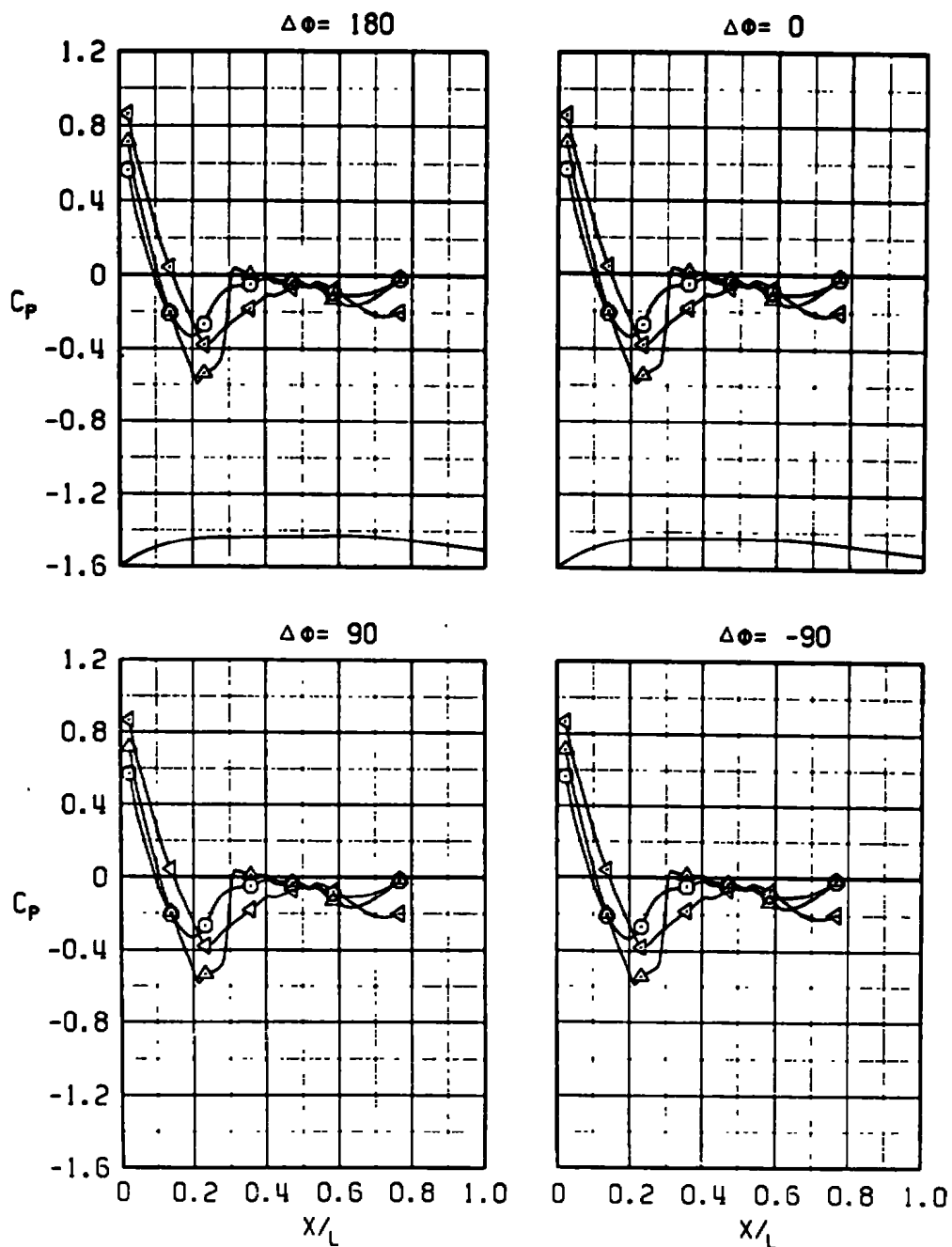
SYM	M_∞	α	$R \times 10^{-6}$	FUSE
○	0.5	0	3.08	NONE
△	0.9	0	3.13	NONE
◁	1.1	0	3.08	NONE



a. Standard M-117 bomb configuration

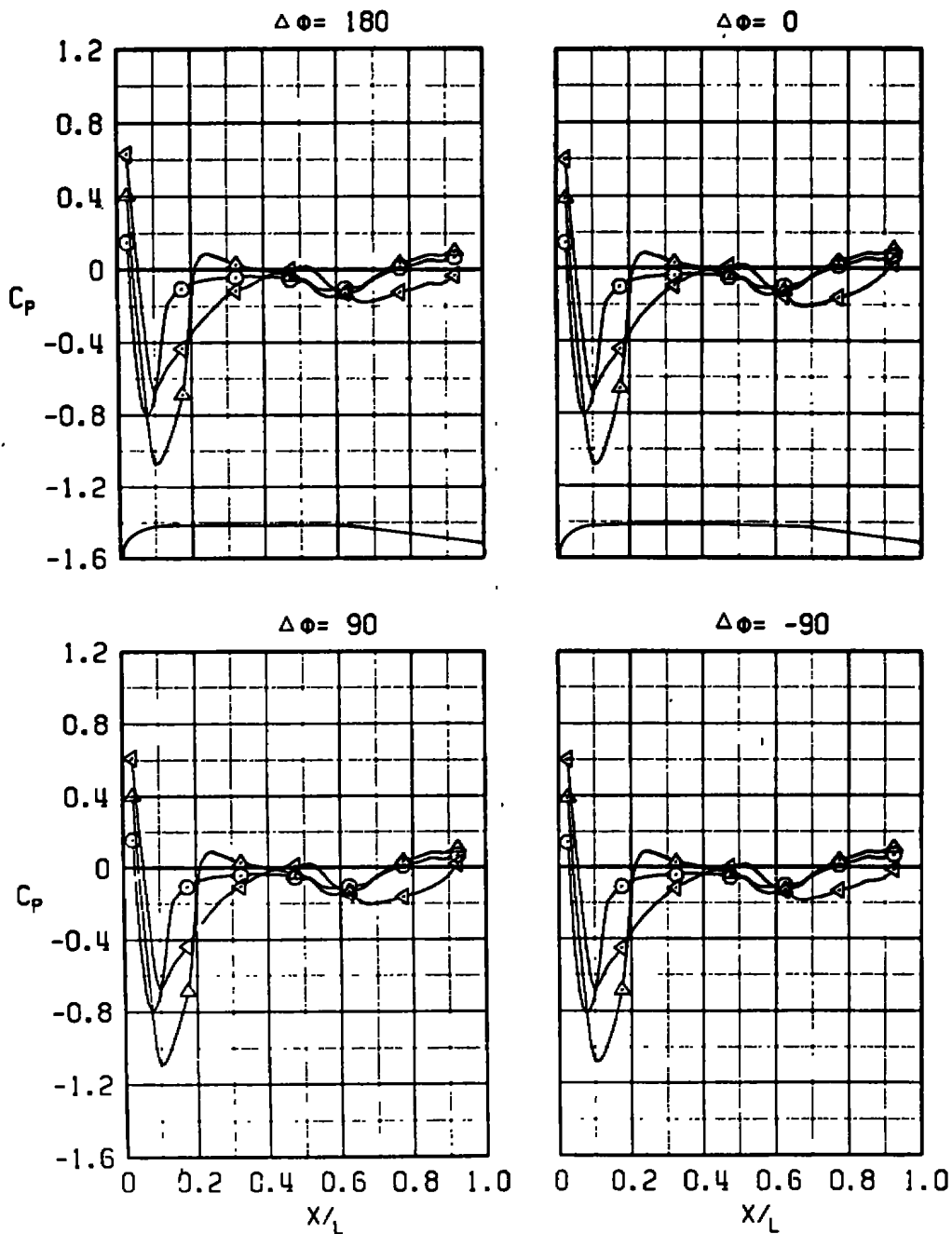
Figure 12. Free-stream pressure distribution data for the M-117 bombs.

SYM	M_∞	α	$R \times 10^{-6}$	FUSE
○	0.5	0	3.19	NONE
△	0.9	0	3.07	NONE
◄	1.1	0	3.06	NONE



b. Modified M-117 bomb configuration
Figure 12. Concluded.

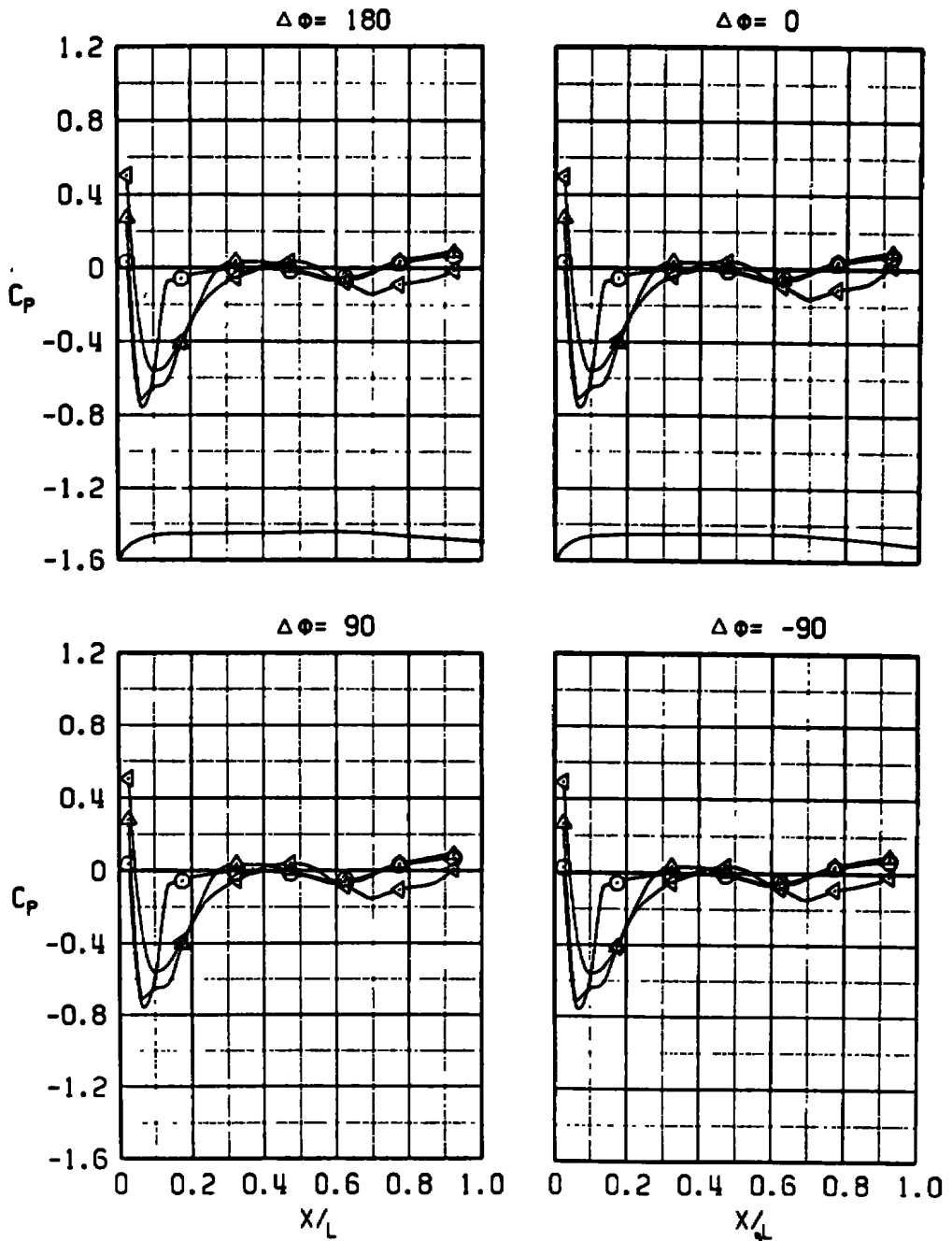
SYM	M_∞	α	$R \times 10^{-5}$	FUSE
○	0.5	0	3.01	NONE
△	0.9	0	3.02	NONE
◁	1.1	0	3.00	NONE



a. 16-in.-diam maximum volume bomb

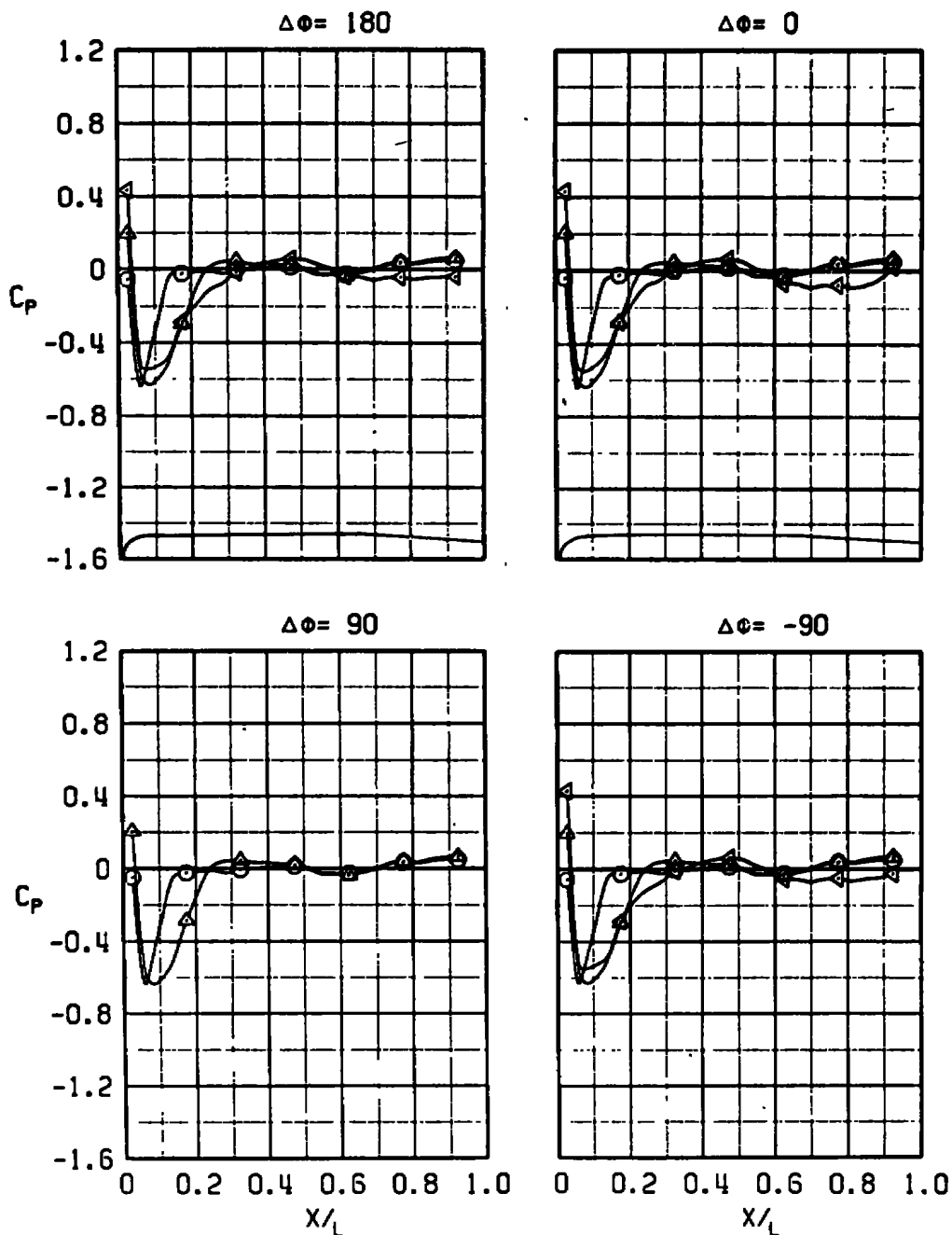
Figure 13. Free-stream pressure distribution data for the maximum volume bombs.

SYM	M_∞	α	$R \times 10^{-6}$	FUSE
○	0.5	0	1.36	NONE
△	0.9	0	1.99	NONE
◁	1.1	0	2.20	NONE



b. 14-in.-diam maximum volume bomb
Figure 13. Continued.

SYM	M_∞	α	$R \times 10^{-6}$	FUSE
○	0.5	0	1.58	NONE
△	0.9	0	1.97	NONE
◄	1.1	0	2.26	NONE



c. 12-in.-diam maximum volume bomb
Figure 13. Concluded.

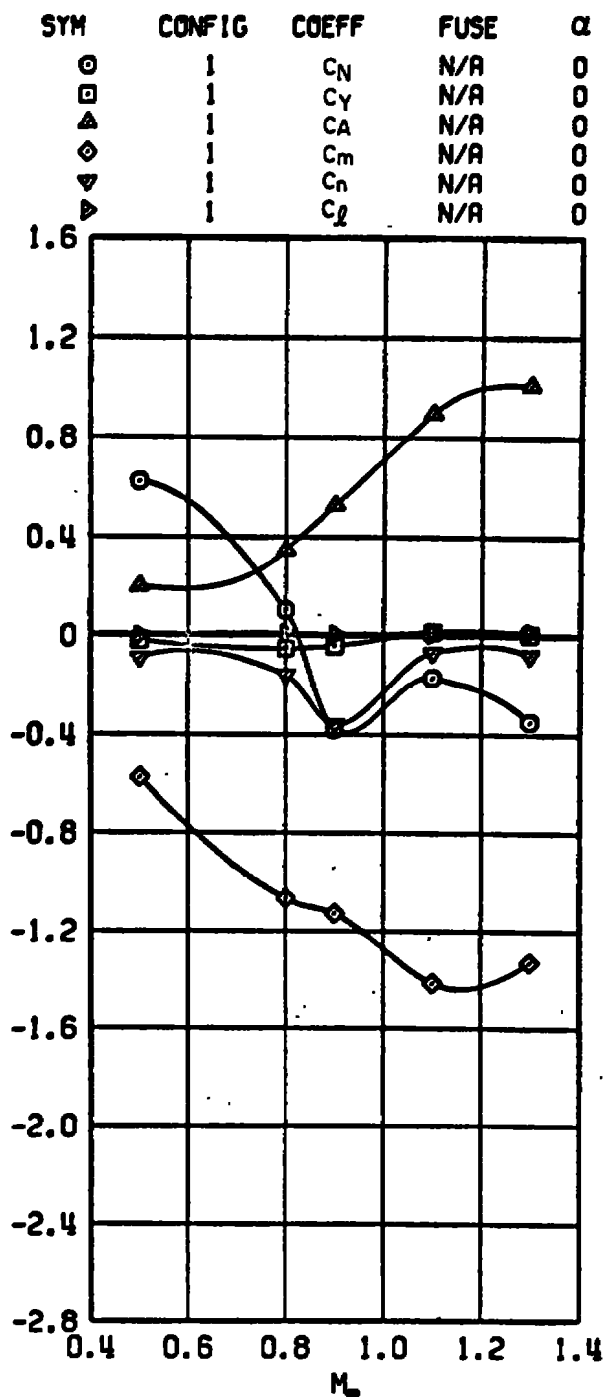


Figure 14. Carriage position airloads of the standard M-117 bomb configuration in the flow field of the isolated simulated TER, $\Delta\phi = 0$.

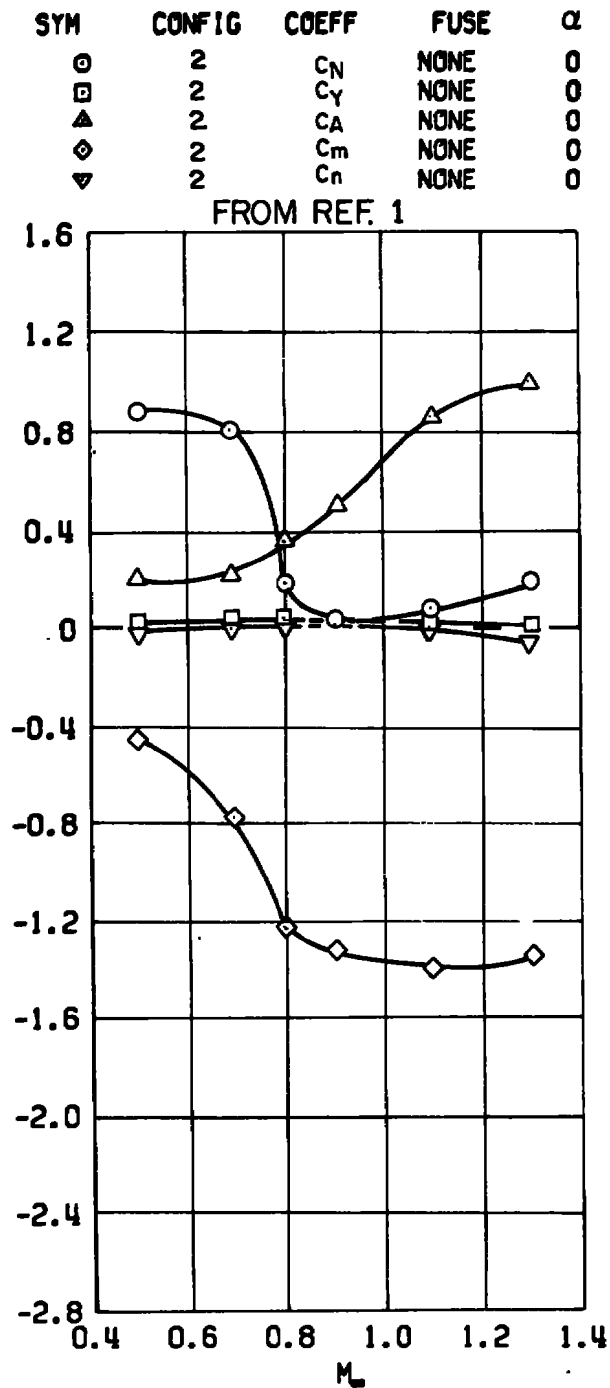


Figure 15. Carriage position airloads of the standard M-117 bomb configuration in the flow field of the isolated geometrical TER, $\Delta\phi = 0$.

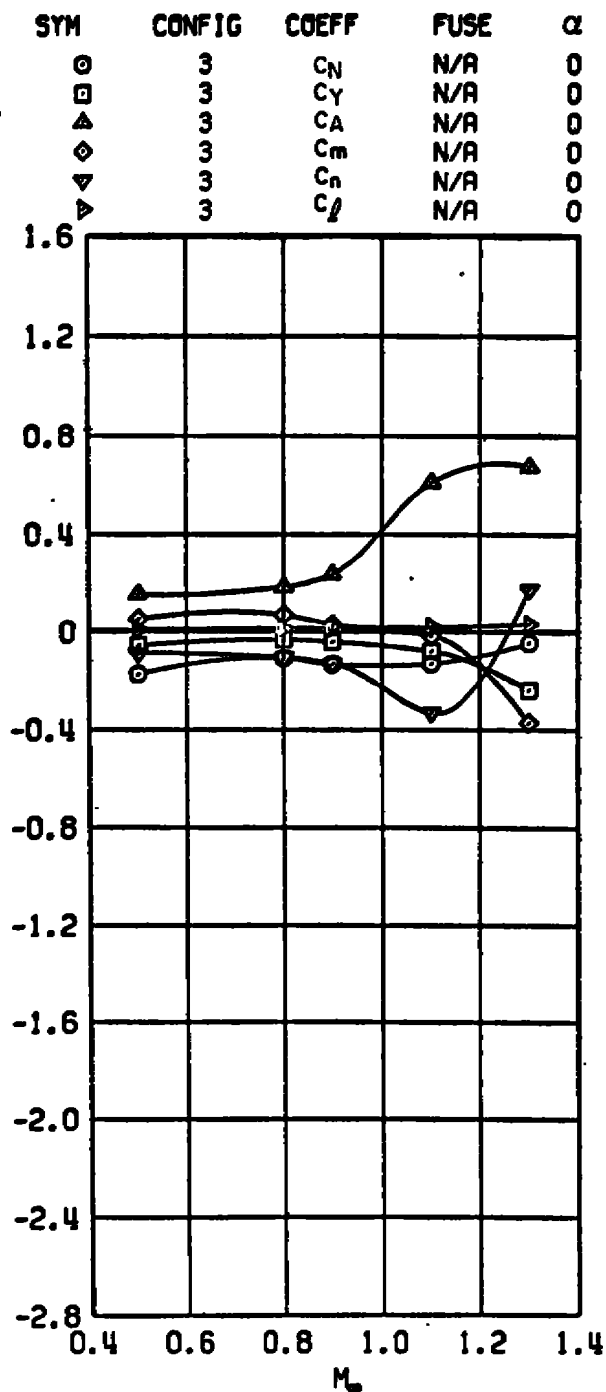
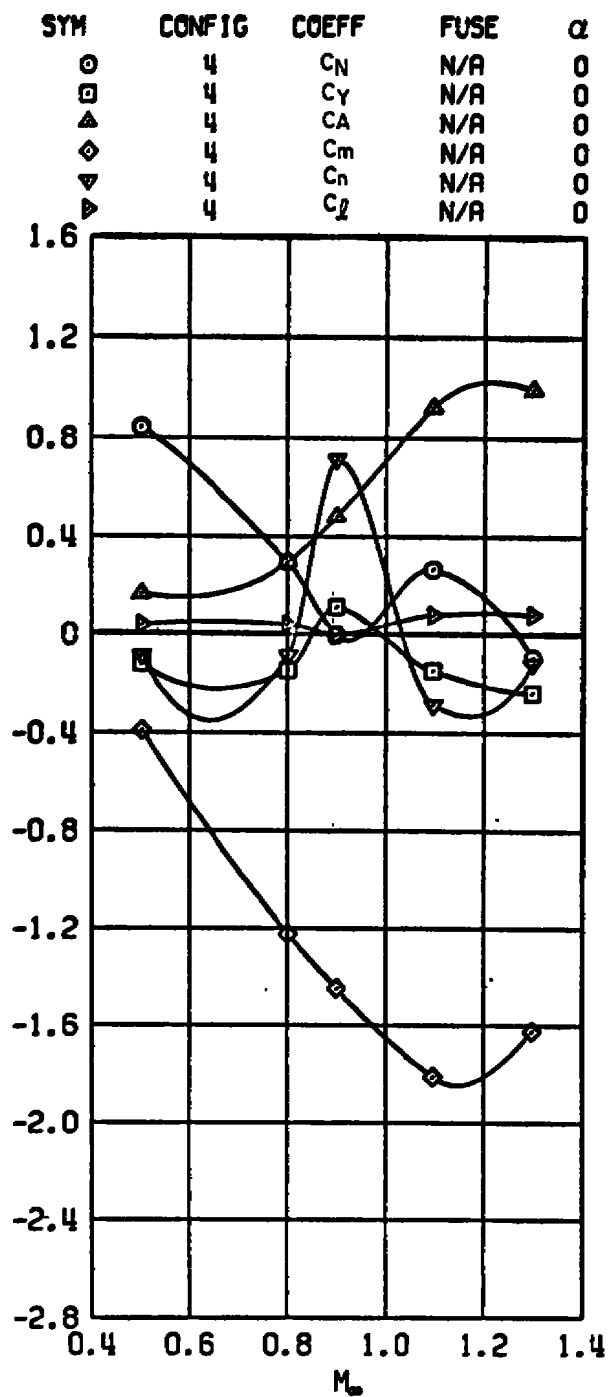
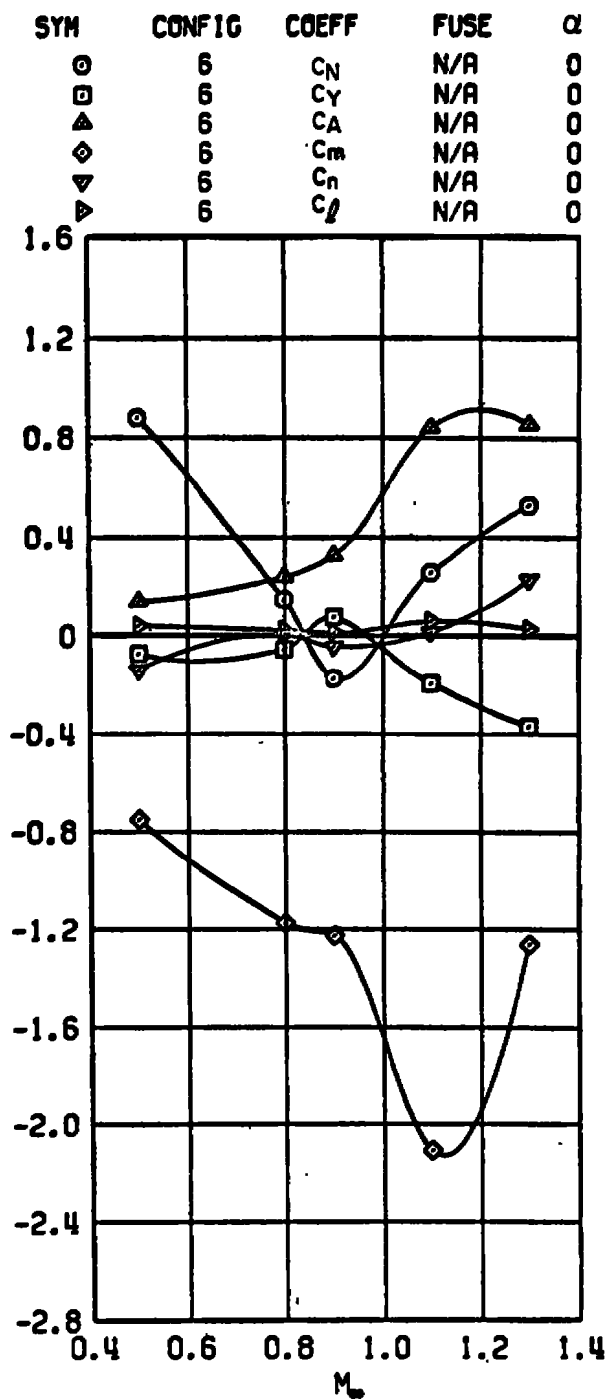


Figure 16. Carriage position airloads of the standard M-117 bomb configuration in the flow field of the wing-pylon (without TER) configuration, $\Delta\phi = 0$.

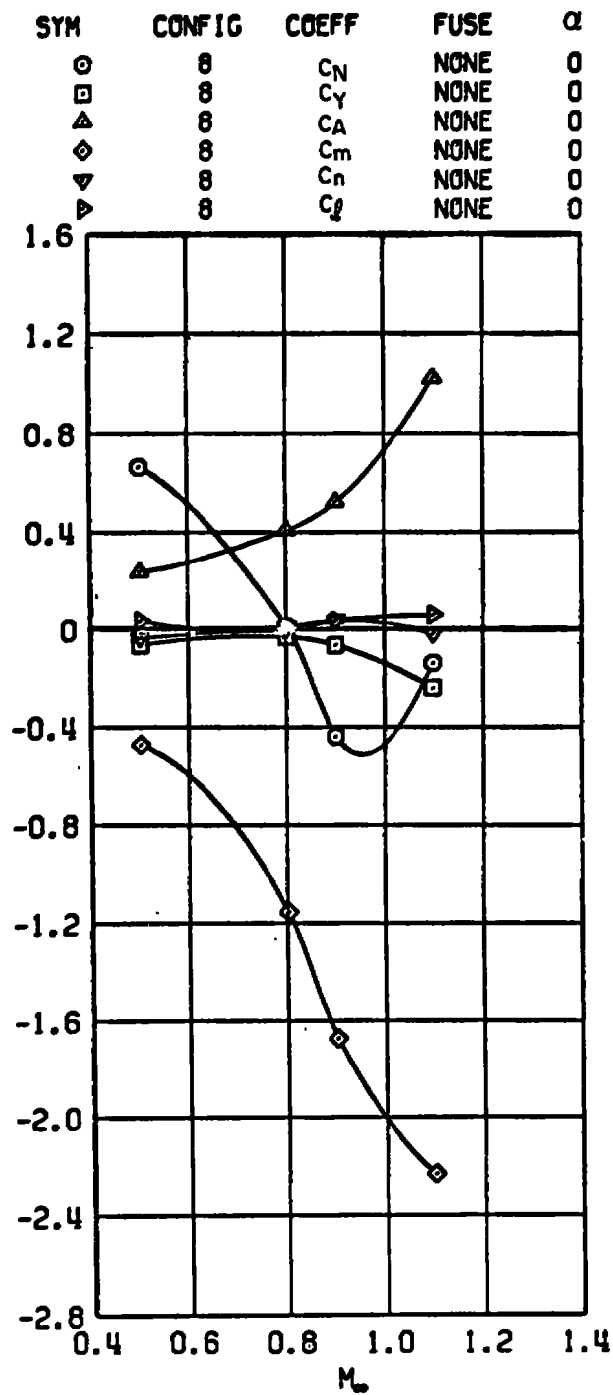


a. Standard M-117 bomb configuration

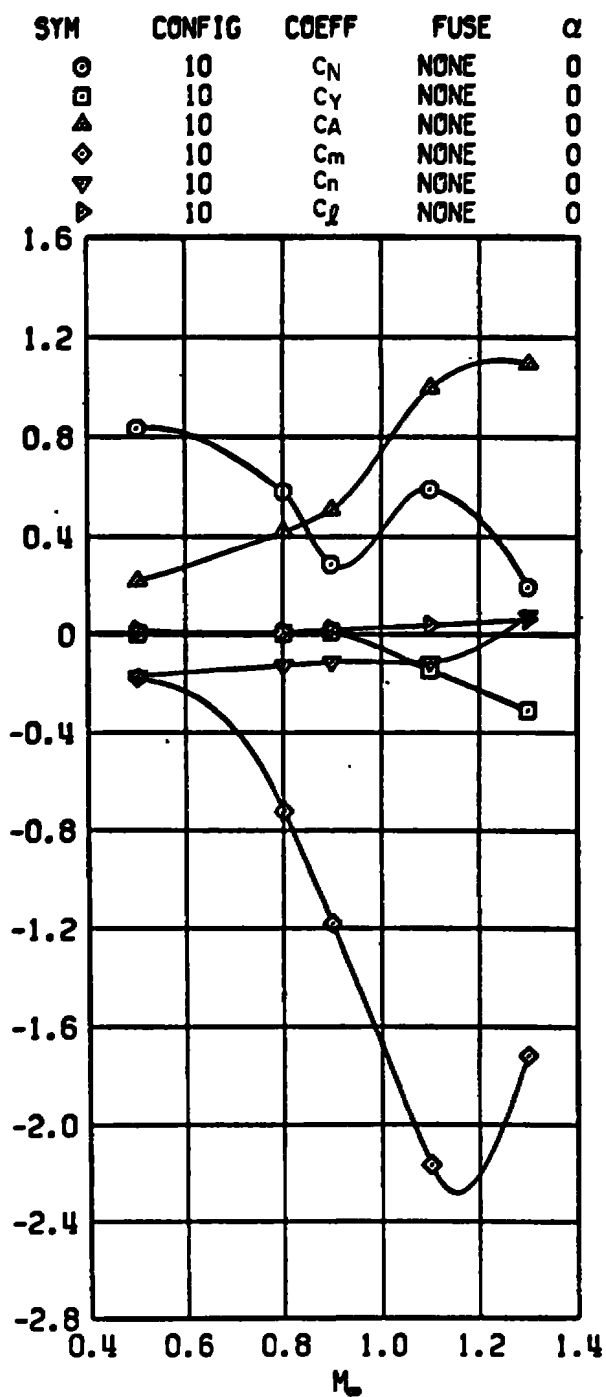
Figure 17. Carriage position airloads of the M-117 bombs in the flow field of the wing-pylon-TER configuration, $\Delta\phi = 0$.



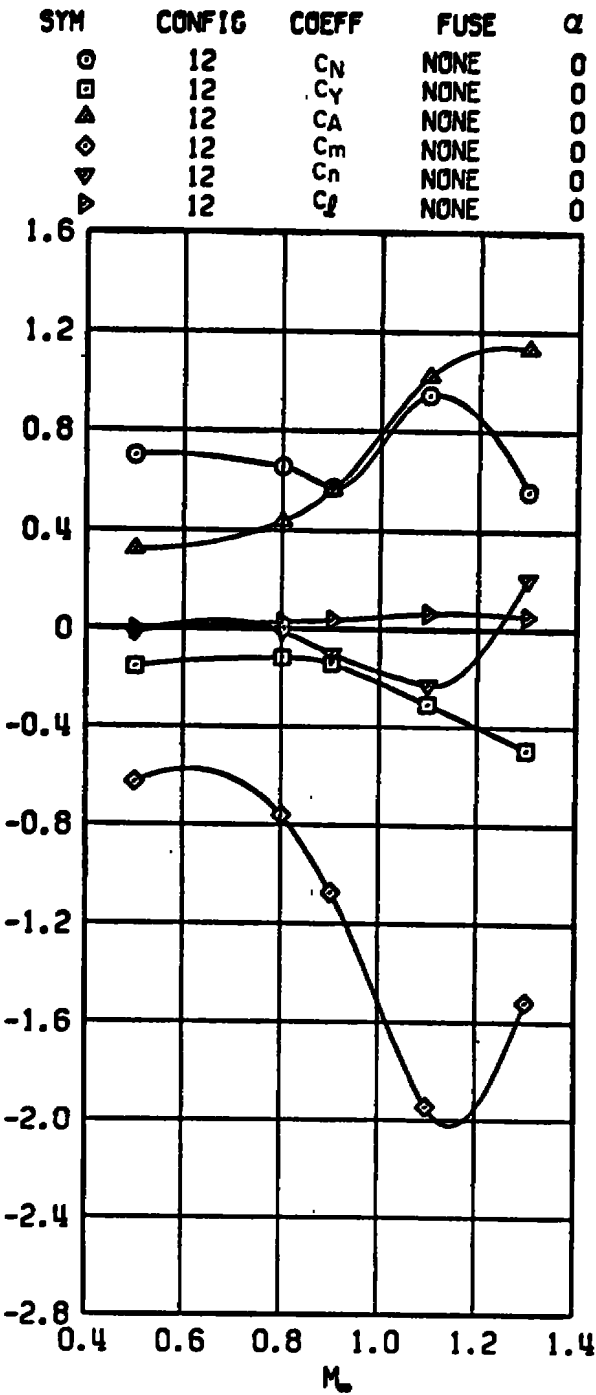
b. Modified M-117 bomb configuration
Figure 17. Concluded.



a. 16-in.-diam maximum volume bomb
 Figure 18. Carriage position airloads of the maximum volume bombs
 in the flow field of the wing-pylon-TER configuration, $\Delta\phi = 0$.



b. 14-in.-diam maximum volume bomb
Figure 18. Continued.



c. 12-in.-diam maximum volume bomb
Figure 18. Concluded.

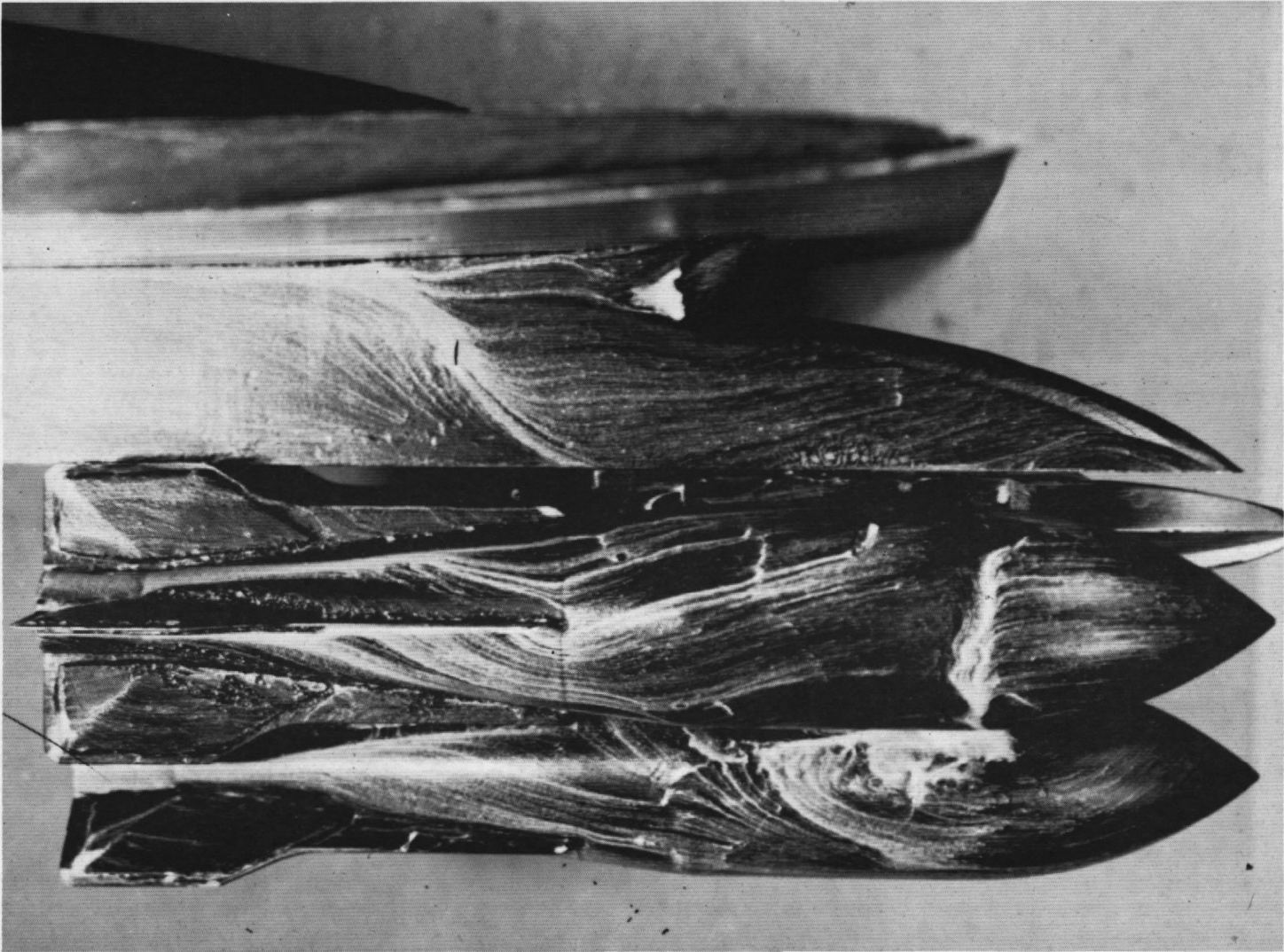
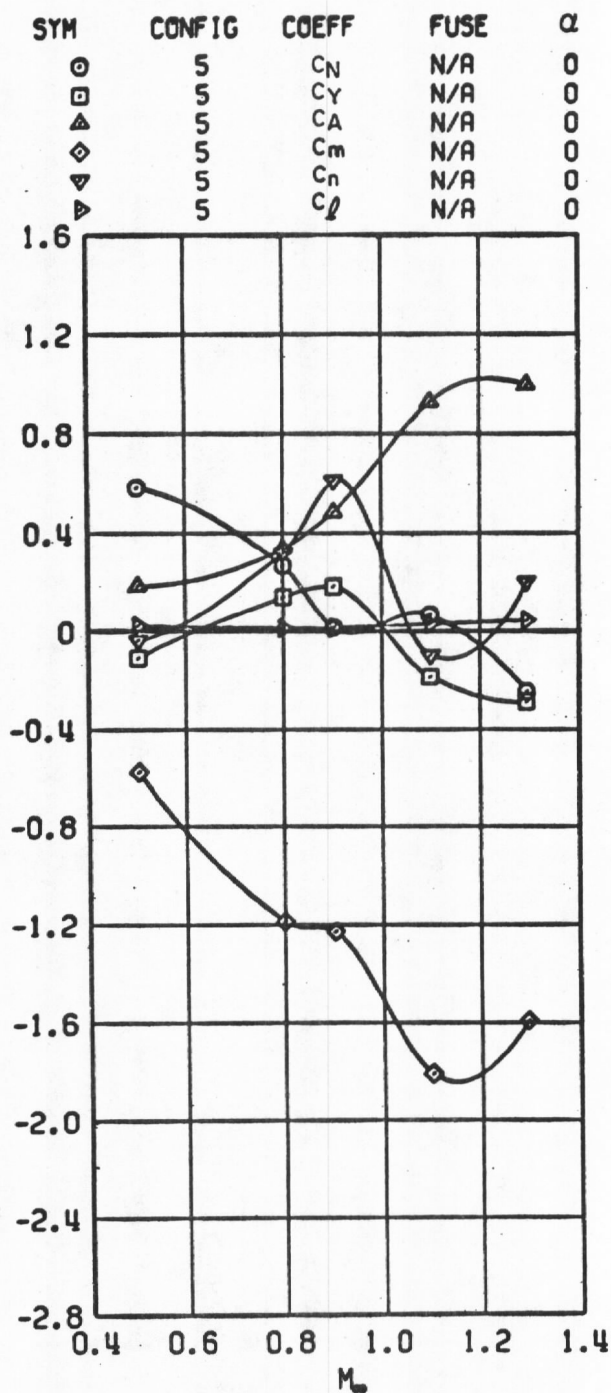
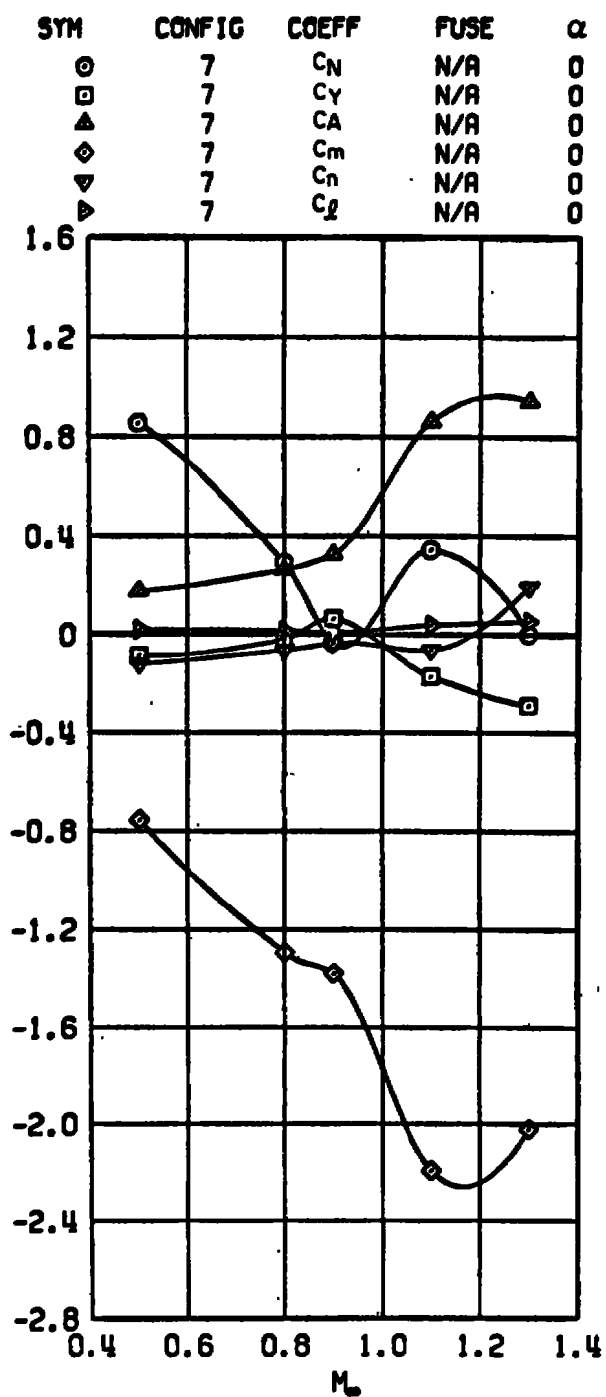


Figure 19. Oil-flow visualization photograph of a standard M-117 bomb configuration in the flow field of a wing-pylon-TER configuration, $\alpha = 0$, $M_\infty = 0.9$.



a. Standard M-117 bomb configuration

Figure 20. Carriage position airloads of the M-117 bombs in the flow field of the wing-pylon-TER configuration, $\Delta\phi = 45^\circ$.



b. Modified M-117 bomb configuration
 Figure 20. Concluded.

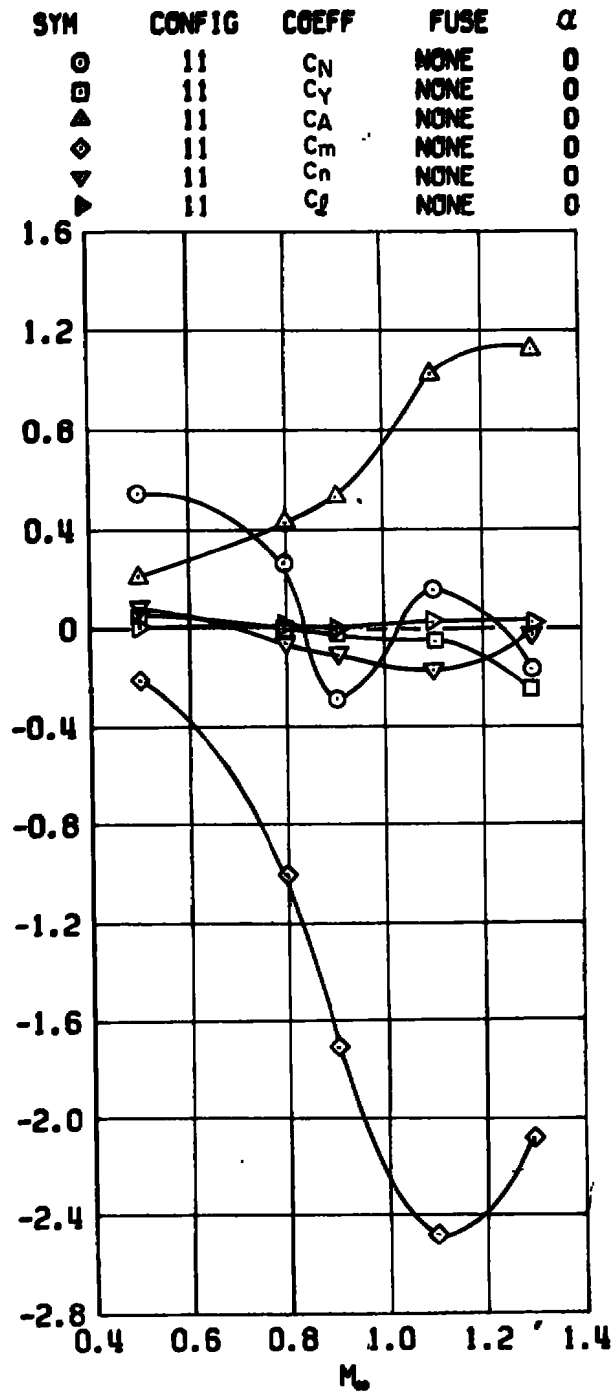
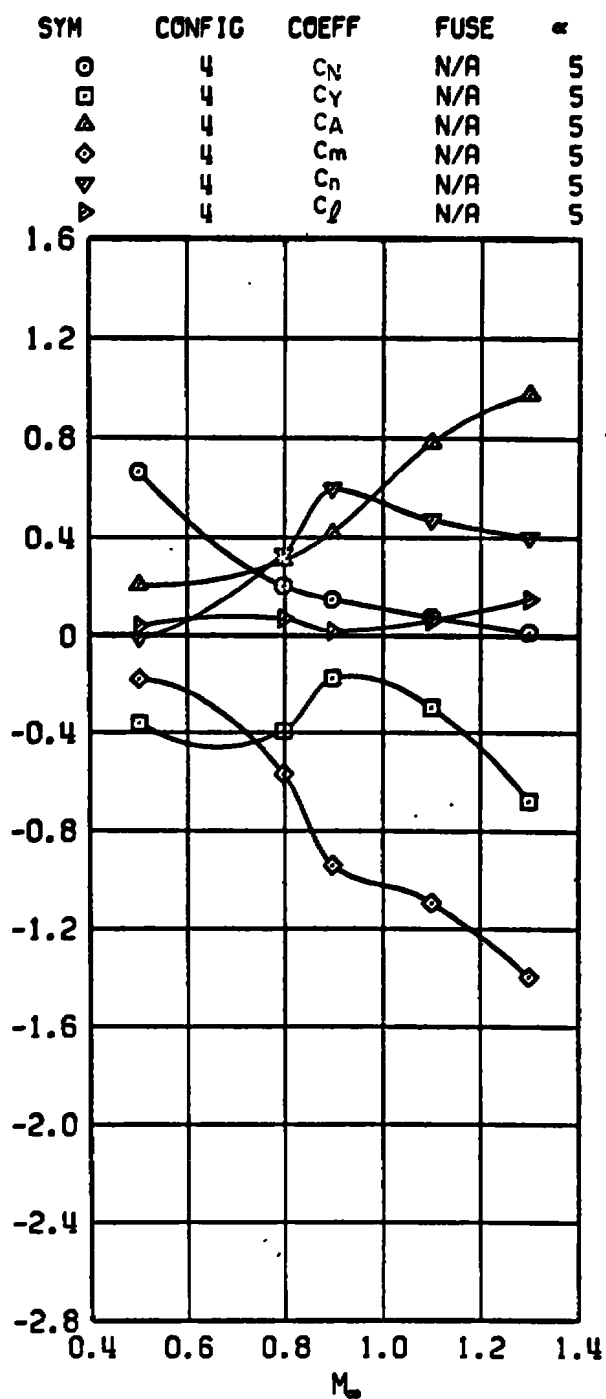
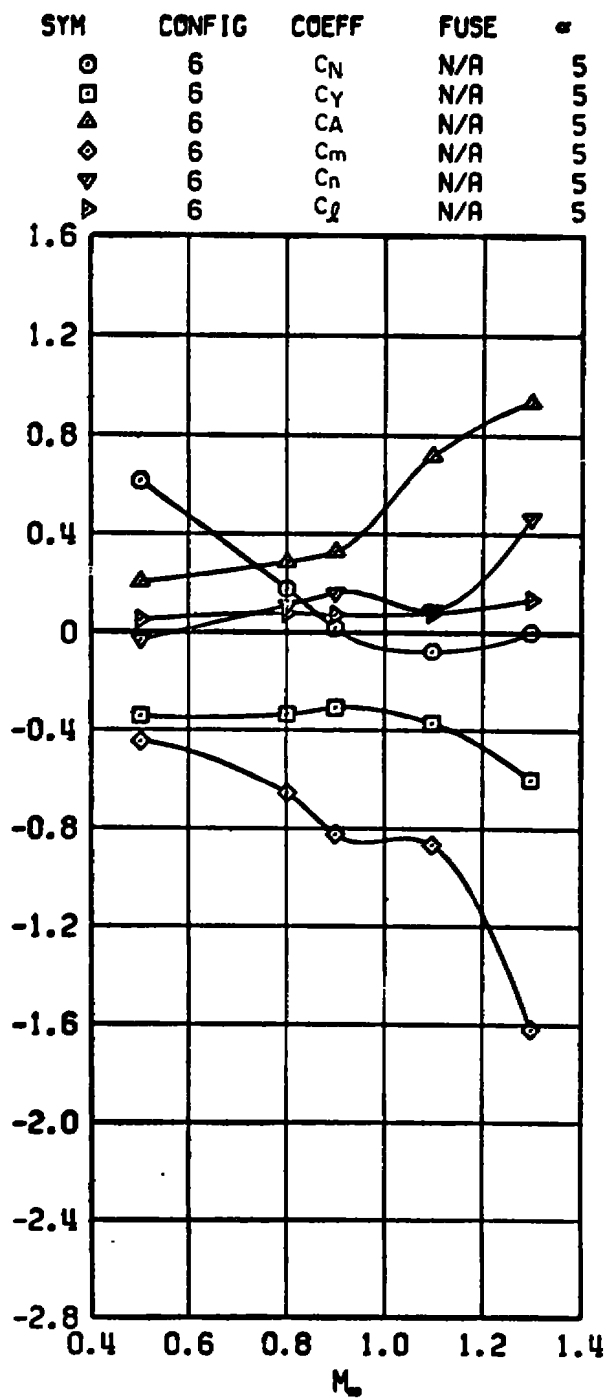


Figure 21. Carriage position airloads of the 14-in.-diam maximum volume bomb in the flow field of the wing-pylon-TER configuration, $\Delta\phi = 45$ deg.

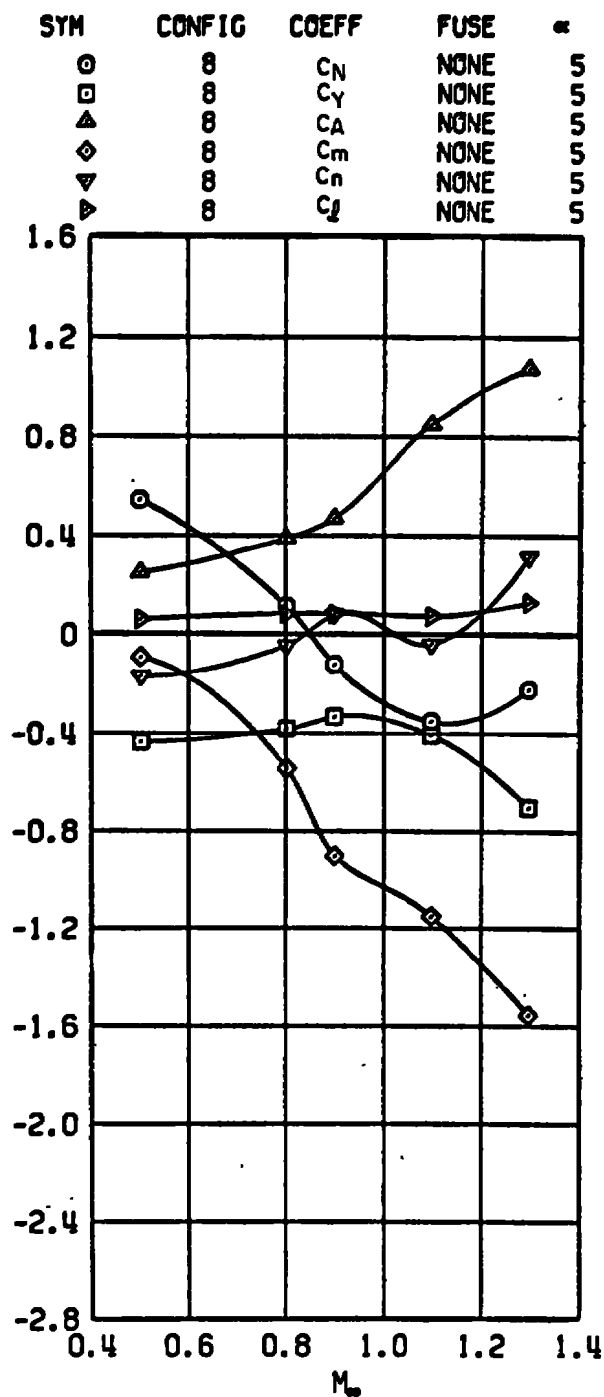


a. Standard M-117 bomb configuration

Figure 22. Carriage position airloads of the M-117 bombs in the flow field of the wing-pylon-TER configuration, $\Delta\phi = 0$, $\alpha = 5$ deg.

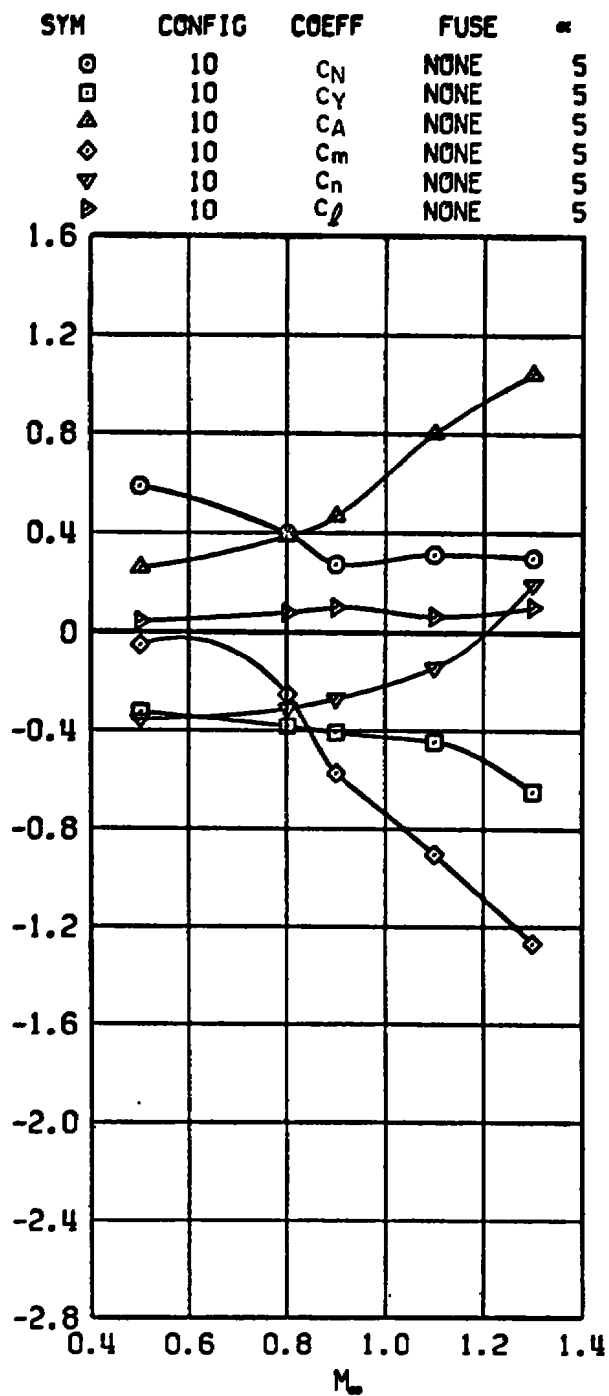


b. Modified M-117 bomb configuration
Figure 22. Concluded.

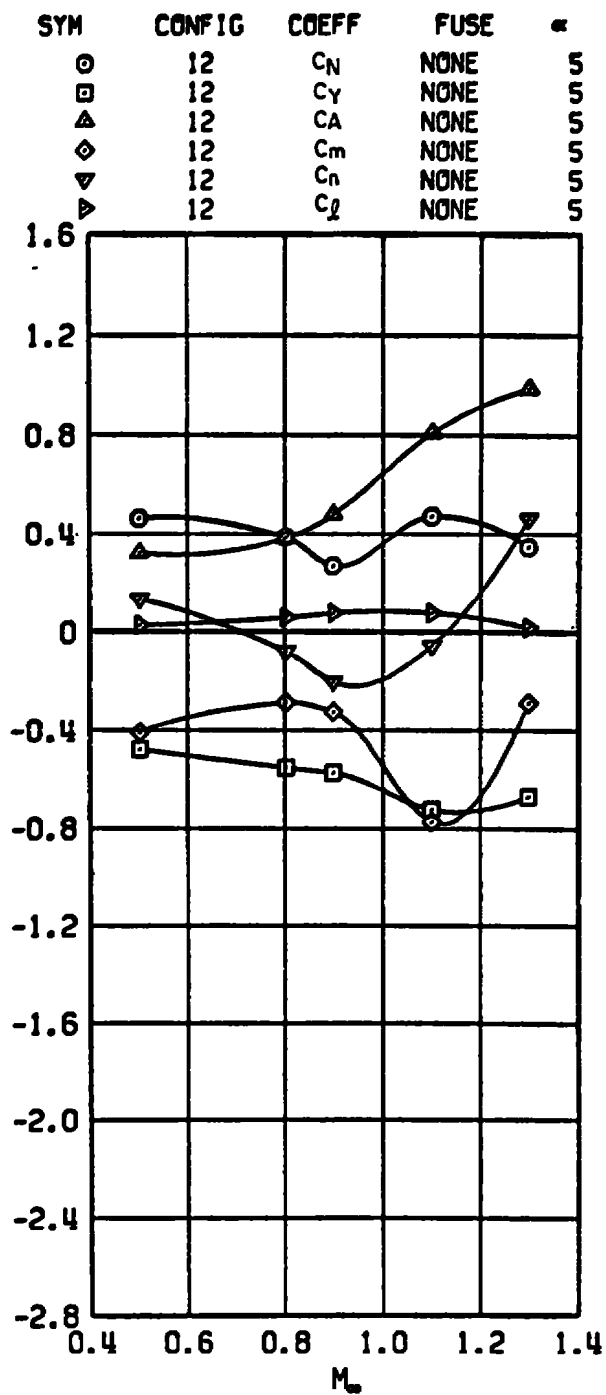


a. 16-in.-diam maximum volume bomb

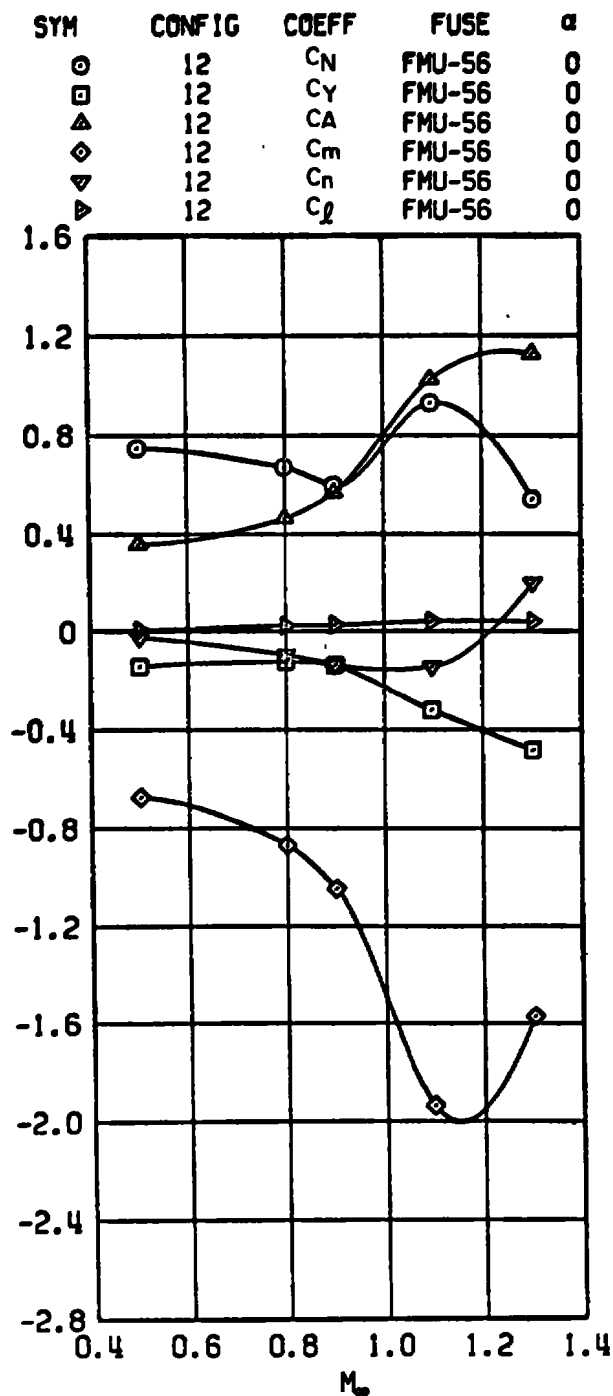
Figure 23. Carriage position airloads of the maximum volume bombs in the flow field of the wing-pylon-TER configuration, $\Delta\phi = 0$, $\alpha = 5$ deg.



b. 14-in.-diam maximum volume bomb
Figure 23. Continued.

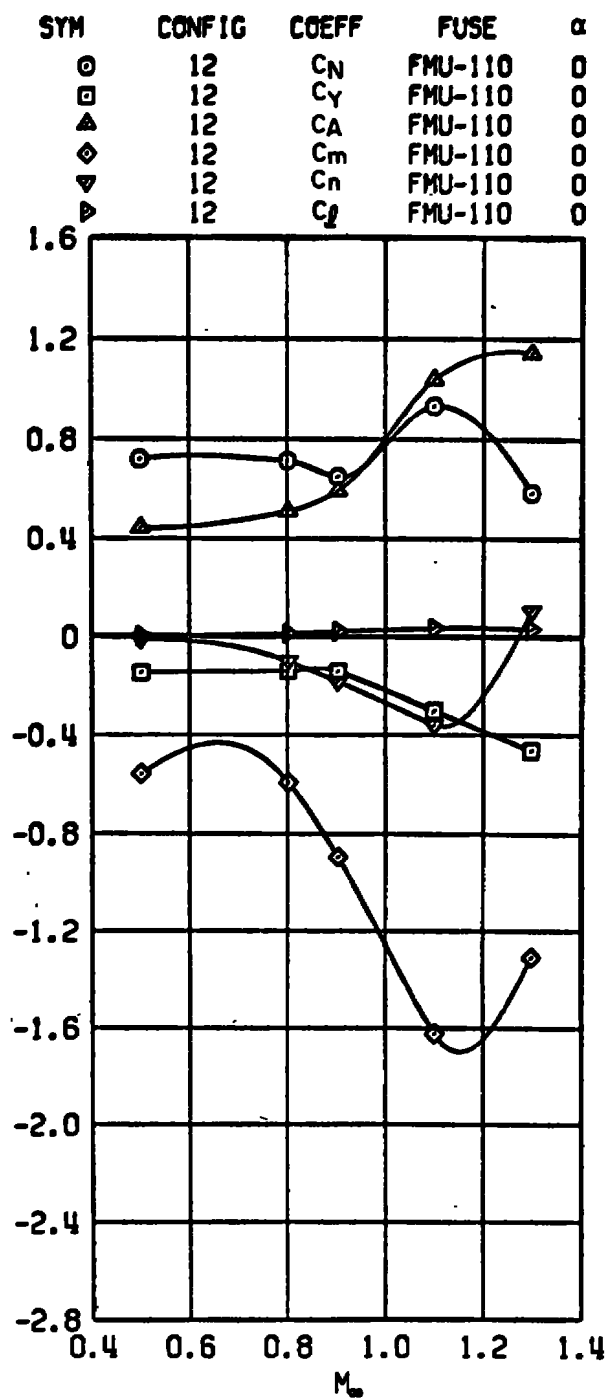


c. 12-in.-diam maximum volume bomb
Figure 23. Concluded.



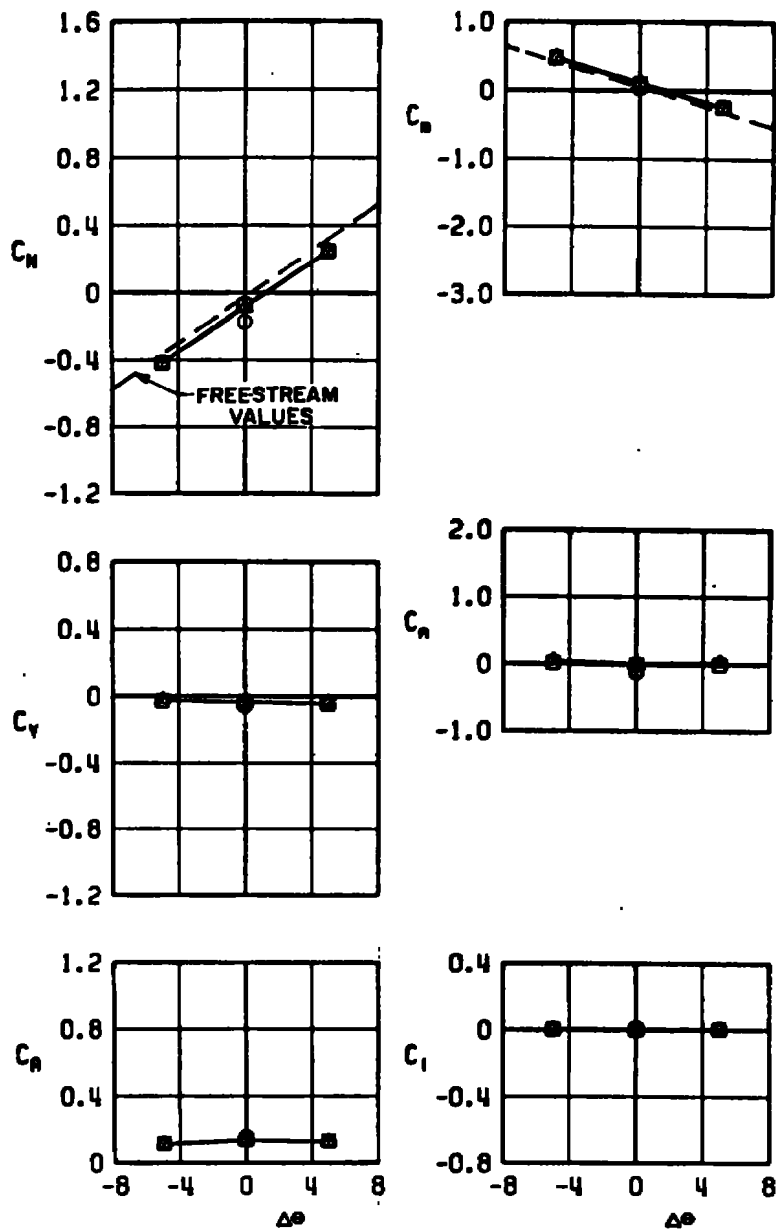
a. FMU-56

Figure 24. Carriage position airloads of the 12-in.-diam maximum volume bomb with fuse, in the flow field of the wing-pylon-TER configuration, $\Delta\phi = 0$.



b. FMU-110
Figure 24. Concluded.

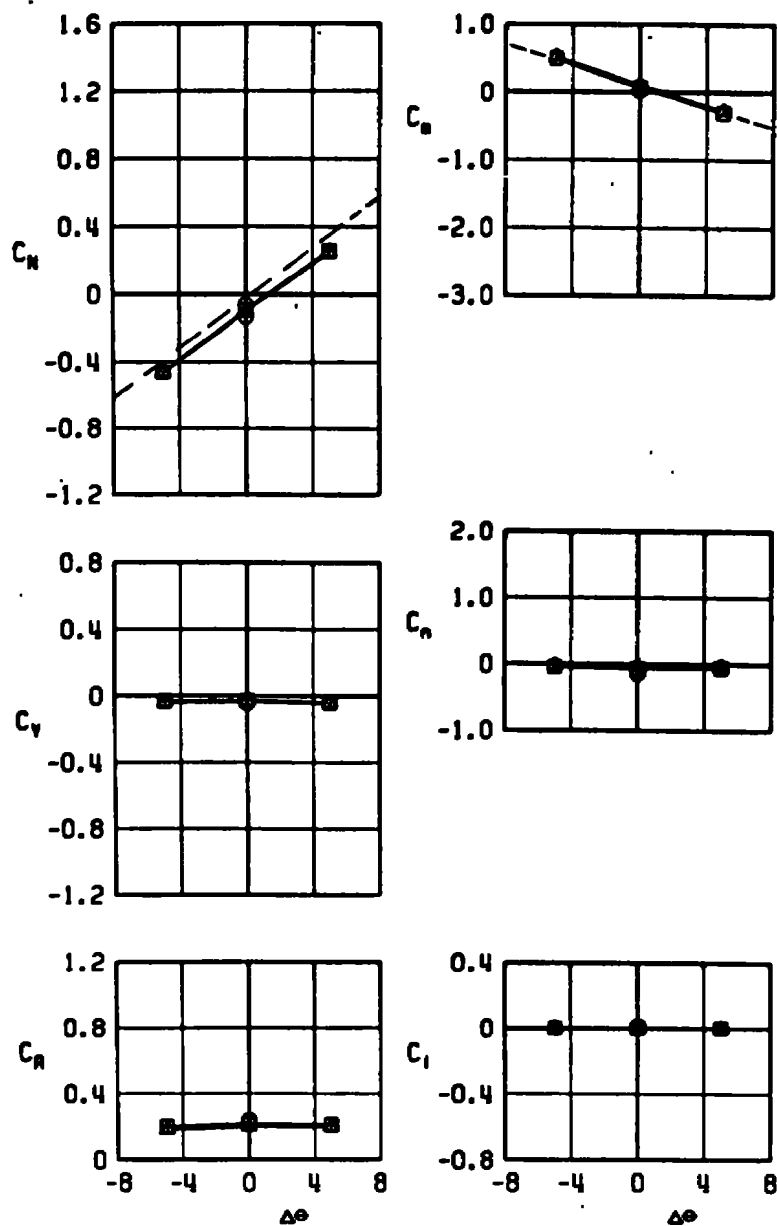
SYM	M_∞	α	CONFIG	FUSE	Z/D
○	0.50	0	3	N/A	0
□	0.50	0	3	N/A	0.5
▲	0.50	0	3	N/A	1.0



a. $M_\infty = 0.5$

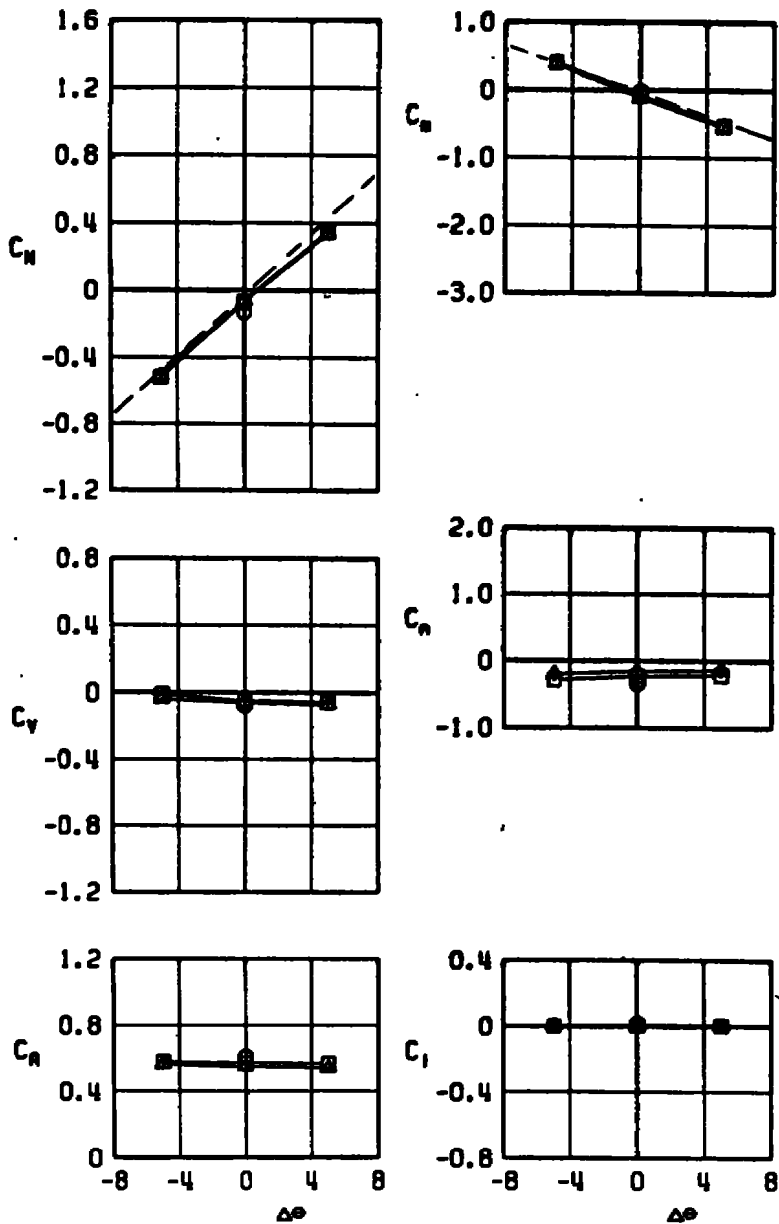
Figure 25. Grid survey airloads of the standard M-117 bomb configuration in the flow field of the wing-pylon (without TER) configuration, $\Delta\phi = 0$.

SYM	M_∞	α	CONFIG	FUSE	Z/D
○	0.90	0	3	N/A	0
□	0.90	0	3	N/A	0.5
△	0.90	0	3	N/A	1.0



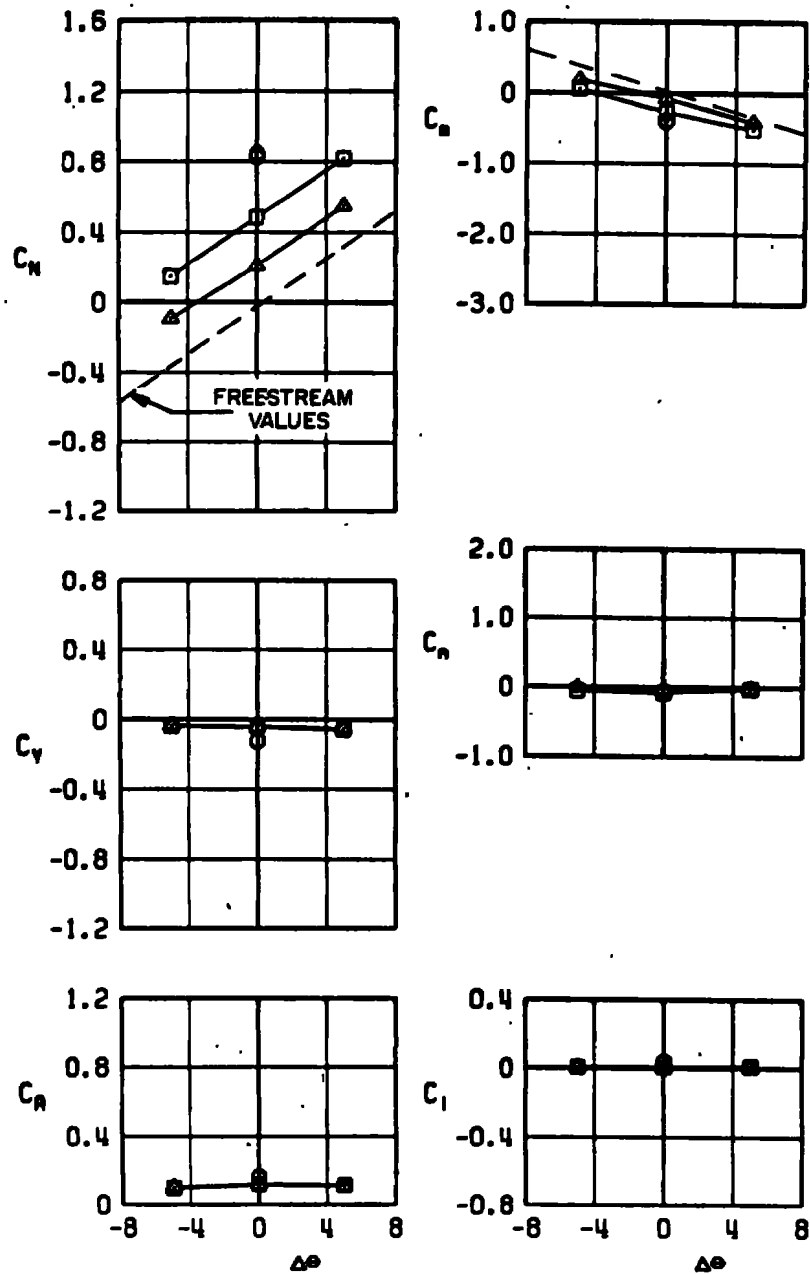
b. $M_\infty = 0.9$
Figure 25. Continued.

SYM	M_∞	α	CONFIG	FUSE	Z/D
○	1.10	0	3	N/A	0
□	1.10	0	3	N/A	0.5
△	1.10	0	3	N/A	1.0



c. $M_\infty = 1.1$
Figure 25. Concluded.

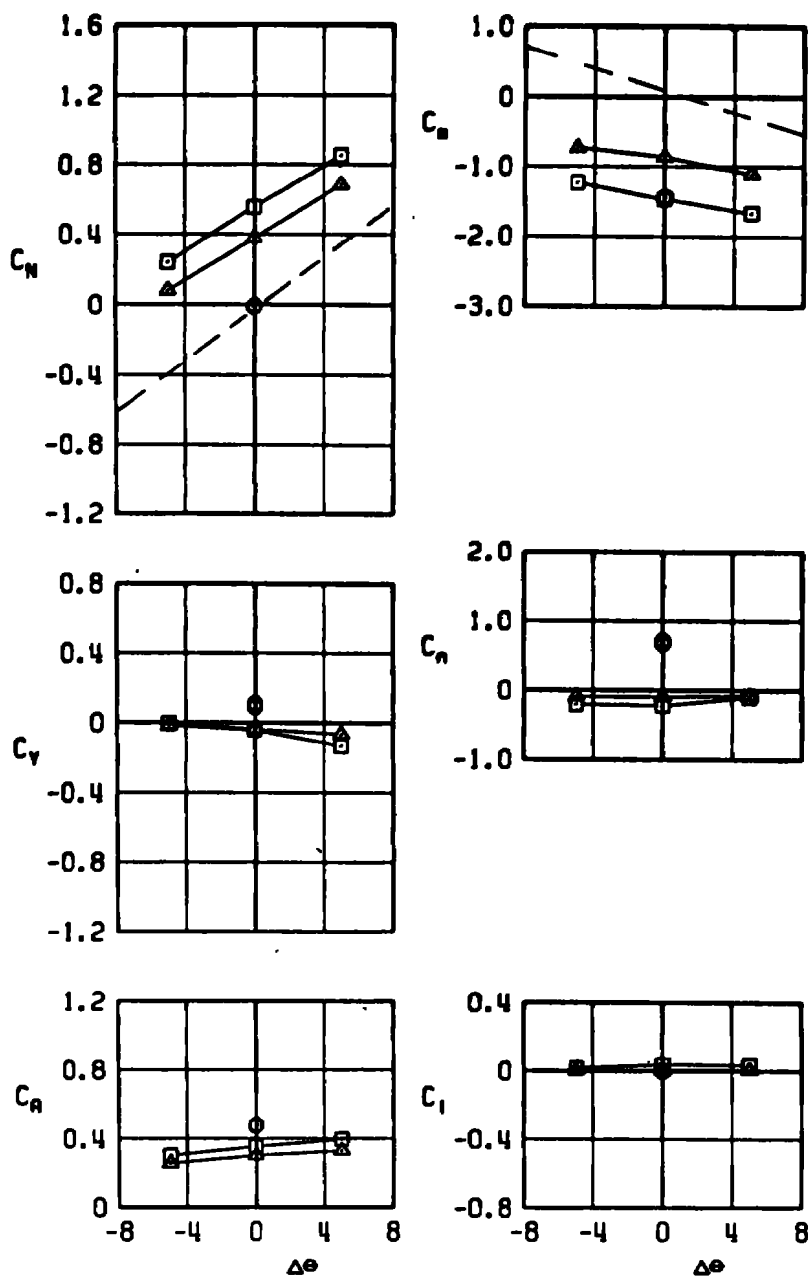
SYM	M_∞	α	CONFIG	FUSE	Z/D
○	0.50	0	4	N/A	0
□	0.50	0	4	N/A	0.5
△	0.50	0	4	N/A	1.0



a. $M_\infty = 0.5$

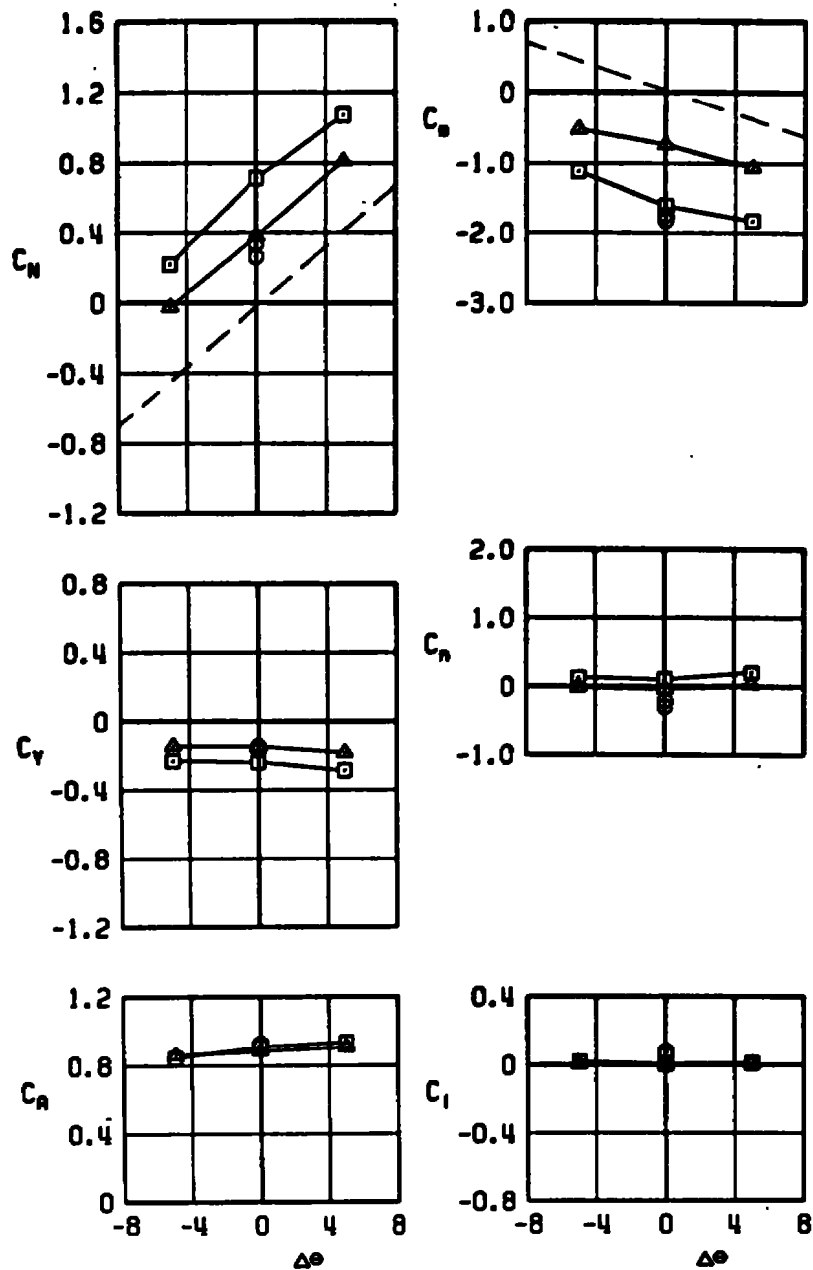
Figure 26. Grid survey airloads of the standard M-117 bomb configuration in the flow field of the wing-pylon-TER configuration, $\Delta\phi = 0$.

SYM	M_∞	α	CONFIG	FUSE	Z/O
○	0.90	0	4	N/A	0
□	0.90	0	4	N/A	0.5
△	0.90	0	4	N/A	1.0



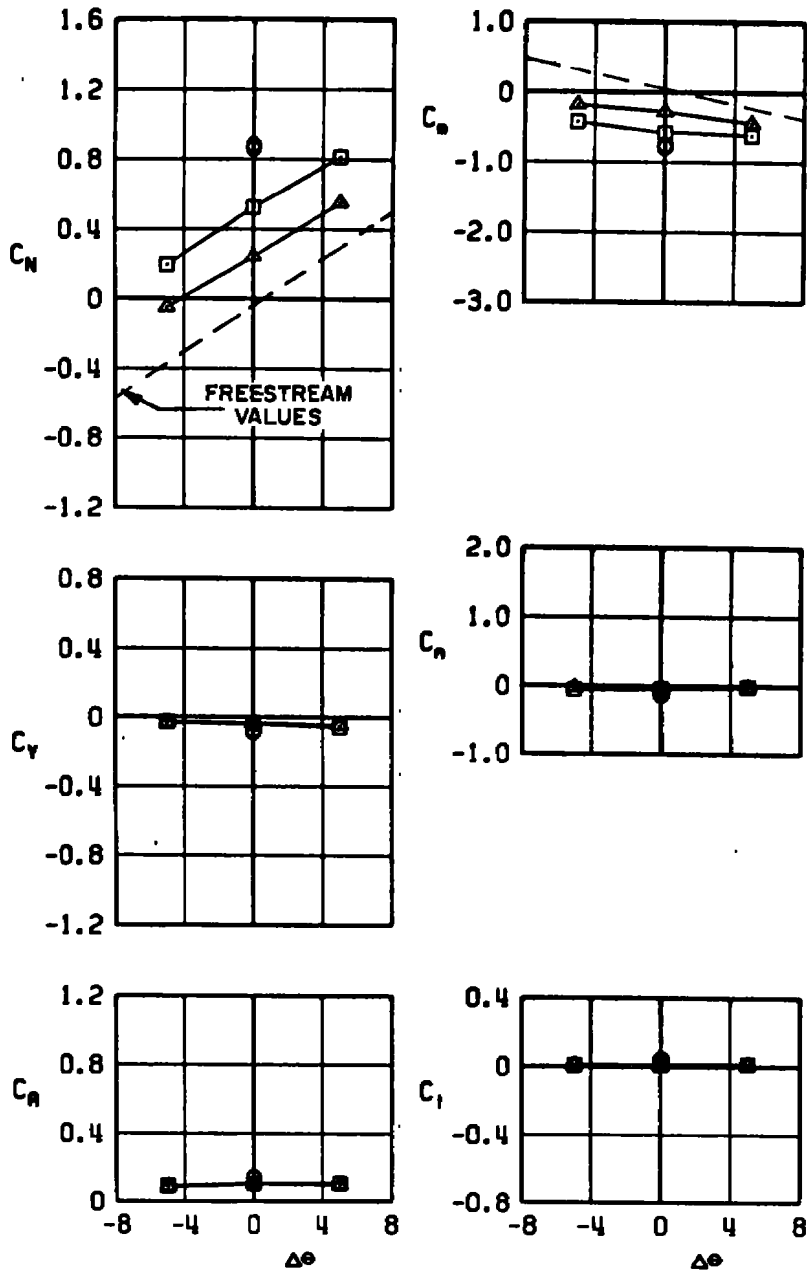
b. $M_\infty = 0.9$
Figure 26. Continued.

SYM	M_∞	α	CONFIG	FUSE	Z/D
○	1.10	0	4	N/A	0
□	1.10	0	4	N/A	0.5
△	1.10	0	4	N/A	1.0



c. $M_\infty = 1.1$
Figure 26. Concluded.

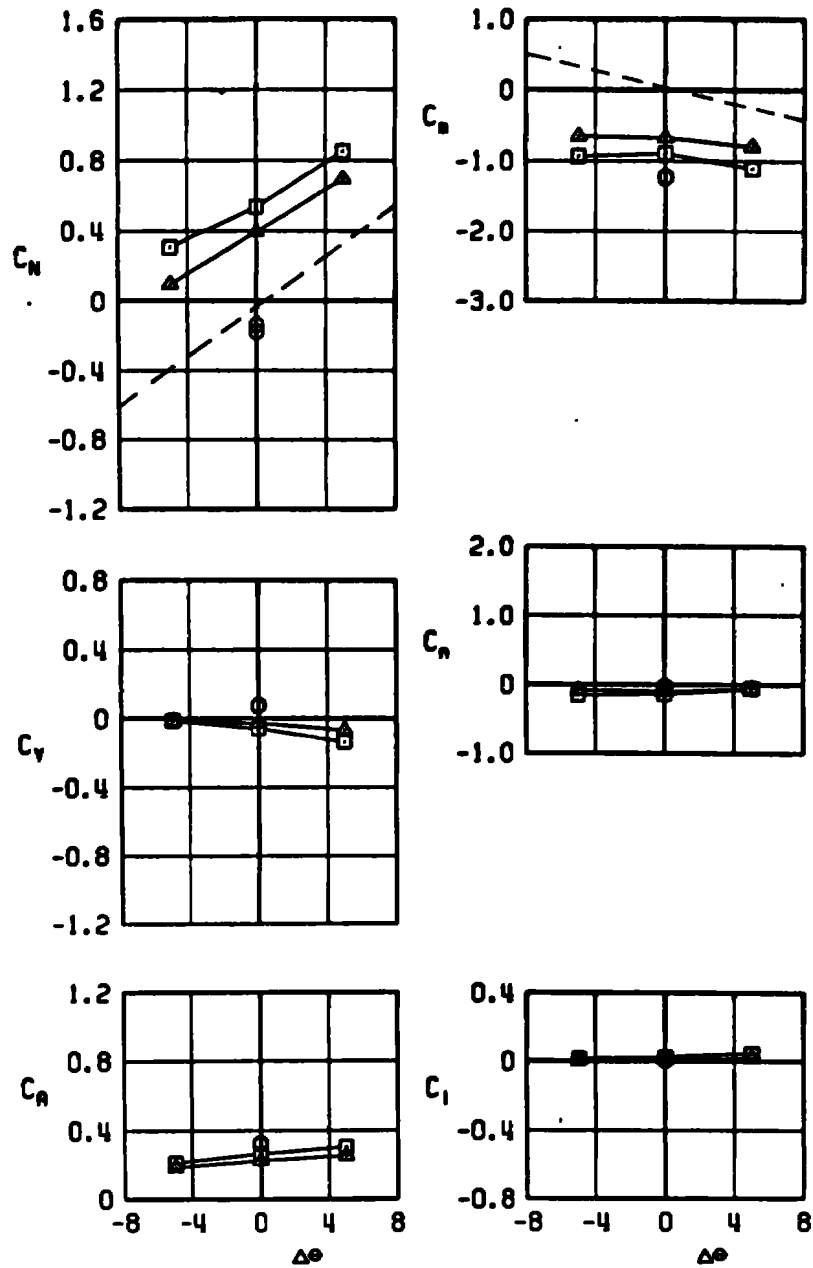
SYM	M_∞	α	CONFIG	FUSE	Z/D
○	0.50	0	6	N/R	0
□	0.50	0	6	N/R	0.5
△	0.50	0	6	N/R	1.0



a. $M_\infty = 0.5$

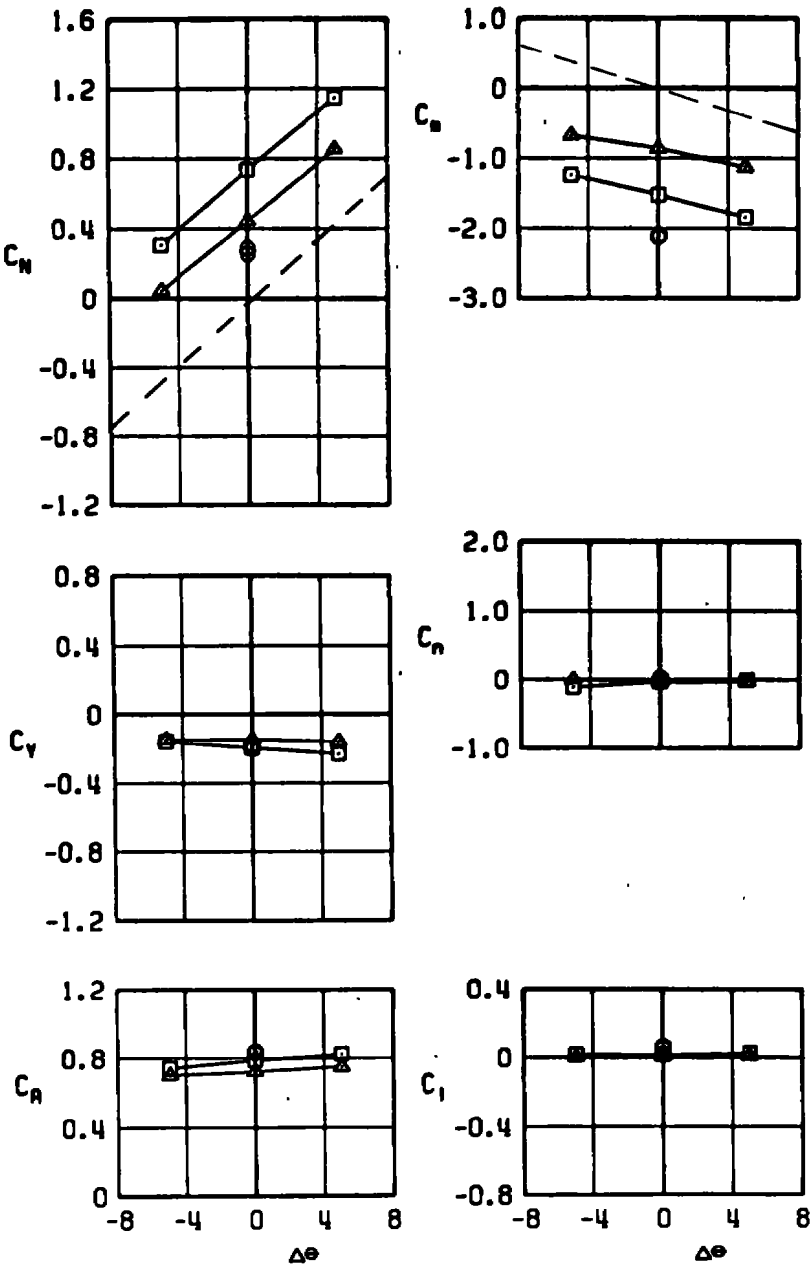
Figure 27. Grid survey airloads of the modified M-117 bomb configuration in the flow field of the wing-pylon-TER configuration, $\Delta\phi = 0$.

SYM	M_∞	α	CONFIG	FUSE	Z/D
○	0.90	0	6	N/A	0
□	0.90	0	6	N/A	0.5
△	0.90	0	6	N/A	1.0



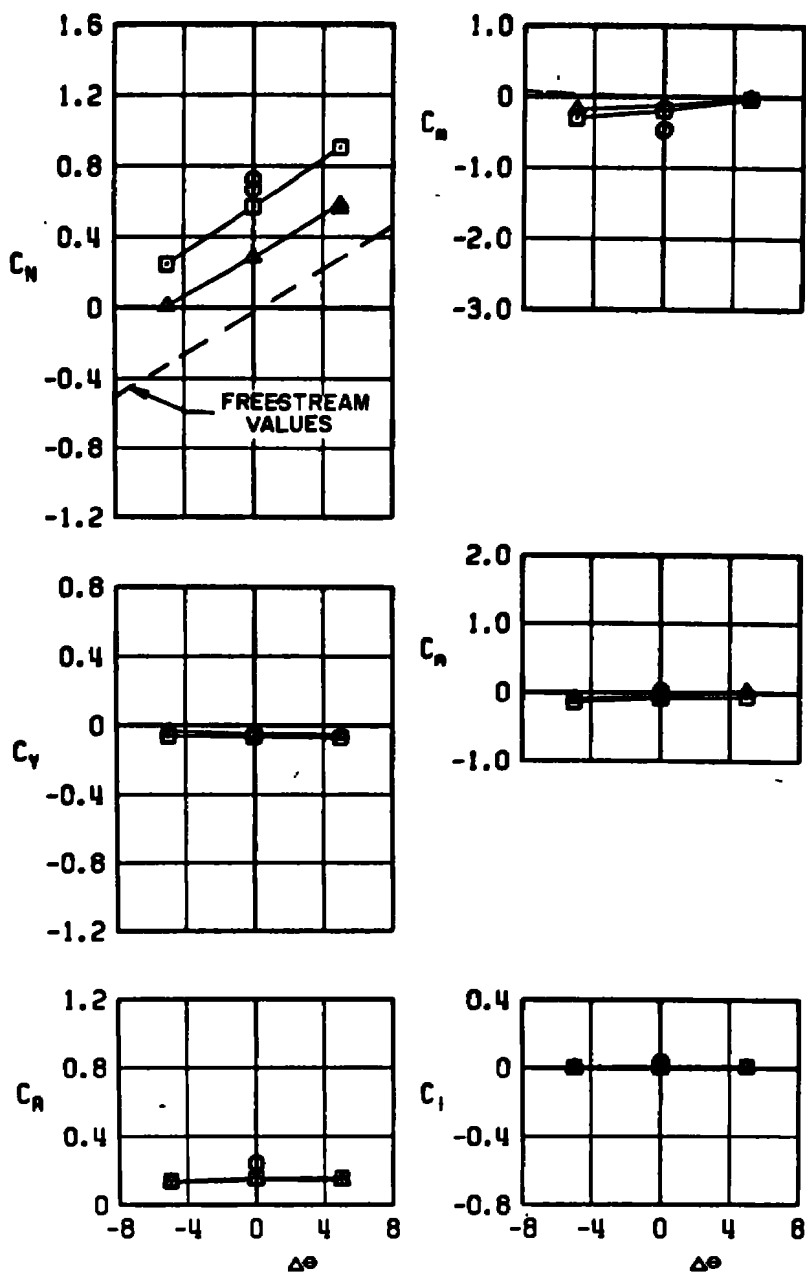
b. $M_\infty = 0.9$
Figure 27. Continued.

SYM	M _∞	α	CONFIG	FUSE	Z/D
○	1.10	0	6	N/A	0
□	1.10	0	6	N/A	0.5
▲	1.10	0	6	N/A	1.0



c. $M_\infty = 1.1$
Figure 27. Concluded.

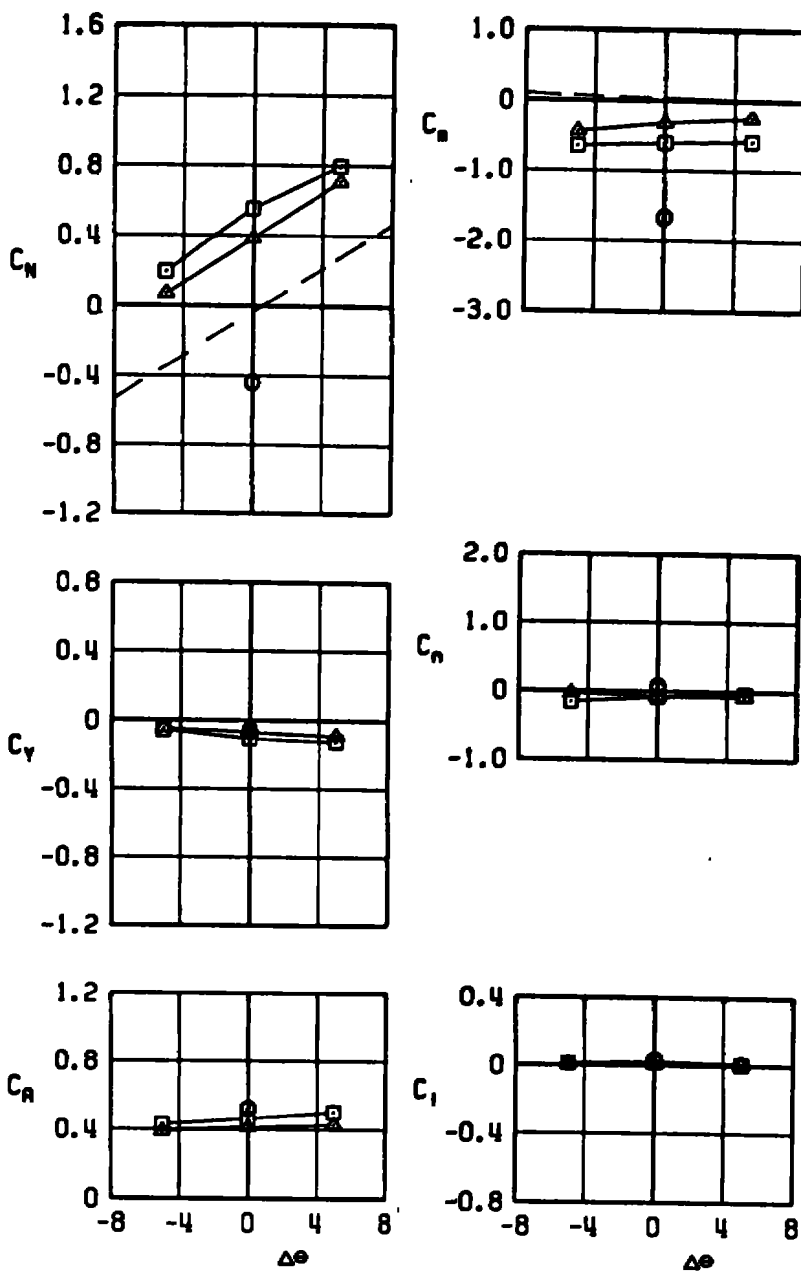
SYM	M_∞	α	CONFIG	FUSE	Z/D
○	0.50	0	8	N/A	0
□	0.50	0	8	N/A	0.5
▲	0.50	0	8	N/A	1.0



a. $M_\infty = 0.5$

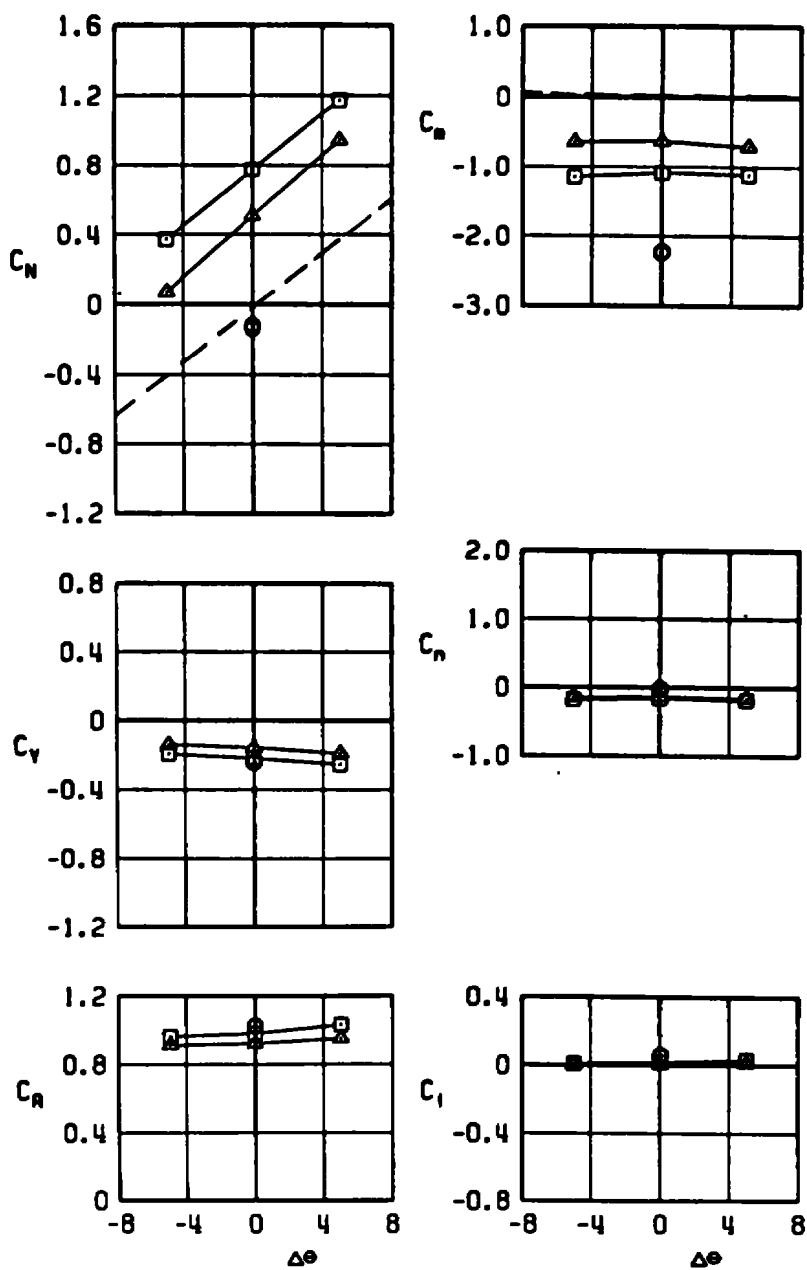
Figure 28. Grid survey airloads of the 16-in.-diam maximum volume bomb in the flow field of the wing-pylon-TER configuration, $\Delta\phi = 0$.

SYM	M_∞	α	CONFIG	FUSE	Z/D
○	0.90	0	8	NONE	0
□	0.90	0	8	NONE	0.5
△	0.90	0	8	NONE	1.0



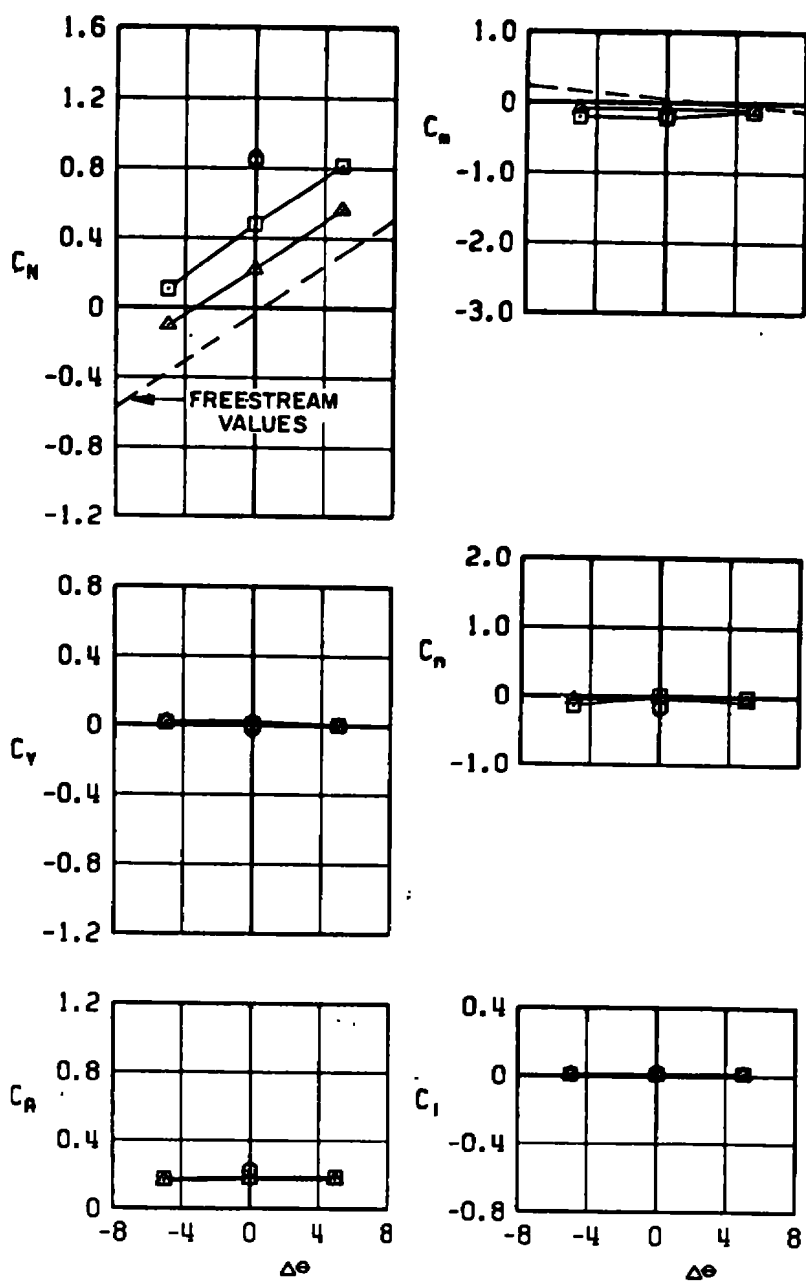
b. $M_\infty = 0.9$
Figure 28. Continued.

SYM	M_∞	α	CONFIG	FUSE	Z/D
○	1.10	0	8	NONE	0
□	1.10	0	8	NONE	0.5
△	1.10	0	8	NONE	1.0



c. $M_\infty = 1.1$
Figure 28. Concluded.

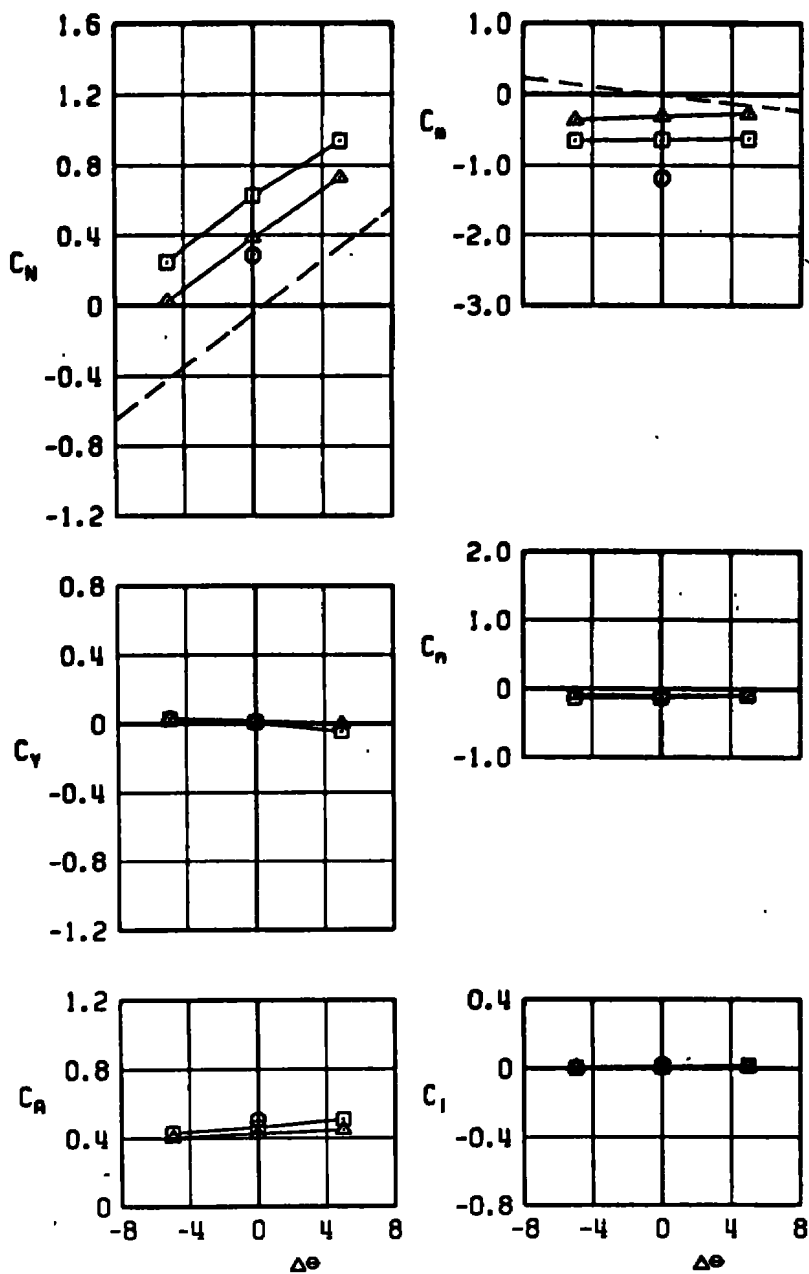
SYM	M_∞	α	CONFIG	FUSE	Z/D
○	0.50	0	10	NONE	0
□	0.50	0	10	NONE	0.5
△	0.50	0	10	NONE	1.0



a. $M_\infty = 0.5$

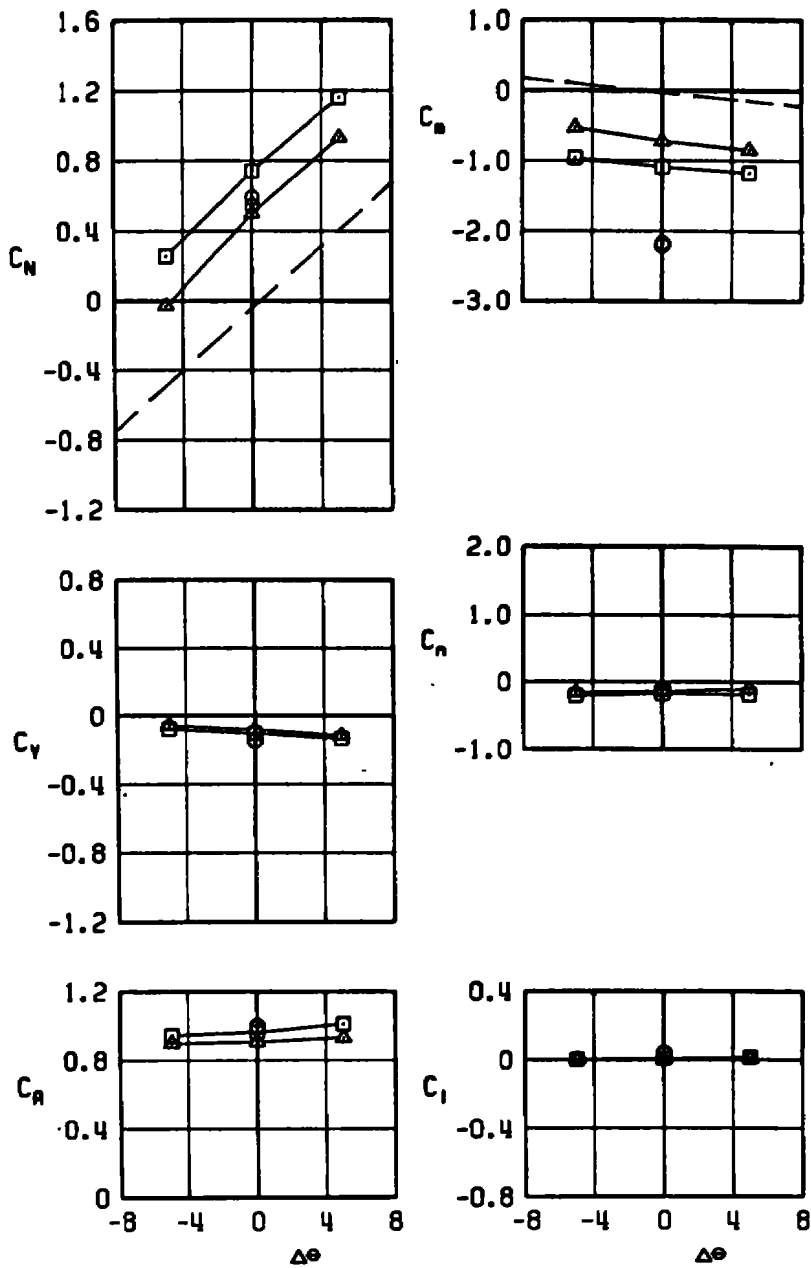
Figure 29. Grid survey airloads of the 14-in.-diam maximum volume bomb in the flow field of the wing-pylon-TER configuration, $\Delta\phi = 0$.

SYM	M_∞	α	CONFIG	FUSE	Z/O
○	0.90	0	10	NONE	0
□	0.90	0	10	NONE	0.5
▲	0.90	0	10	NONE	1.0



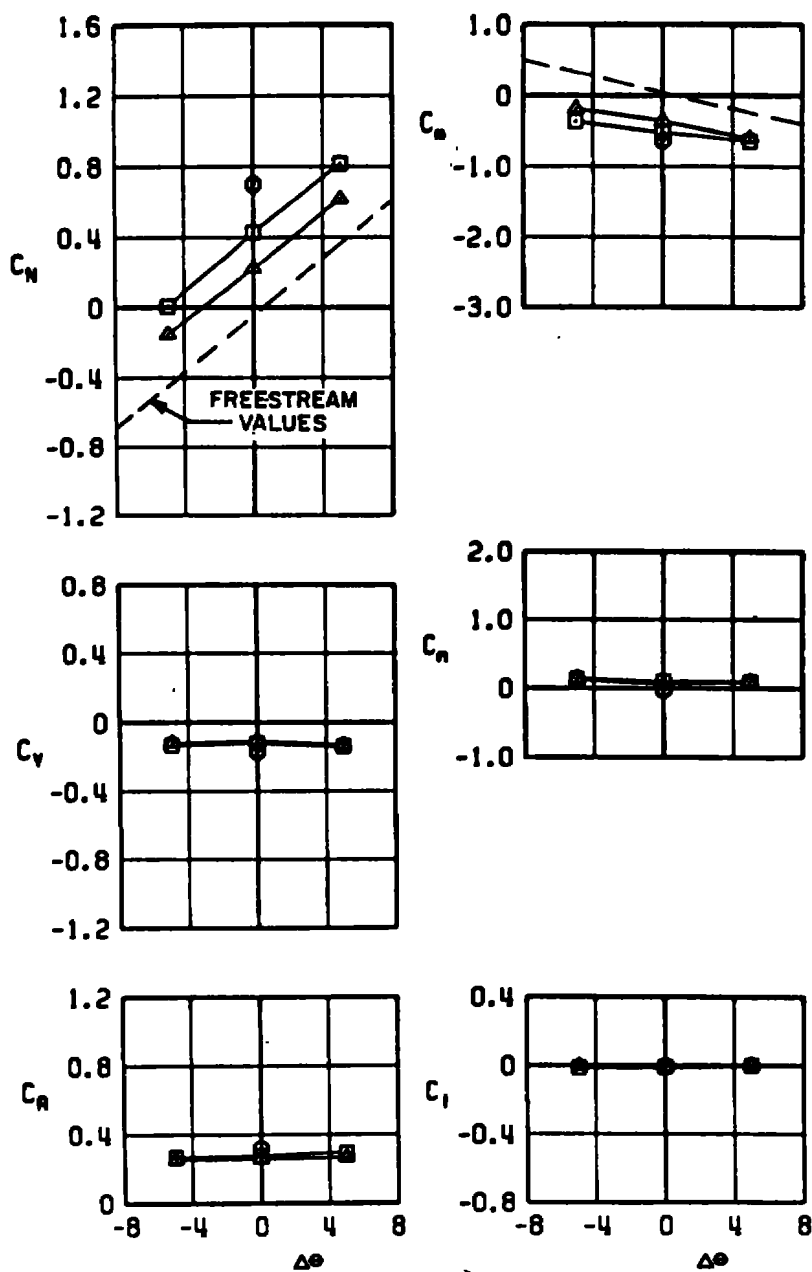
b. $M_\infty = 0.9$
Figure 29. Continued.

SYM	M_∞	α	CONFIG	FUSE	Z/D
○	1.10	0	10	NONE	0
□	1.10	0	10	NONE	0.5
△	1.10	0	10	NONE	1.0



c. $M_\infty = 1.1$
Figure 29. Concluded.

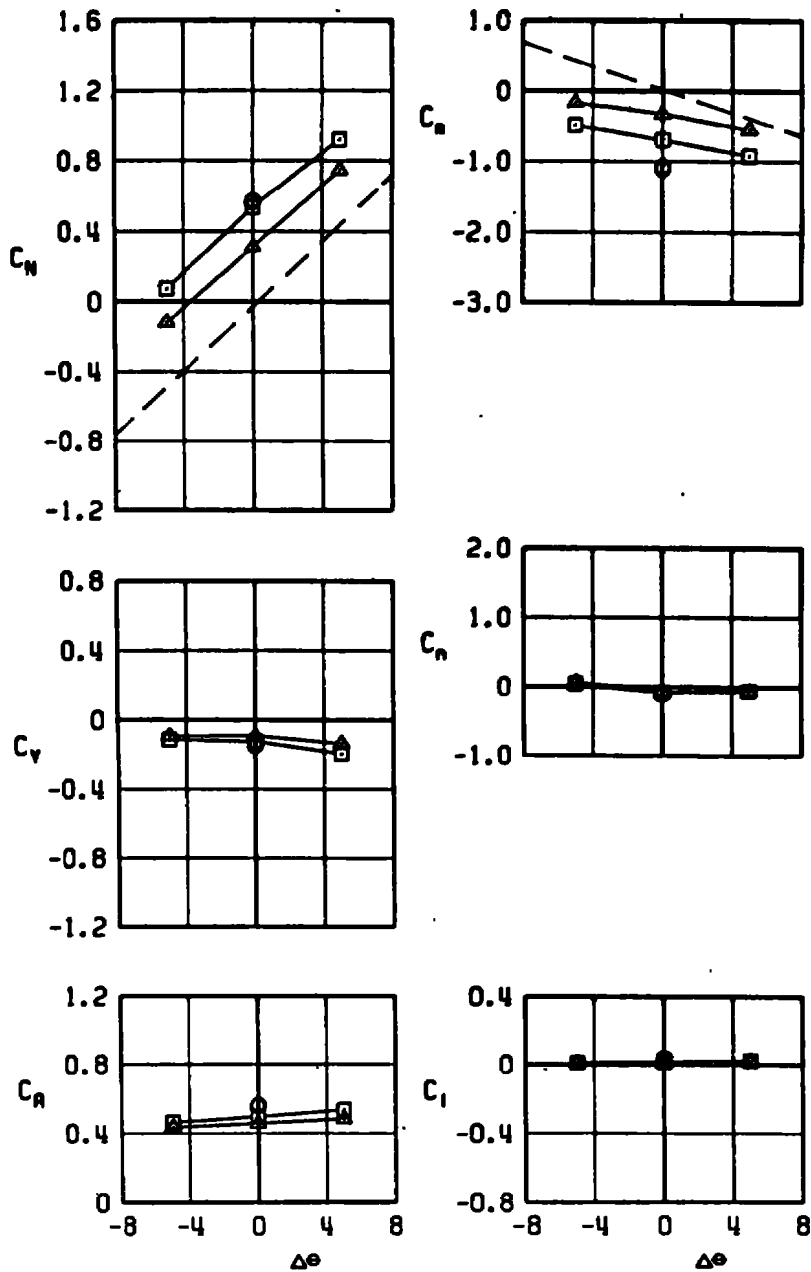
SYM	M_∞	α	CONFIG	FUSE	Z/D
○	0.50	0	12	NONE	0
□	0.50	0	12	NONE	0.5
▲	0.50	0	12	NONE	1.0



a. $M_\infty = 0.5$

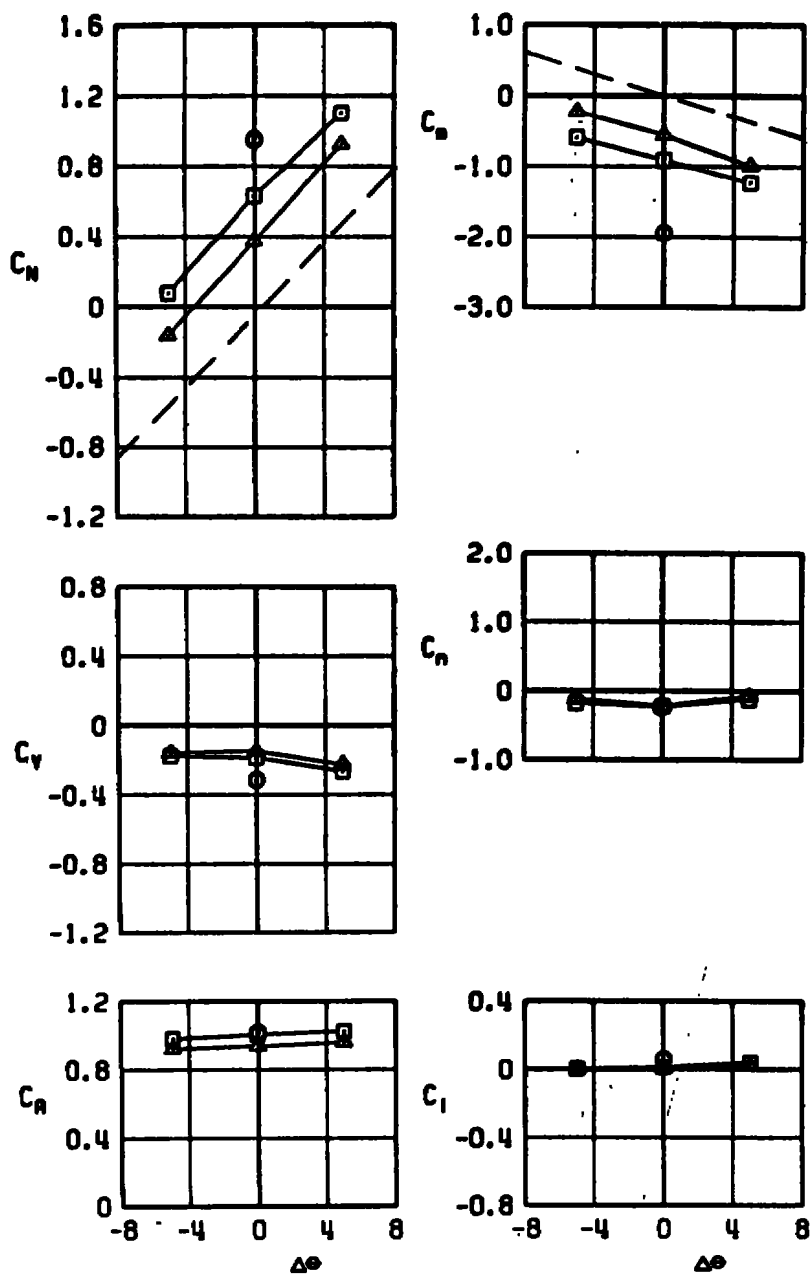
Figure 30. Grid survey airloads of the 12-in.-diam maximum volume bomb in the flow field of the wing-pylon-TER configuration, $\Delta\phi = 0$.

SYM	M_∞	α	CONFIG	FUSE	Z/D
○	0.90	0	12	NONE	0
□	0.90	0	12	NONE	0.5
△	0.90	0	12	NONE	1.0



b. $M_\infty = 0.9$
Figure 30. Continued.

SYM	M_∞	α	CONFIG	FUSE	Z/D
○	1.10	0	12	NONE	0
□	1.10	0	12	NONE	0.5
△	1.10	0	12	NONE	1.0



c. $M_\infty = 1.1$
Figure 30. Concluded.

SYM	CONFIG	COEFF	FUSE	α	$\Delta\theta$	Z/D
○	10	C_N	N/A	0	0	0.5
□	10	C_Y	N/A	0	0	0.5
△	10	C_A	N/A	0	0	0.5
◇	10	C_m	N/A	0	0	0.5
▽	10	C_n	N/A	0	0	0.5
▴	10	C_l	N/A	0	0	0.5

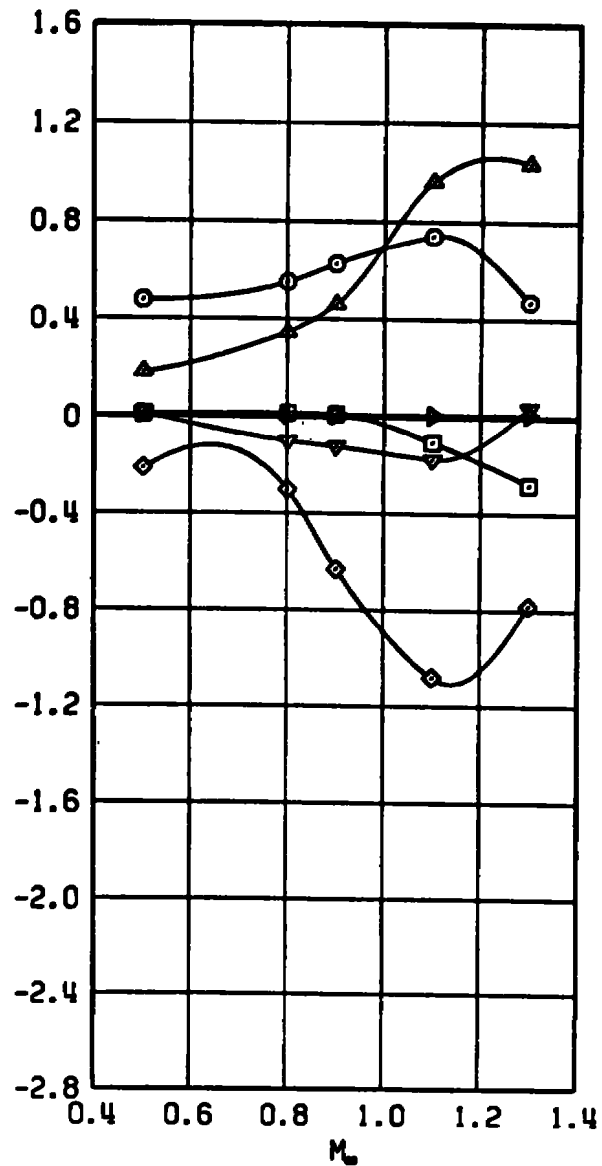
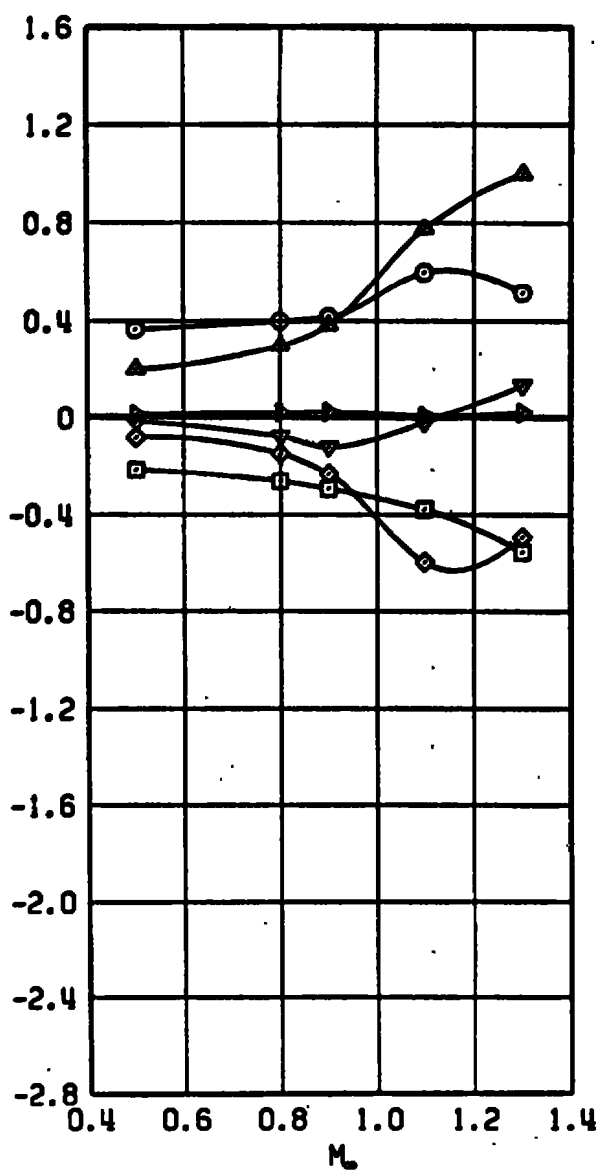
a. $\alpha = 0$

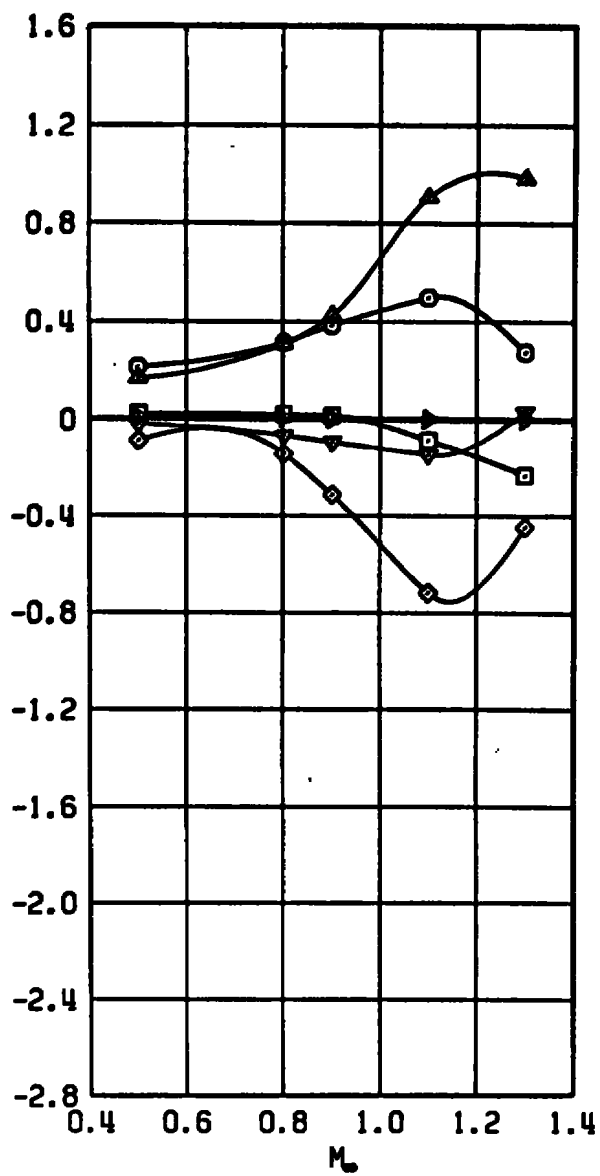
Figure 31. Grid survey airloads of the 14-in.-diam maximum volume bomb in the flow field of the wing-pylon-TER configuration, $\Delta\phi = 0$, $Z/D = 0.5$.

SYM	CONFIG	COEFF	FUSE	α	$\Delta\theta$	Z/D
○	10	C _N	N/A	5	0	0.5
□	10	C _Y	N/A	5	0	0.5
△	10	C _A	N/A	5	0	0.5
◇	10	C _m	N/A	5	0	0.5
▽	10	C _n	N/A	5	0	0.5
▽	10	C _l	N/A	5	0	0.5



b. $\alpha = 5^\circ$
Figure 31. Concluded.

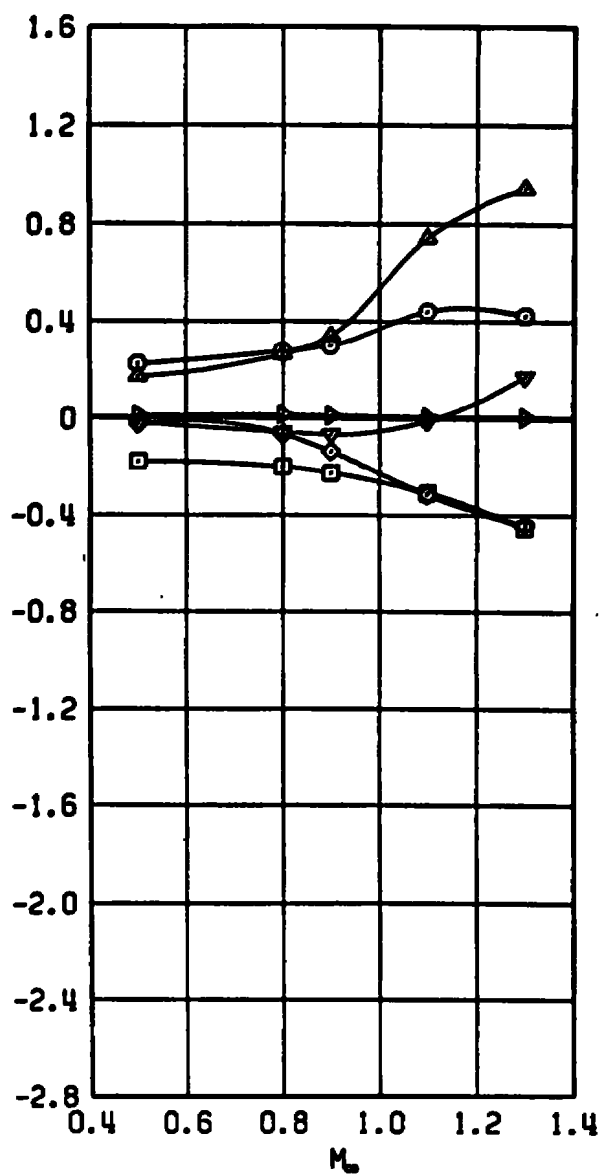
SYM	CONFIG	COEFF	FUSE	α	$\Delta\theta$	Z/D
○	10	C _N	N/A	0	0	1.0
□	10	C _Y	N/A	0	0	1.0
▲	10	C _A	N/A	0	0	1.0
◇	10	C _m	N/A	0	0	1.0
▼	10	C _n	N/A	0	0	1.0
▽	10	C _g	N/A	0	0	1.0



a. $\alpha = 0$

Figure 32. Grid survey airloads of the 14-in.-diam maximum volume bomb in the flow field of the wing-pylon-TER configuration, $\Delta\phi = 0$, $Z/D = 1.0$.

SYM	CONFIG	COEFF	FUSE	α	$\Delta\theta$	Z/D
○	10	C _N	N/A	5	0	1.0
□	10	C _Y	N/A	5	0	1.0
△	10	C _A	N/A	5	0	1.0
◇	10	C _m	N/A	5	0	1.0
▽	10	C _n	N/A	5	0	1.0
▴	10	C _l	N/A	5	0	1.0



b. $\alpha = 5$ deg
Figure 32. Concluded.

SYM	CONFIG	COEFF	FUSE	α	$\Delta\theta$	z/D	$\Delta\phi$
○	4	CN	NONE	0	0	0.5	0
□	5	CN	NONE	0	0	0.5	45
▲	4	Cm	NONE	0	0	0.5	0
◄	5	Cm	NONE	0	0	0.5	45
▼	4	CN	NONE	0	0	1.0	0
▷	5	CN	NONE	0	0	1.0	45
◇	4	Cm	NONE	0	0	1.0	0
♣	5	Cm	NONE	0	0	1.0	45

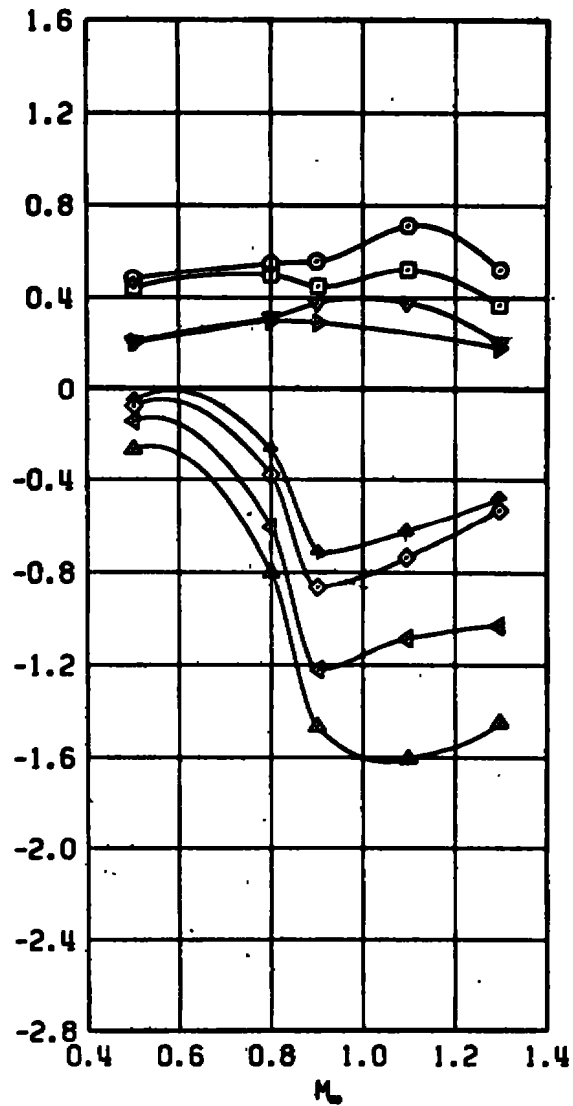


Figure 33. Effects of roll orientation on the normal-force and pitching-moment coefficients of the standard M-117 bomb configuration.

SYM	CONFIG	COEFF	FUSE	α	$\Delta\theta$	z/D
○	12	CN	NONE	0	0	0.5
□	12	CN	FMU-110	0	0	0.5
▲	12	Cm	NONE	0	0	0.5
◀	12	Cm	FMU-110	0	0	0.5
▼	12	CN	NONE	0	0	1.0
▷	12	CN	FMU-110	0	0	1.0
◇	12	Cm	NONE	0	0	1.0
♣	12	Cm	FMU-110	0	0	1.0

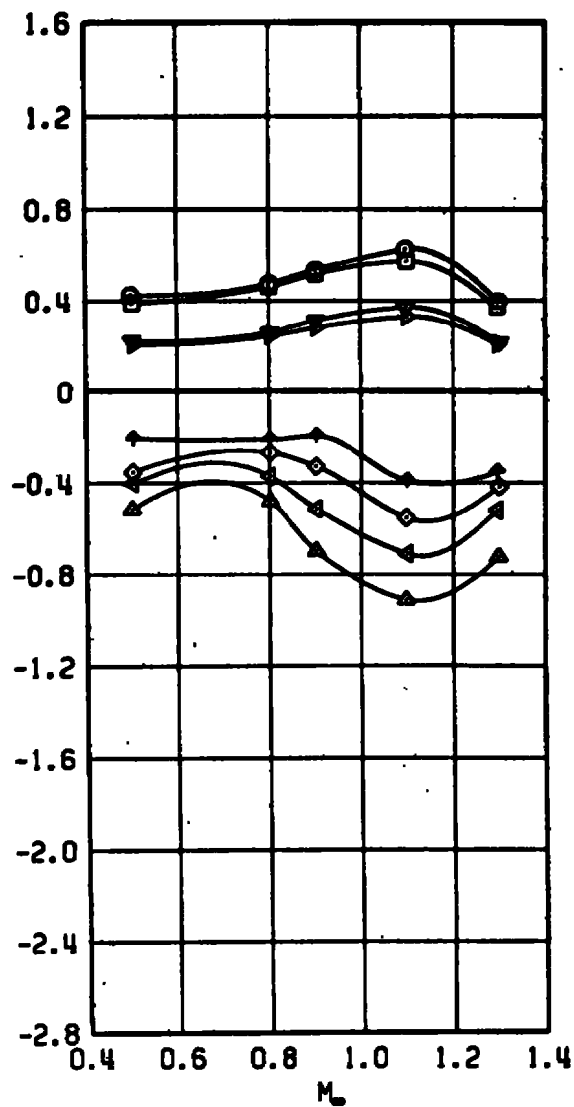
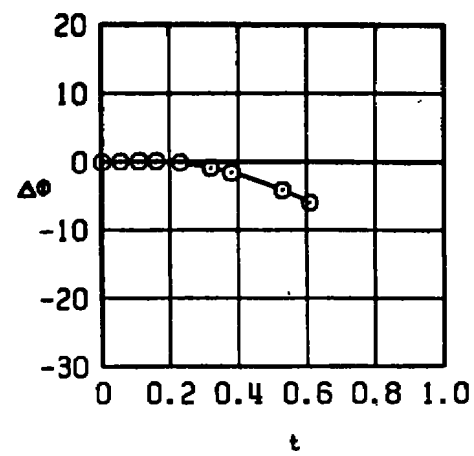
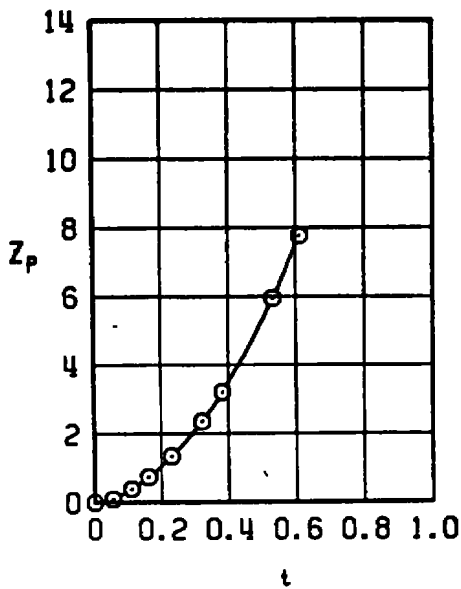
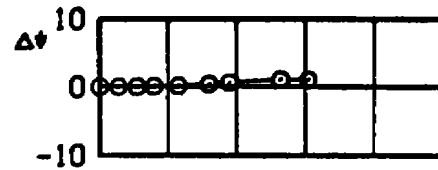
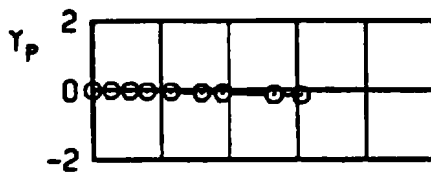
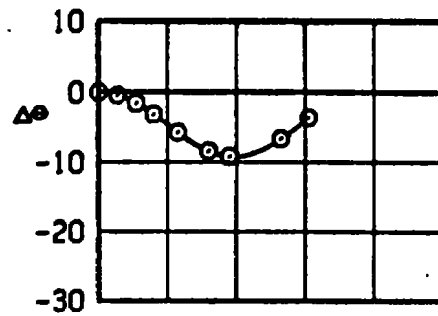
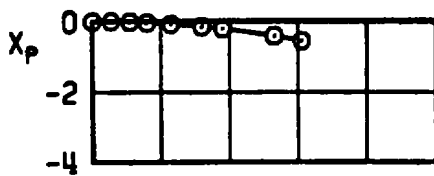


Figure 34. Effects of the FMU-110 fuse on the normal-force and pitching-moment coefficients of the 12-in.-diam maximum volume bomb.

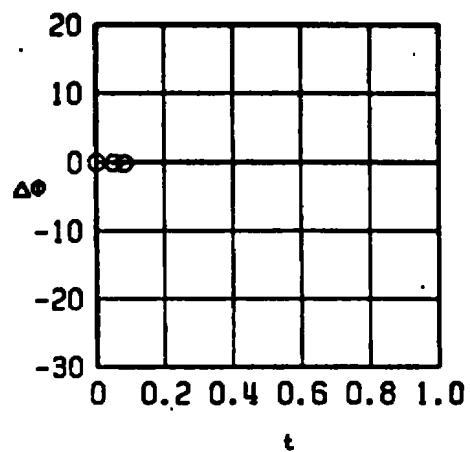
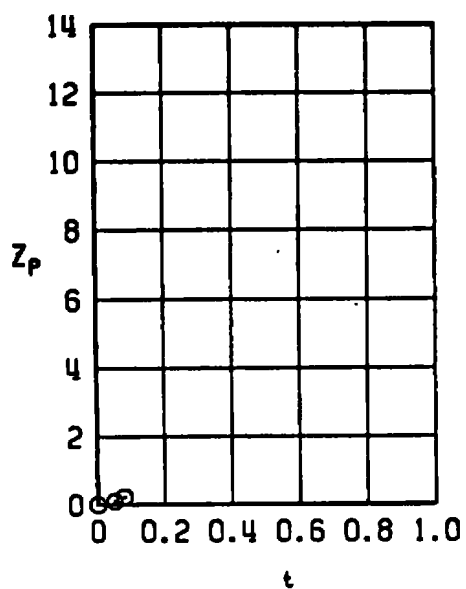
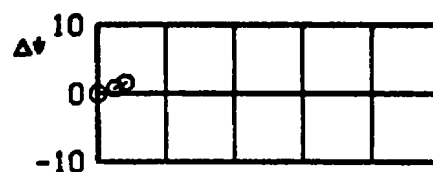
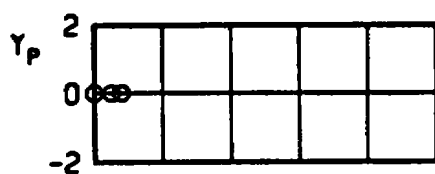
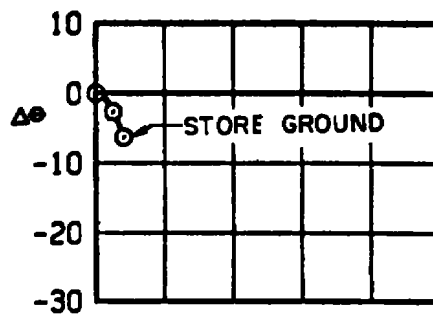
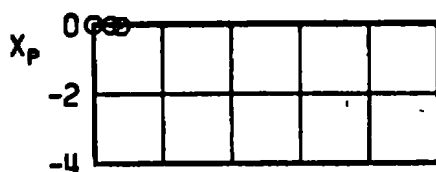
SYM	M_∞	α	CONFIG
○	0.50	0	4



a. $M_\infty = 0.5$

Figure 35. Trajectory data for the standard M-117 bomb configuration.

SYM	M_∞	α	CONFIG
⊙	0.80	0	4



b. $M_\infty = 0.8$
Figure 35. Concluded.

SYM	M_∞	α	CONFIG
○	0.50	0	6

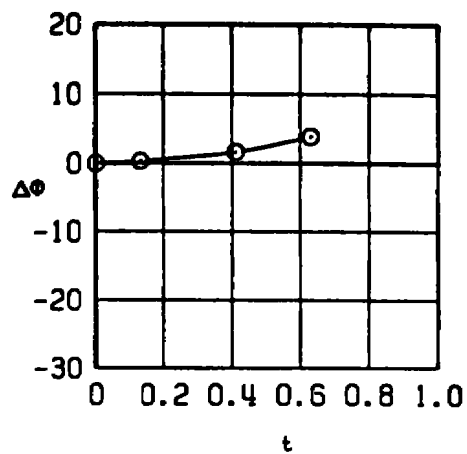
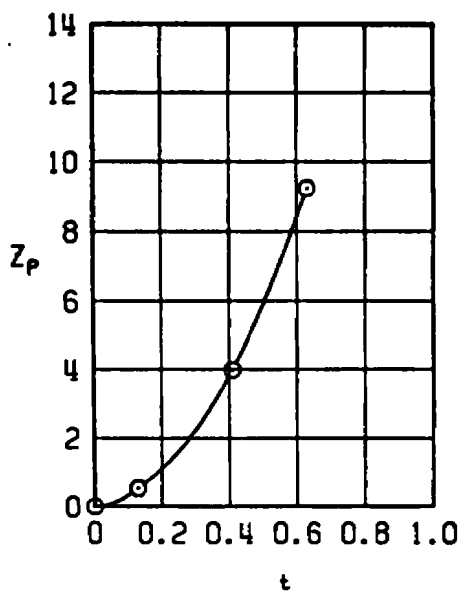
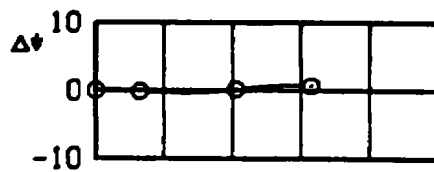
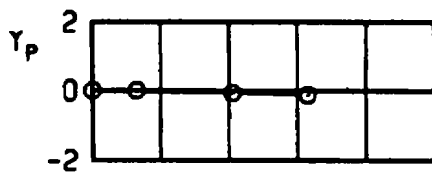
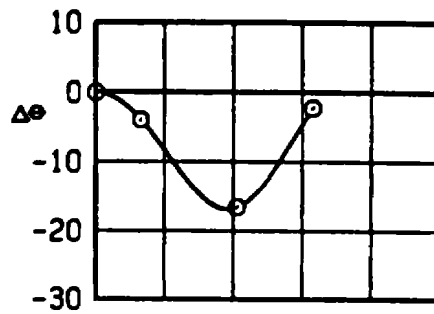
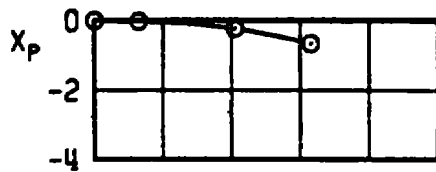
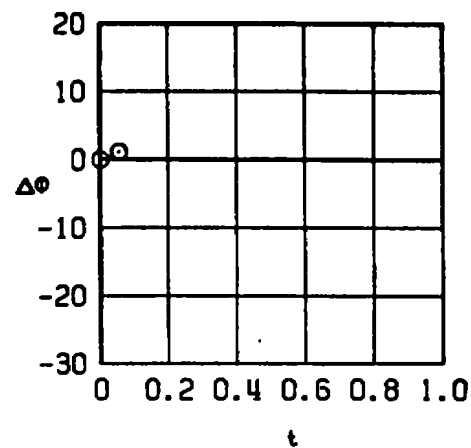
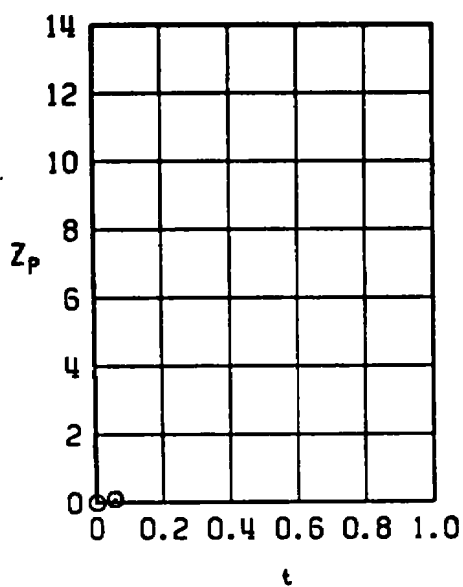
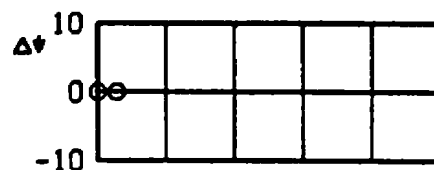
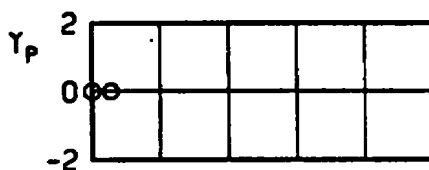
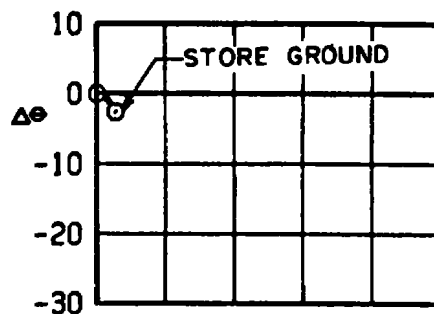
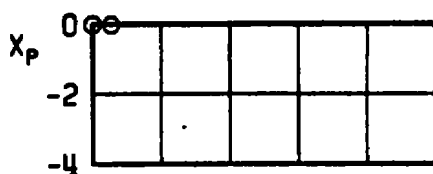
a. $M_\infty = 0.5$

Figure 36. Trajectory data for the modified M-117 bomb configuration.

SYM	M_∞	α	CONFIG
⊙	0.80	0	6



b. $M_\infty = 0.8$
Figure 36. Concluded.

SYM	M_∞	α	CONFIG
⊙	0.50	0	8

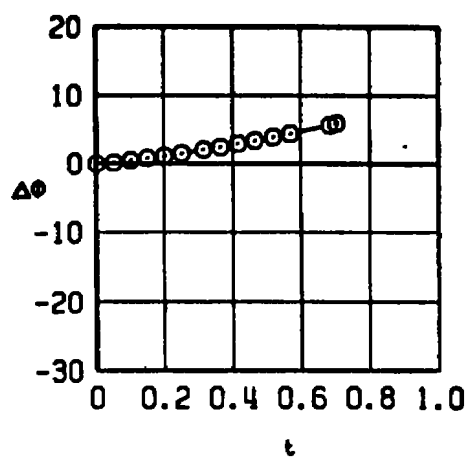
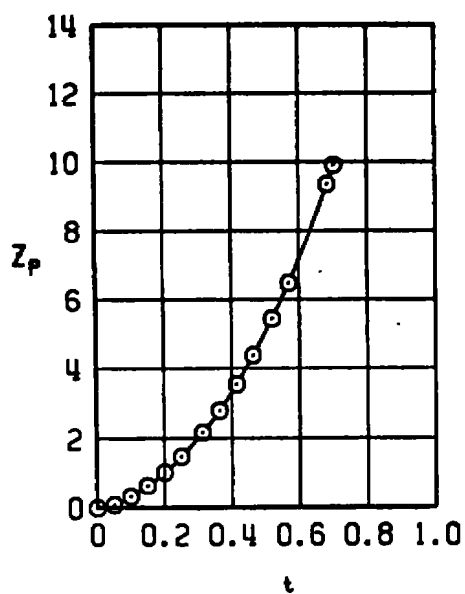
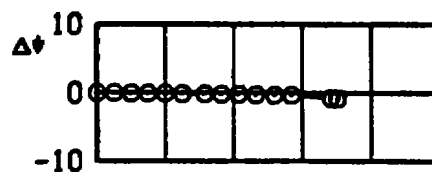
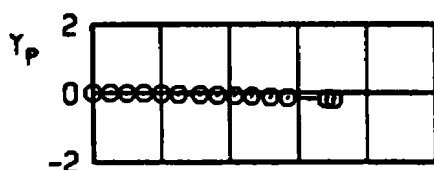
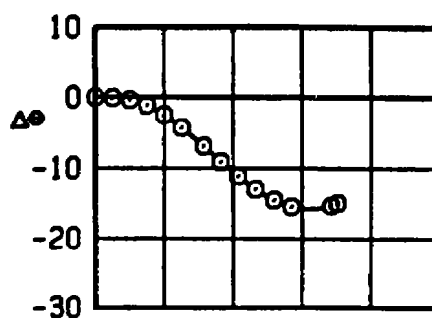
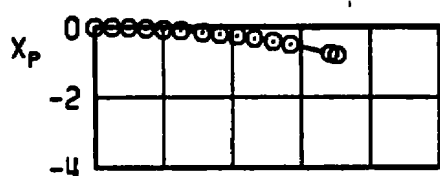
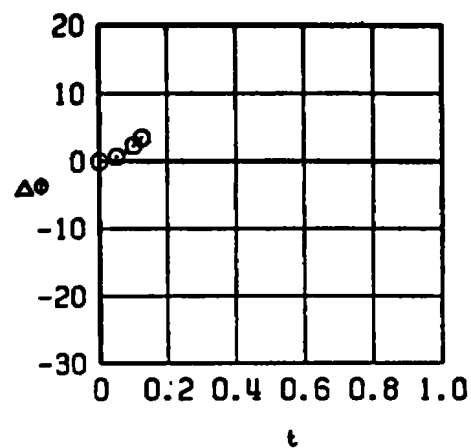
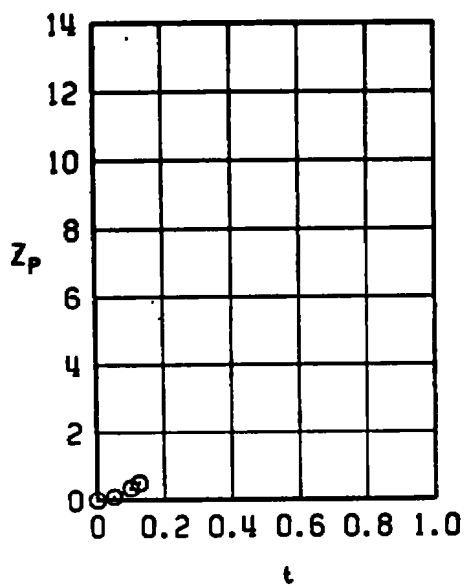
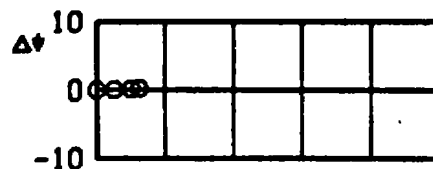
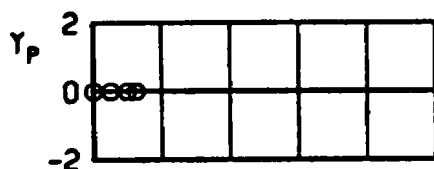
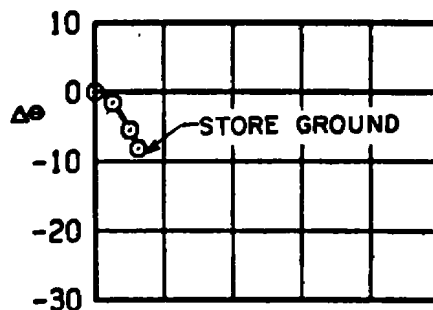
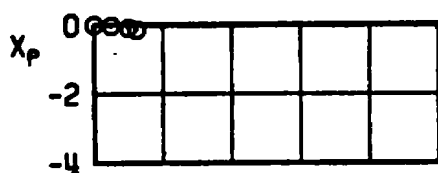
a. $M_\infty = 0.5$

Figure 37. Trajectory data for the 16-in.-diam maximum volume bomb.

SYM	M_∞	α	CONFIG
○	0.80	0	8



b. $M_\infty = 0.8$
Figure 37. Concluded.

SYM	M_∞	α	CONFIG
○	0.50	0	10

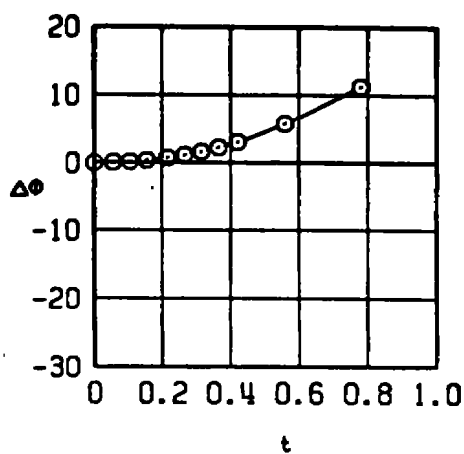
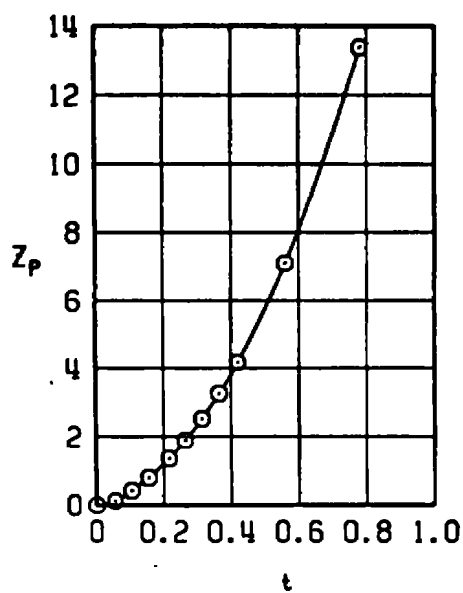
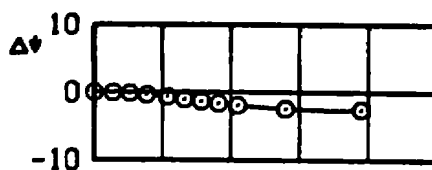
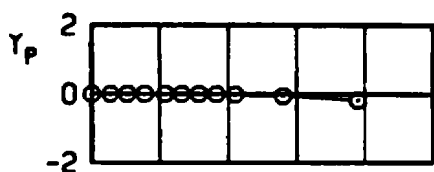
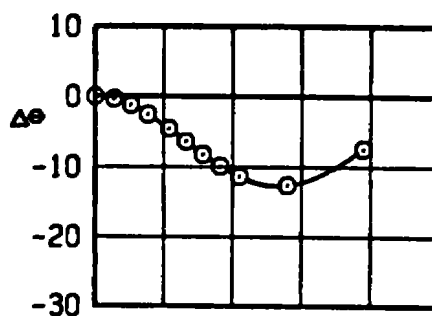
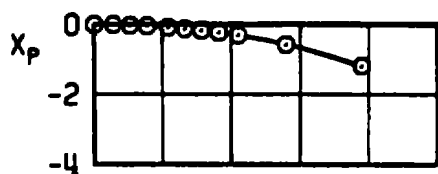
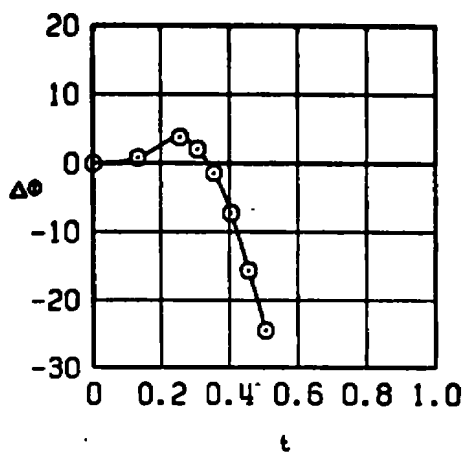
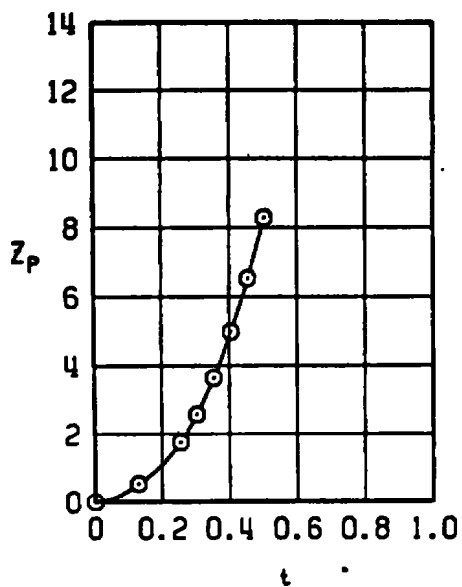
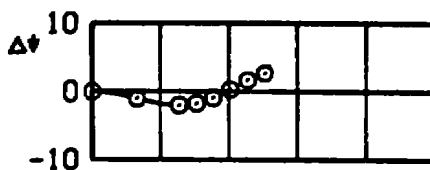
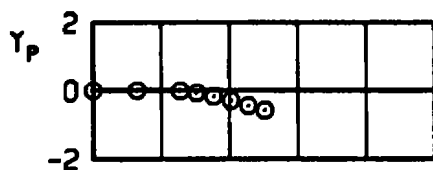
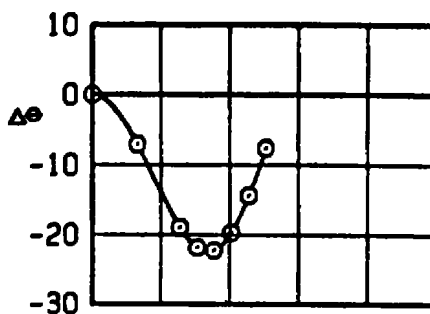
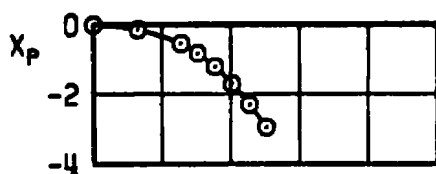
a. $M_\infty = 0.5$

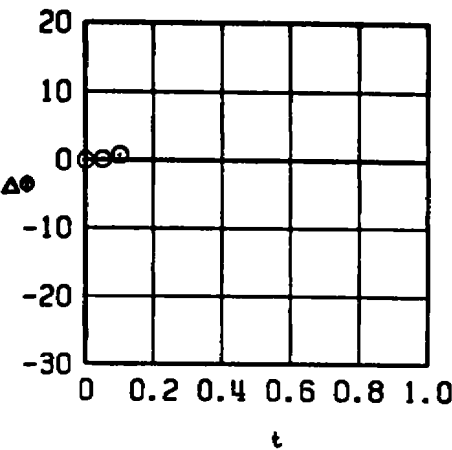
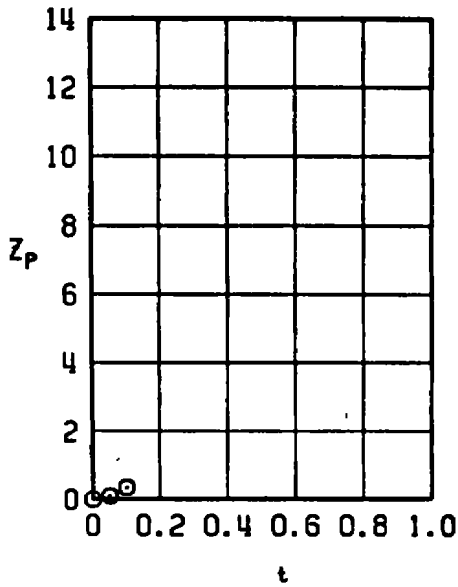
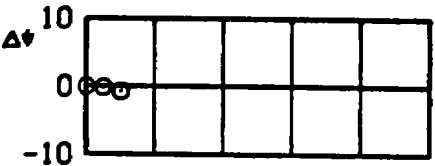
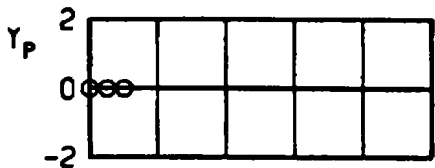
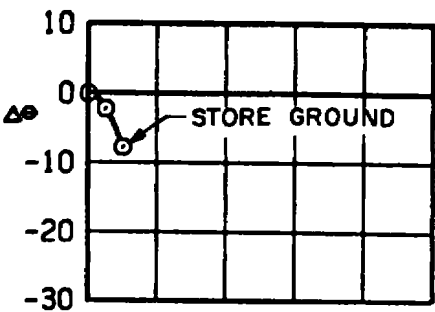
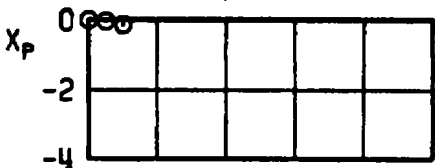
Figure 38. Trajectory data for the 14-in.-diam maximum volume bomb.

SYM	M_∞	α	CONFIG
○	0.80	0	10



b. $M_\infty = 0.8$
Figure 38. Continued.

SYM	M_∞	α	CONFIG
⊙	0.90	0	10



c. $M_\infty = 0.9$
Figure 38. Concluded.

SYM	M_∞	α	CONFIG
⊙	0.50	0	12

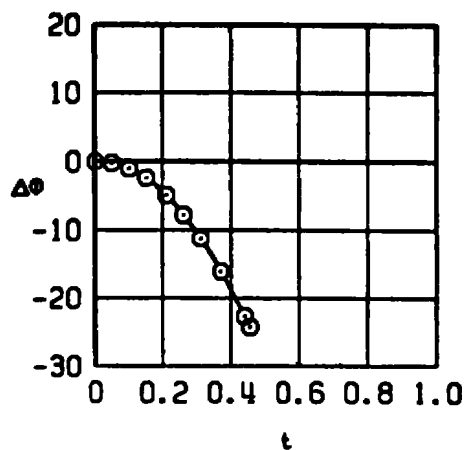
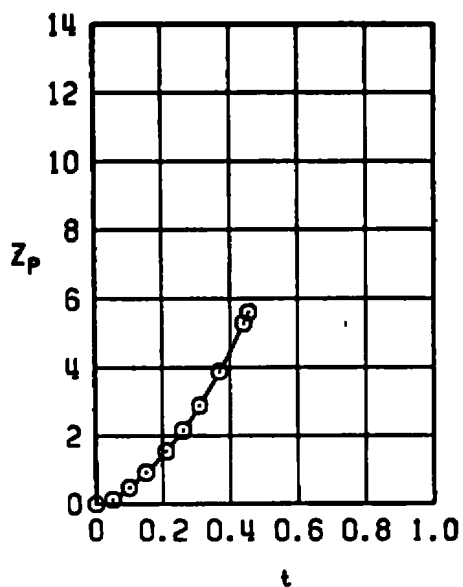
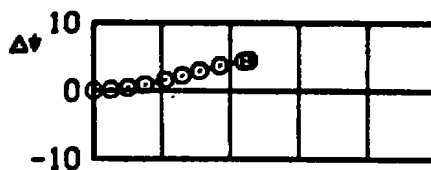
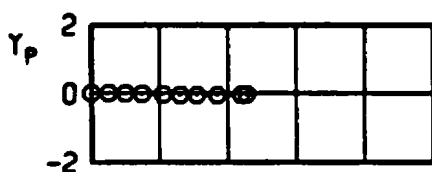
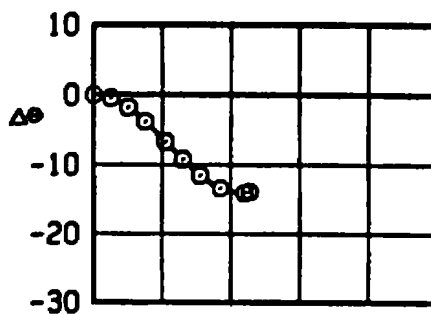
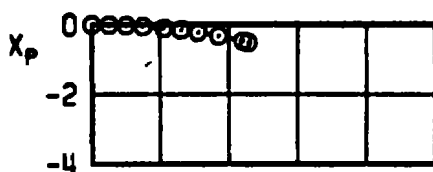
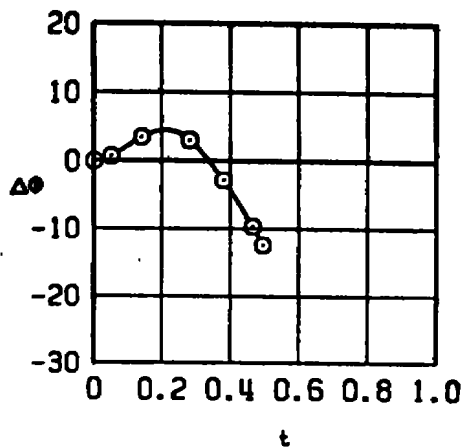
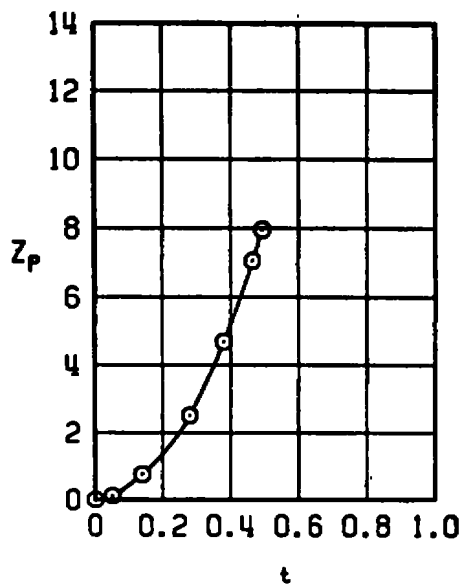
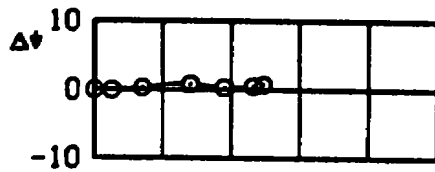
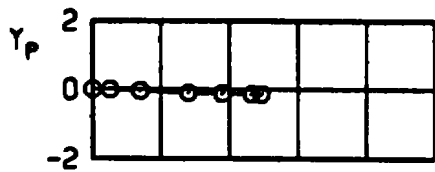
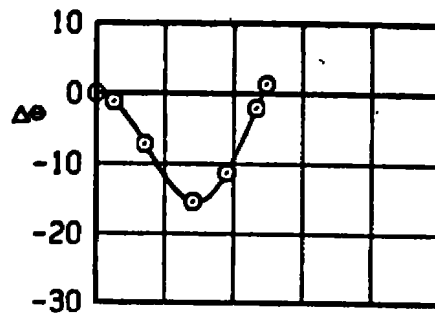
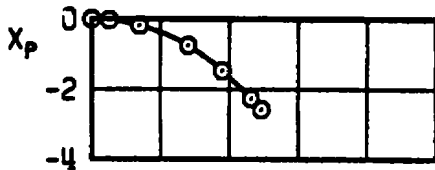
a. $M_\infty = 0.5$

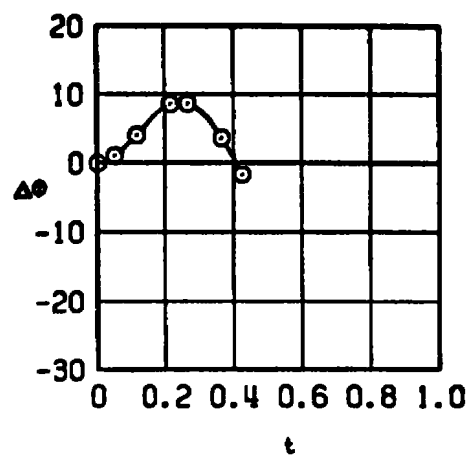
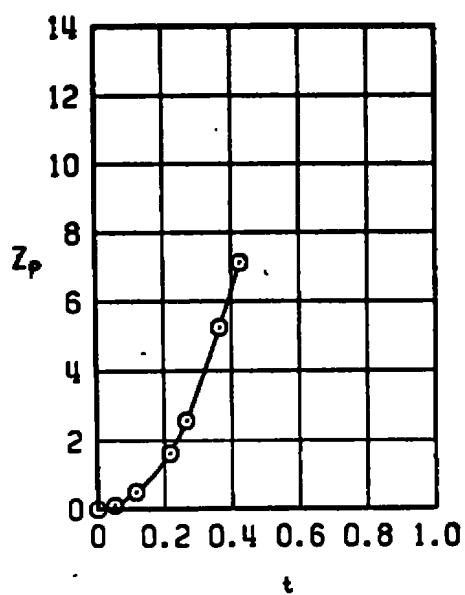
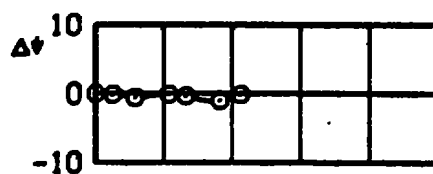
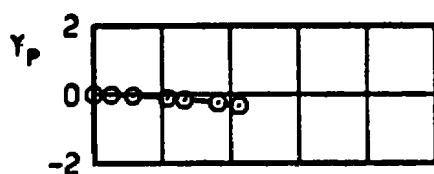
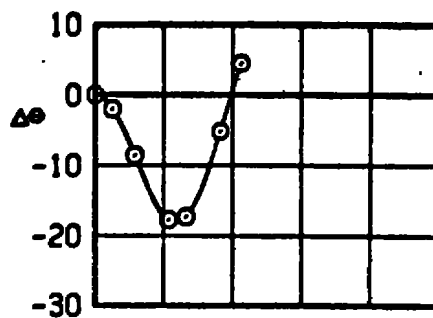
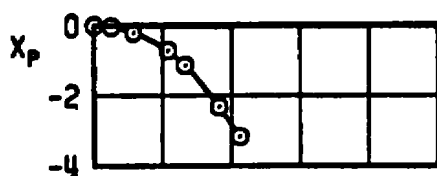
Figure 39. Trajectory Data for the 12-in.-diam maximum volume bomb.

SYM	M_∞	α	CONFIG
⊙	0.80	0	12



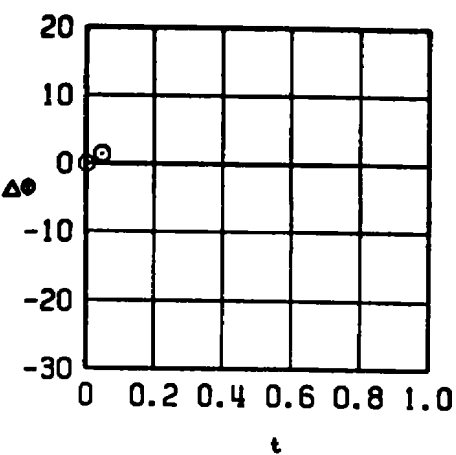
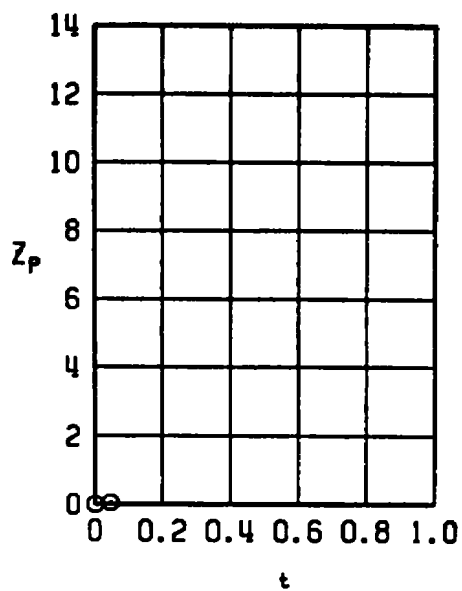
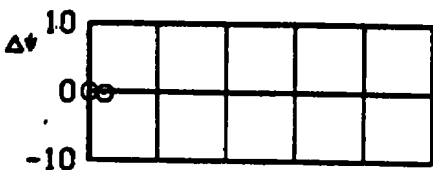
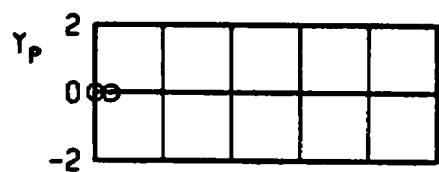
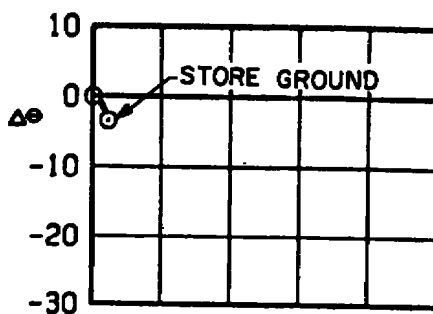
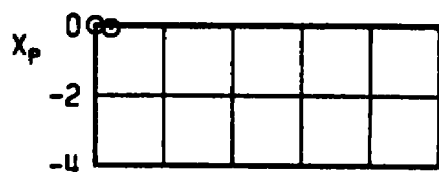
b. $M_\infty = 0.8$
Figure 39. Continued.

SYM	M_∞	α	CONFIG
⊙	0.90	0	12



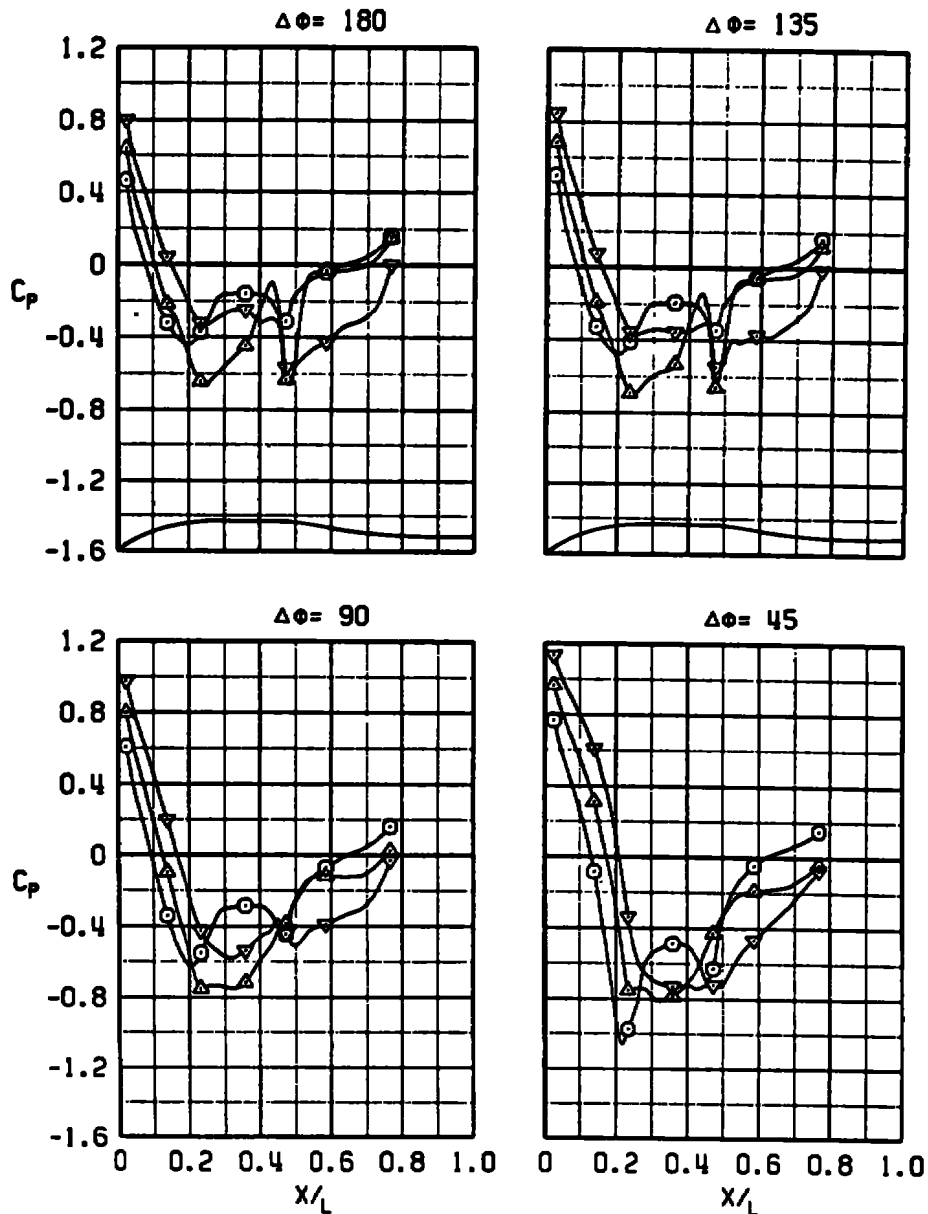
c. $M_\infty = 0.9$
Figure 39. Continued.

SYM	M_∞	α	CONFIG
⊙	1.10	0	12



d. $M_\infty = 1.1$
Figure 39. Concluded.

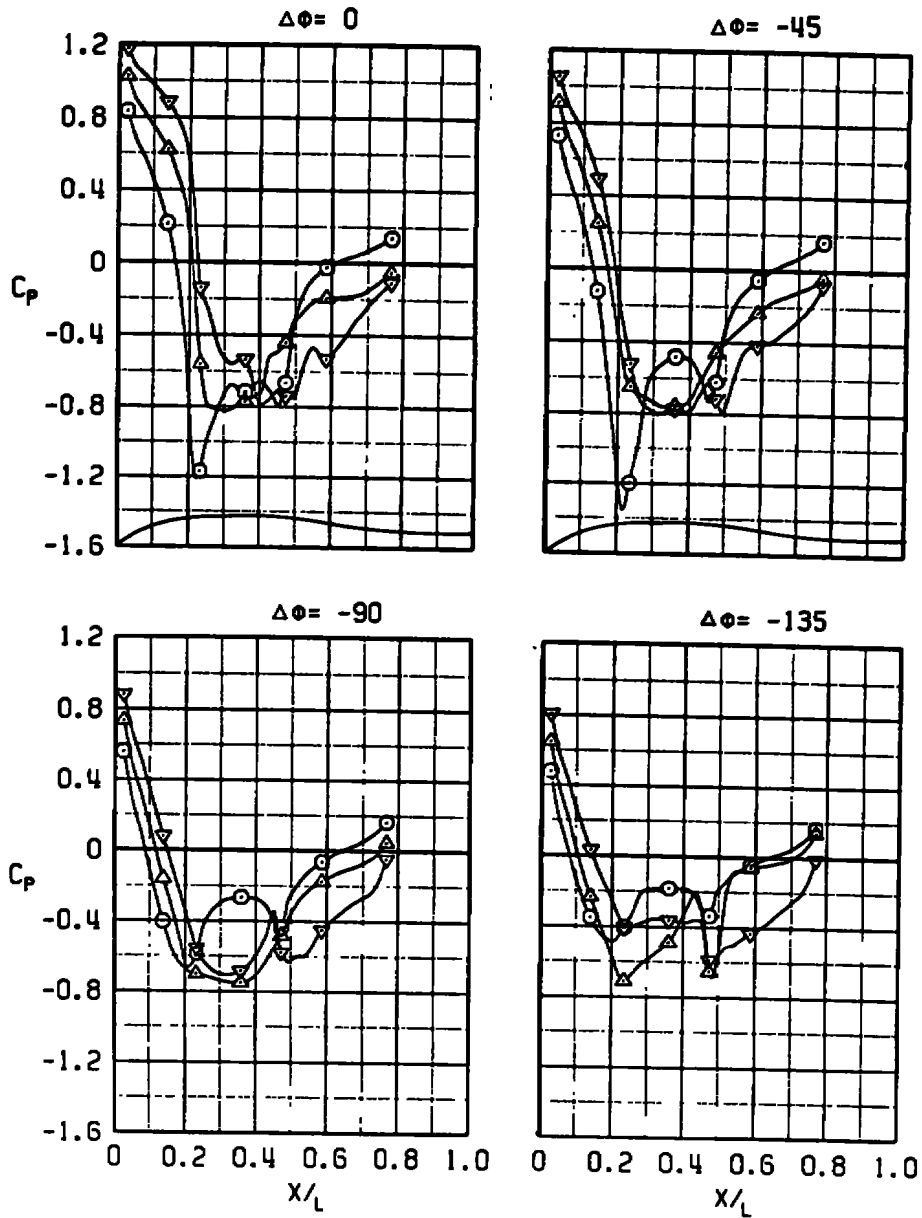
SYM	M_∞	α	$Re \times 10^{-6}$	CONF	FUSE	Z/D	$\Delta\theta$
○	0.5	0	3.02	4	NONE	0	0
△	0.9	0	2.37	4	NONE	0	0
▽	1.1	0	2.49	4	NONE	0	0



a. Positive roll

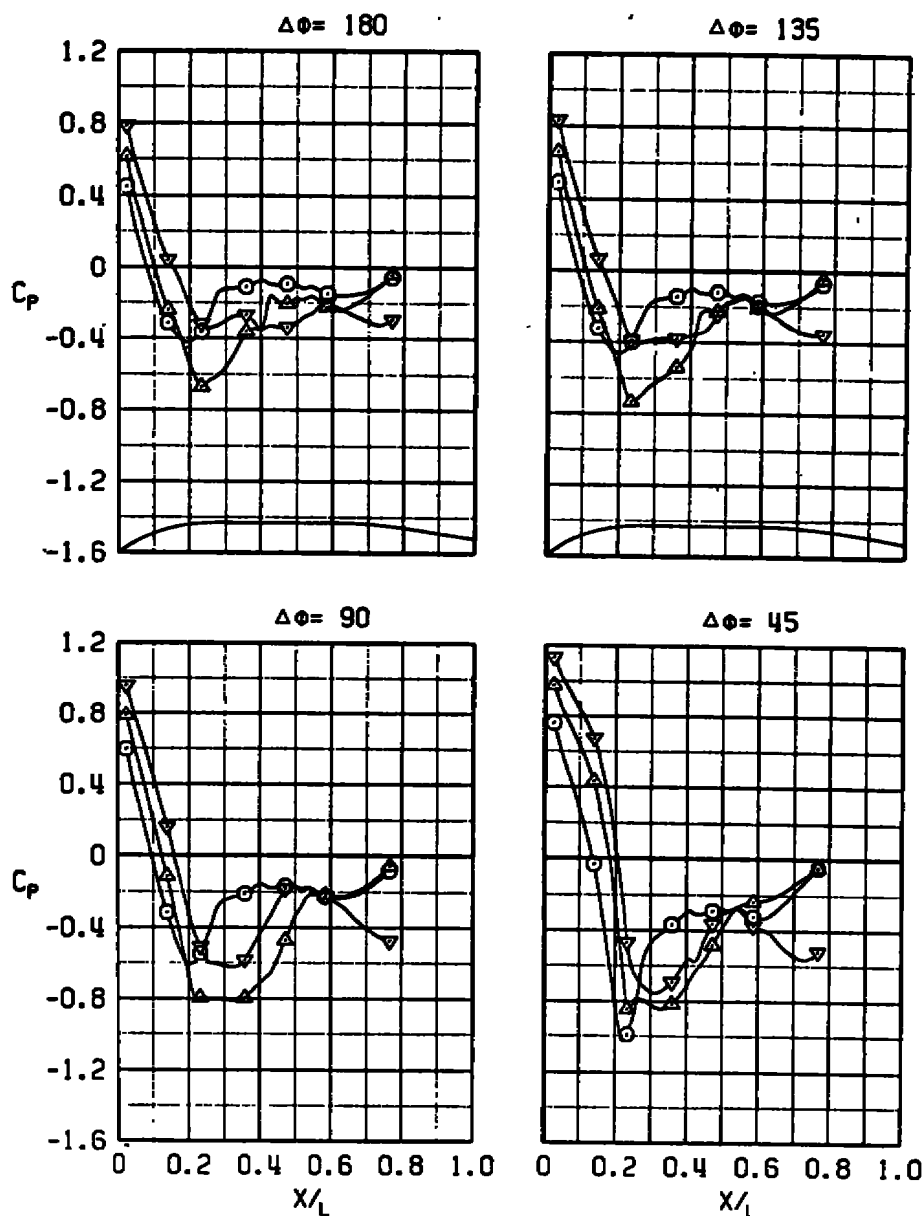
Figure 40. Pressure distribution data on the standard M-117 bomb configuration at the number one carriage position of the wing-pylon-TER configuration.

SYM	M_∞	α	$Re \times 10^{-6}$	CONF	FUSE	Z/D	$\Delta\theta$
○	0.5	0	3.02	4	NONE	0	0
△	0.9	0	2.37	4	NONE	0	0
▽	1.1	0	2.49	4	NONE	0	0



b. Negative roll
Figure 40. Concluded.

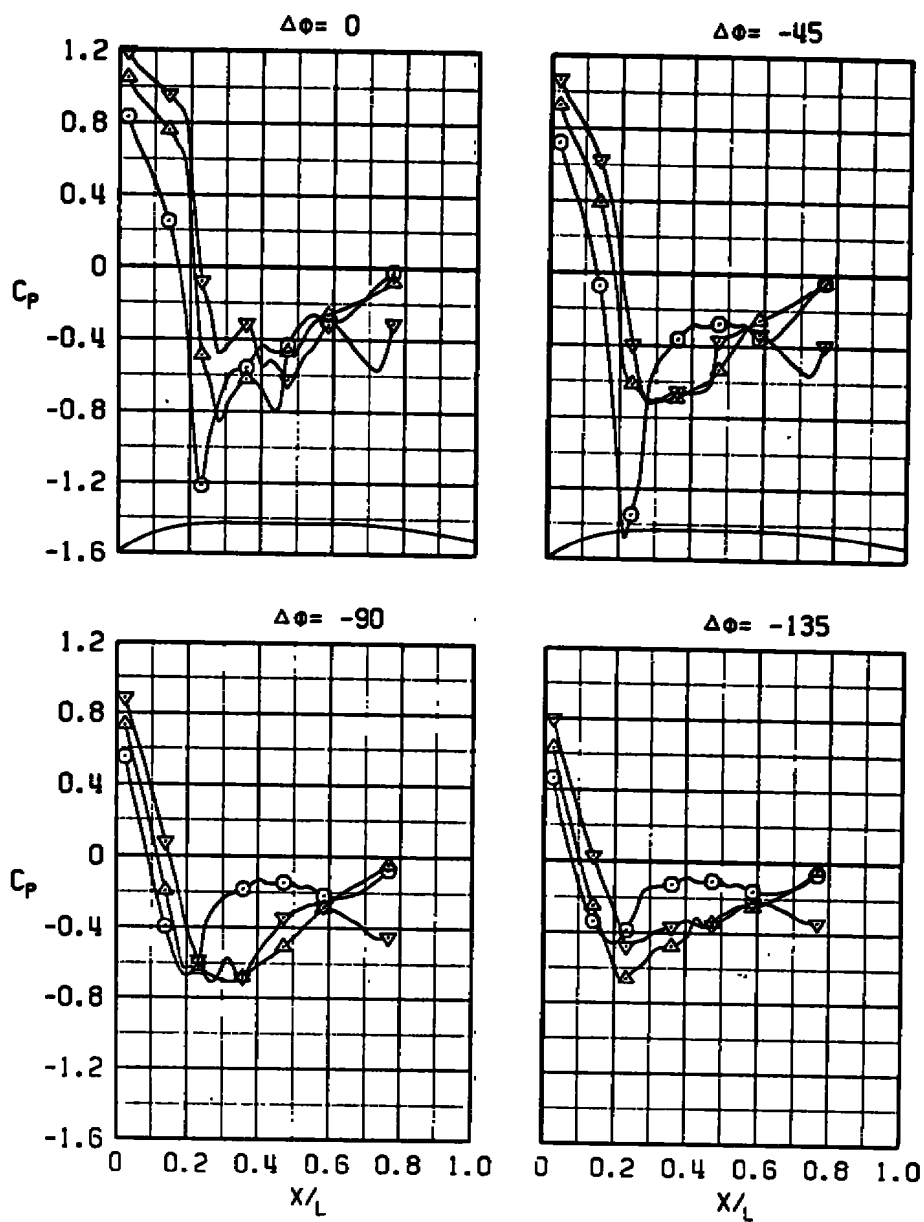
SYM	M _∞	α	ReX10 ⁻⁶	CONF	FUSE	Z/D	Δθ
○	0.5	0	3.18	6	NONE	0	0
△	0.9	0	2.55	6	NONE	0	0
▽	1.1	0	2.65	6	NONE	0	0



a. Positive roll

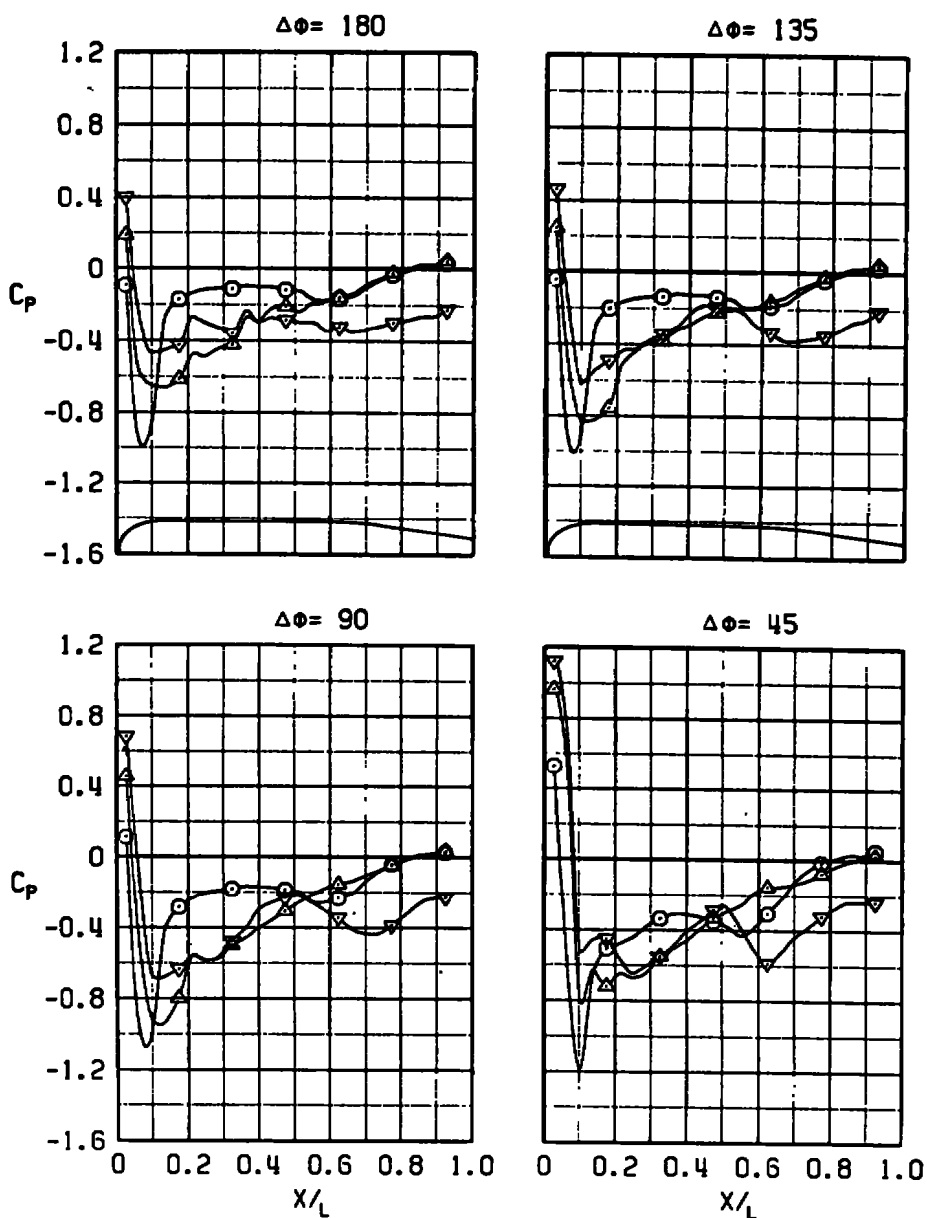
Figure 41. Pressure distribution data on the modified M-117 bomb configuration at the number one carriage position of the wing-pylon-TER configuration.

SYM	M_∞	α	$Re \times 10^{-6}$	CONF	FUSE	Z/D	$\Delta\theta$
○	0.5	0	3.18	6	NONE	0	0
△	0.9	0	2.55	6	NONE	0	0
▽	1.1	0	2.65	6	NONE	0	0



b. Negative roll
Figure 41. Concluded.

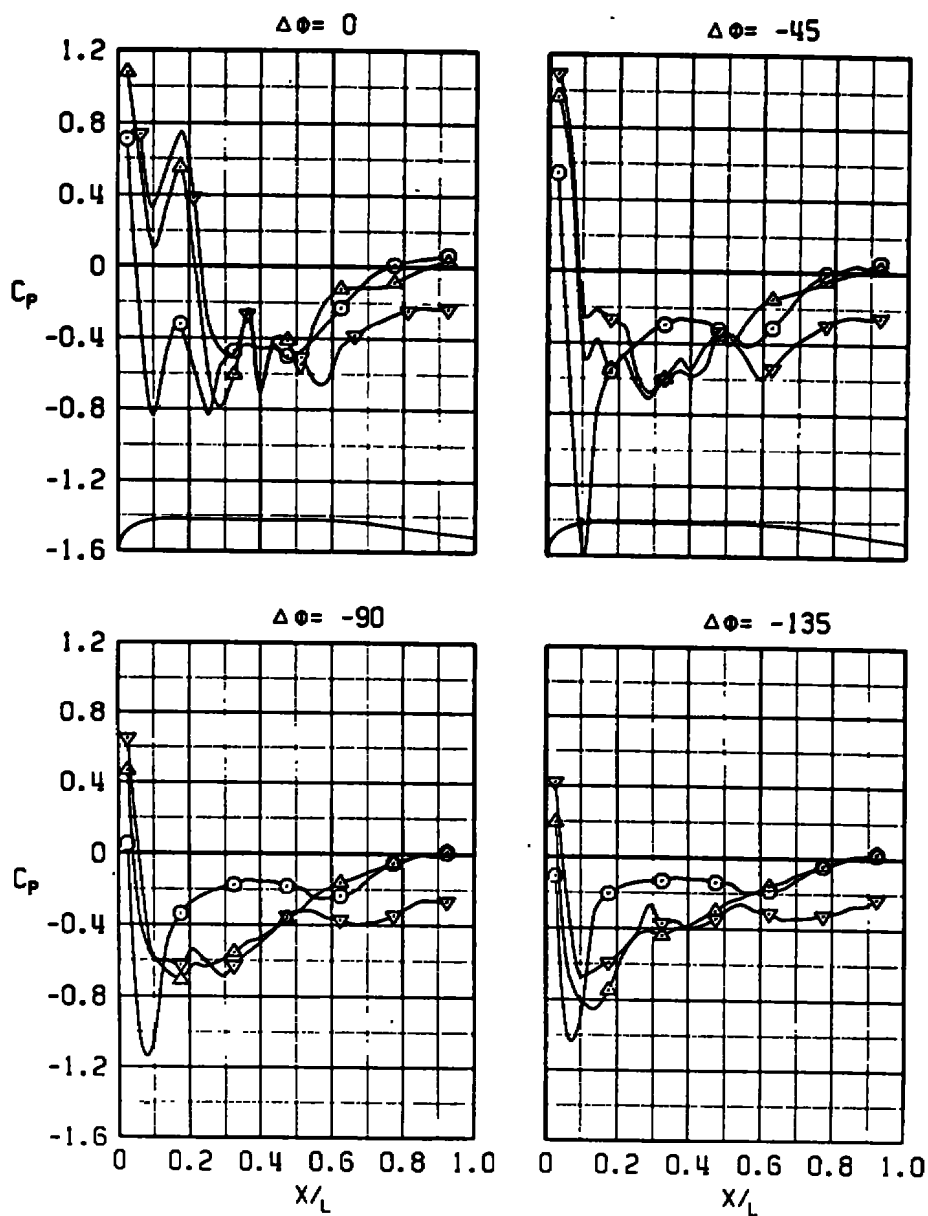
SYM	M_∞	α	$Re \times 10^{-6}$	CONF	FUSE	Z/D	$\Delta\theta$
○	0.5	0	2.98	8	NONE	0	0
△	0.9	0	2.00	8	NONE	0	0
▽	1.1	0	2.22	8	NONE	0	0



a. Positive roll

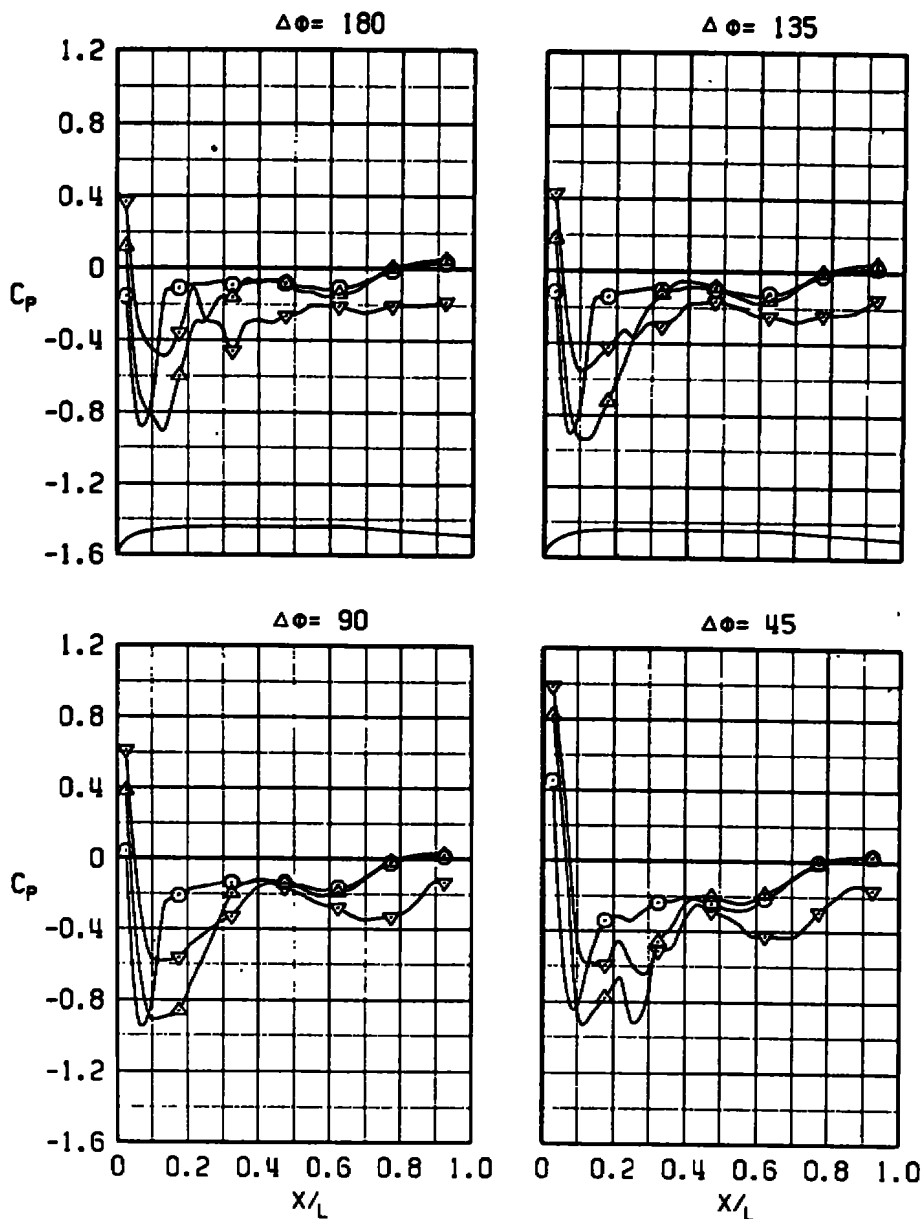
Figure 42. Pressure distribution data on the 16-in.-diam maximum volume bomb at the number one carriage position of the wing-pylon-TER configuration.

SYM	M_∞	α	$Re \times 10^{-6}$	CONF	FUSE	Z/D	$\Delta\theta$
○	0.5	0	2.98	8	NONE	0	0
△	0.9	0	2.00	8	NONE	0	0
▽	1.1	0	2.22	8	NONE	0	0



b. Negative roll
Figure 42. Concluded.

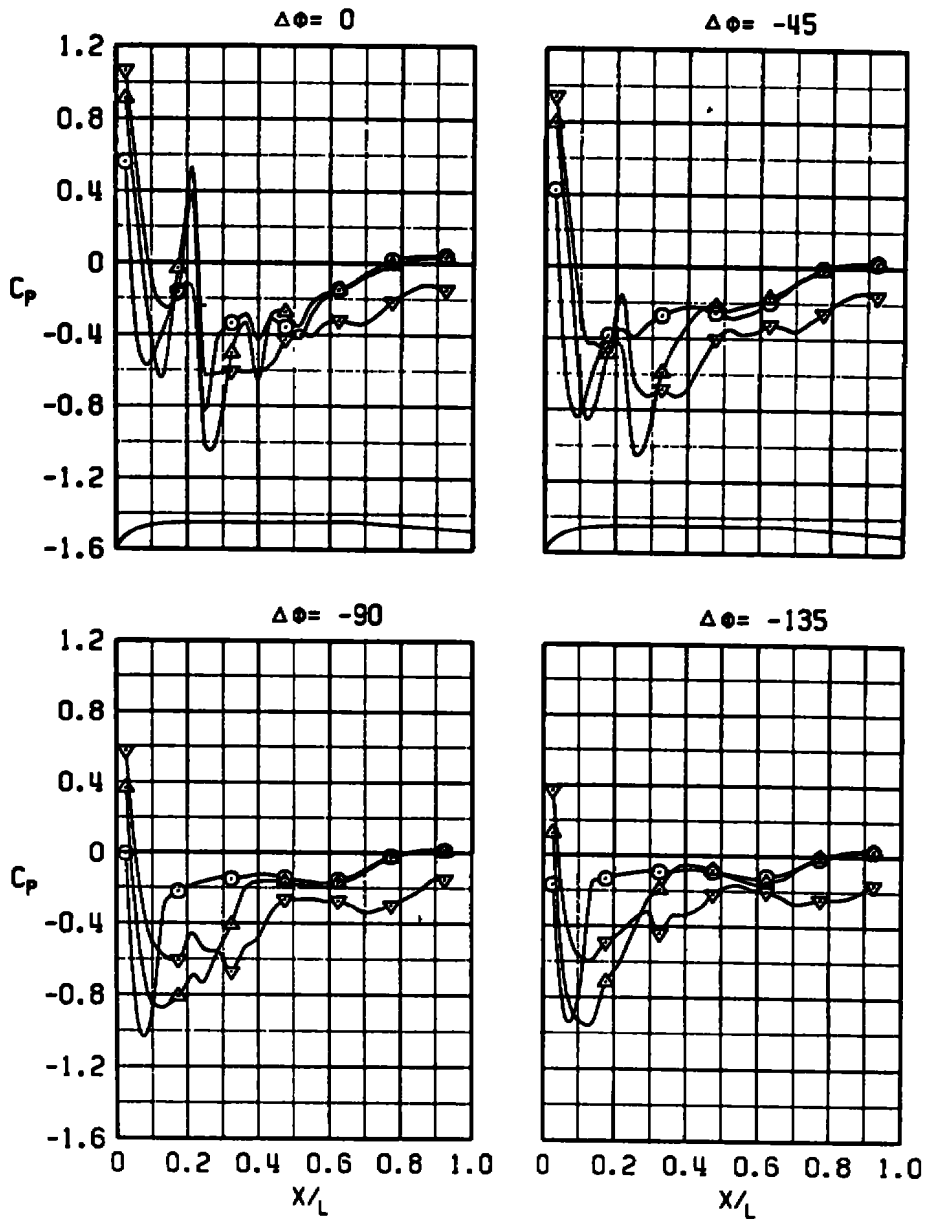
SYM	M_∞	α	$Re \times 10^{-6}$	CONF	FUSE	Z/D	$\Delta\theta$
○	0.5	0	1.37	10	NONE	0	0
△	0.9	0	1.98	10	NONE	0	0
▽	1.1	0	2.21	10	NONE	0	0



a. Positive roll

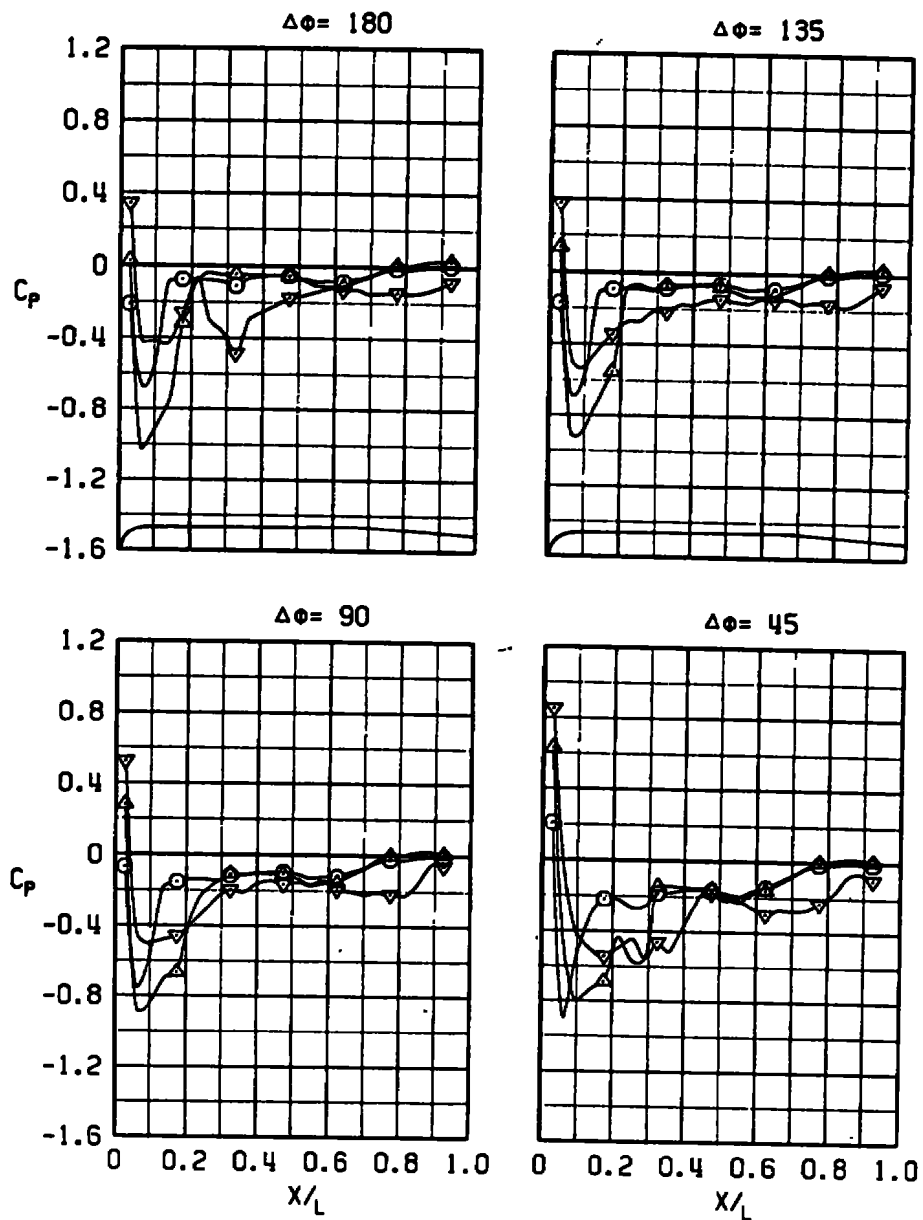
Figure 43. Pressure distribution data on the 14-in.-diam maximum volume bomb at the number one carriage position of the wing-pylon-TER configuration.

SYM	M_∞	α	$Re \times 10^{-6}$	CONF	FUSE	Z/D	$\Delta\theta$
○	0.5	0	1.37	10	NONE	0	0
△	0.9	0	1.98	10	NONE	0	0
▽	1.1	0	2.21	10	NONE	0	0



b. Negative roll
Figure 43. Concluded.

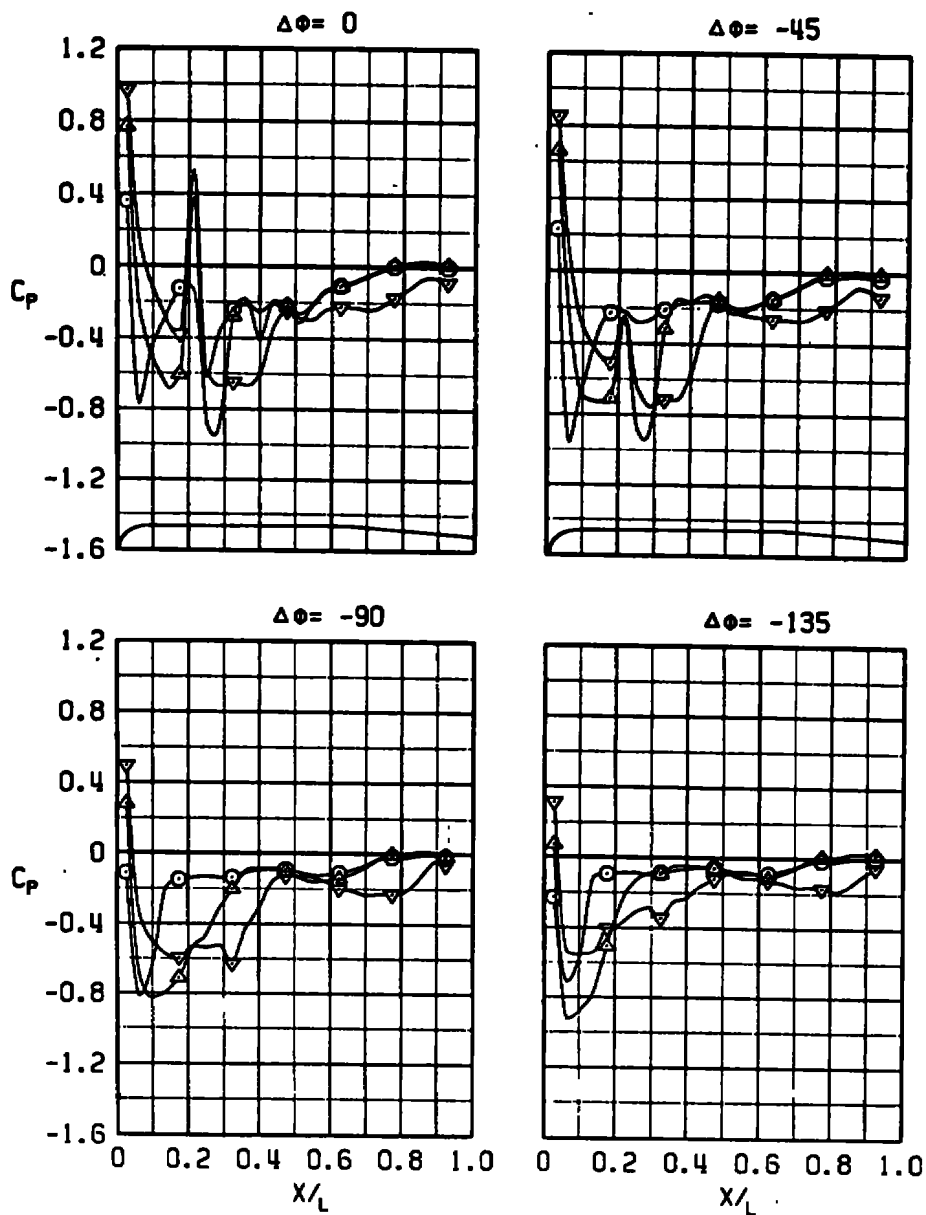
SYM	M _L	α	ReX10 ⁻⁶	CONF	FUSE	Z/D	$\Delta\theta$
○	0.5	-1	1.55	12	NONE	0	0
△	0.9	0	1.99	12	NONE	0	0
▽	1.1	0	2.23	12	NONE	0	0



a. Positive roll

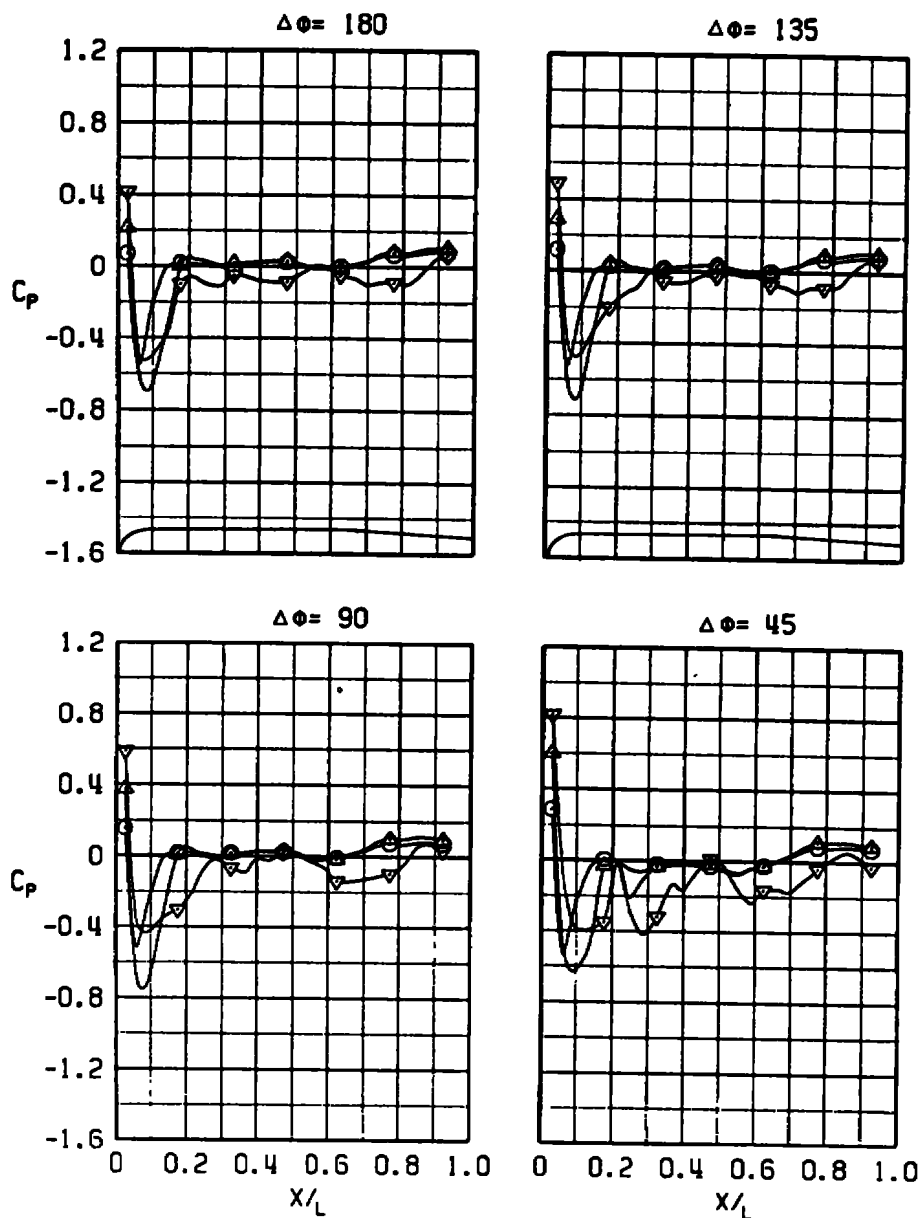
Figure 44. Pressure distribution data on the 12-in.-diam maximum volume bomb at the number one carriage position of the wing-pylon-TER configuration.

SYM	M_∞	α	$Re \times 10^{-6}$	CONF	FUSE	Z/D	$\Delta\theta$
○	0.5	-1	1.55	12	NONE	0	0
△	0.9	0	1.99	12	NONE	0	0
▽	1.1	0	2.23	12	NONE	0	0



b. Negative roll
Figure 44. Concluded.

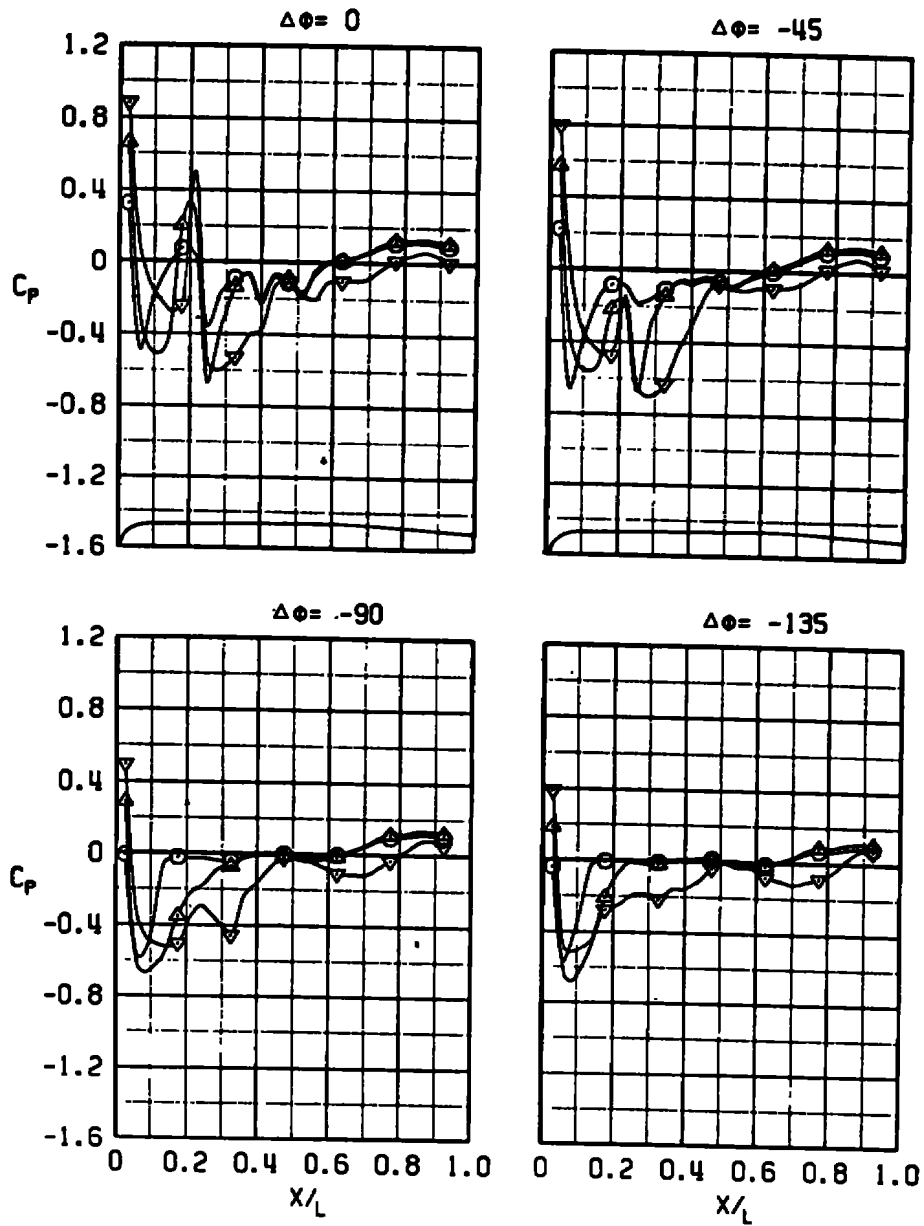
SYM	M_∞	α	$Re \times 10^{-6}$	CONF	FUSE	Z/D	$\Delta\theta$
○	0.5	5	1.55	12	NONE	0	0
△	0.9	5	1.98	12	NONE	0	0
▽	1.1	5	2.30	12	NONE	0	0



a. Positive roll

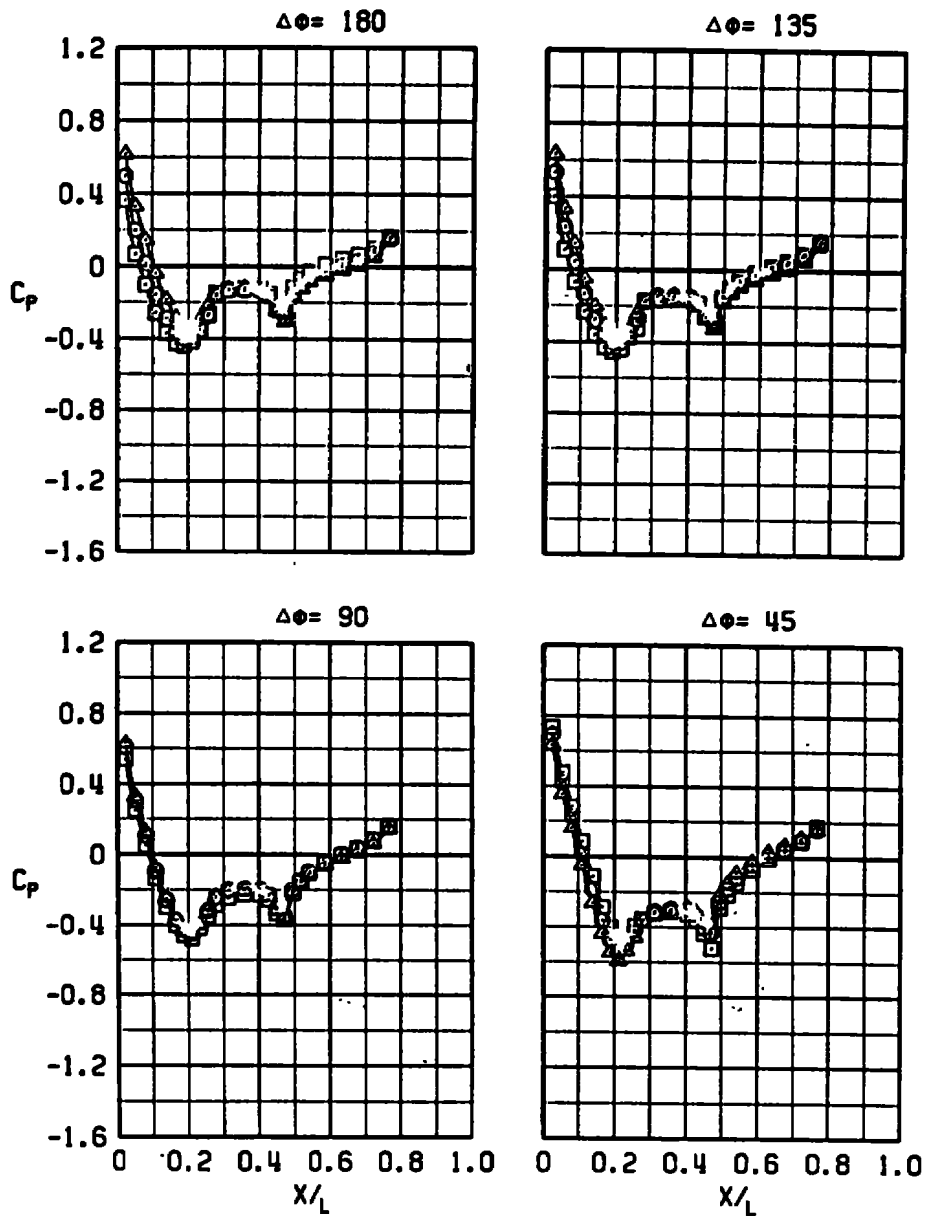
Figure 45. Pressure distribution data on the 12-in.-diam maximum volume bomb at the number one carriage position of the wing-pylon-TER configuration, $\alpha = 5$ deg.

SYM	M_∞	α	$Re \times 10^{-6}$	CONF	FUSE	Z/O	$\Delta\theta$
○	0.5	5	1.55	12	NONE	0	0
△	0.9	5	1.98	12	NONE	0	0
▽	1.1	5	2.30	12	NONE	0	0



b. Negative roll
Figure 45. Concluded.

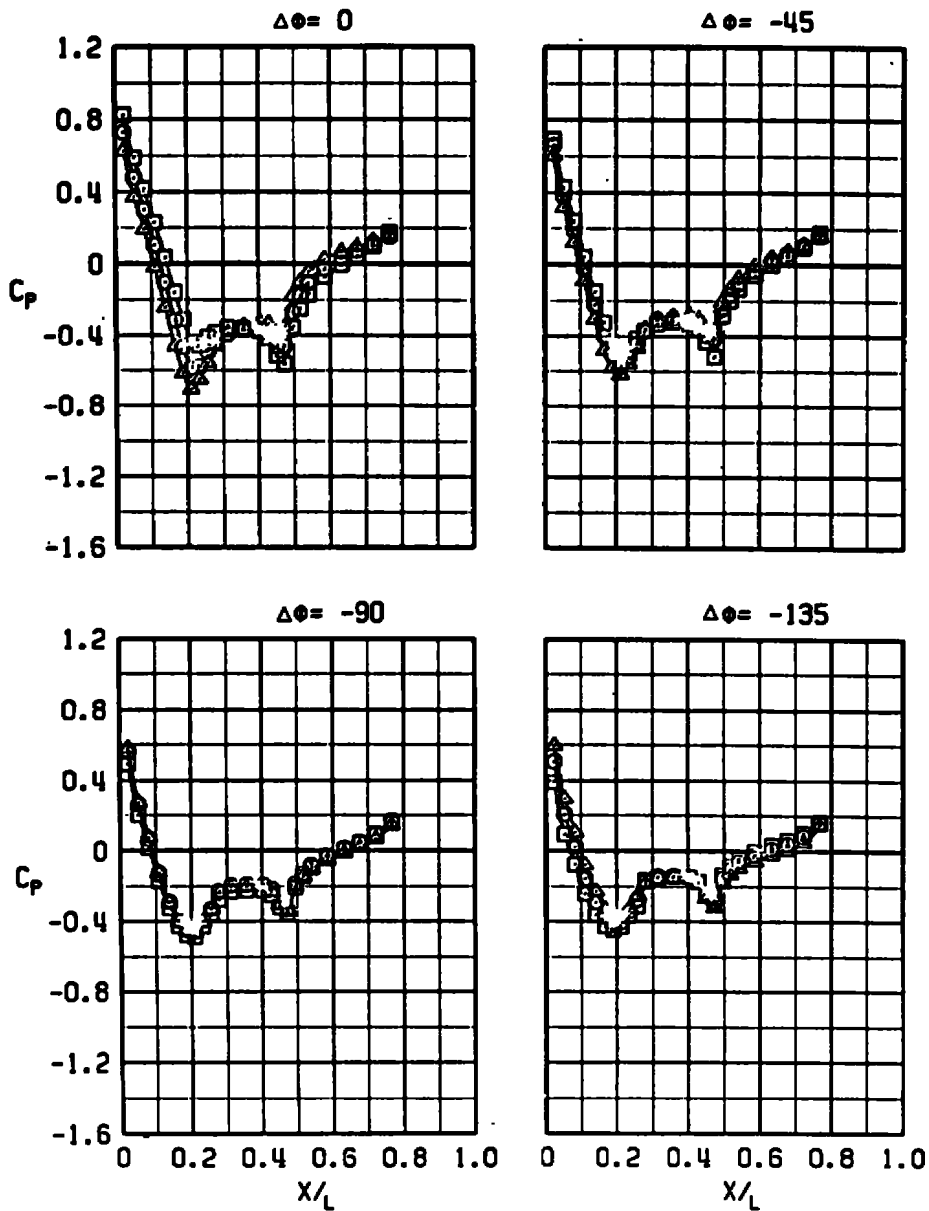
SYM	M_∞	α	$Re \times 10^{-6}$	CONF	FUSE	Z/D	$\Delta\theta$
○	0.5	0	3.02	4	NONE	0.5	0
□	0.5	0	3.02	4	NONE	0.5	-5
△	0.5	0	3.02	4	NONE	0.5	5



a. Positive roll

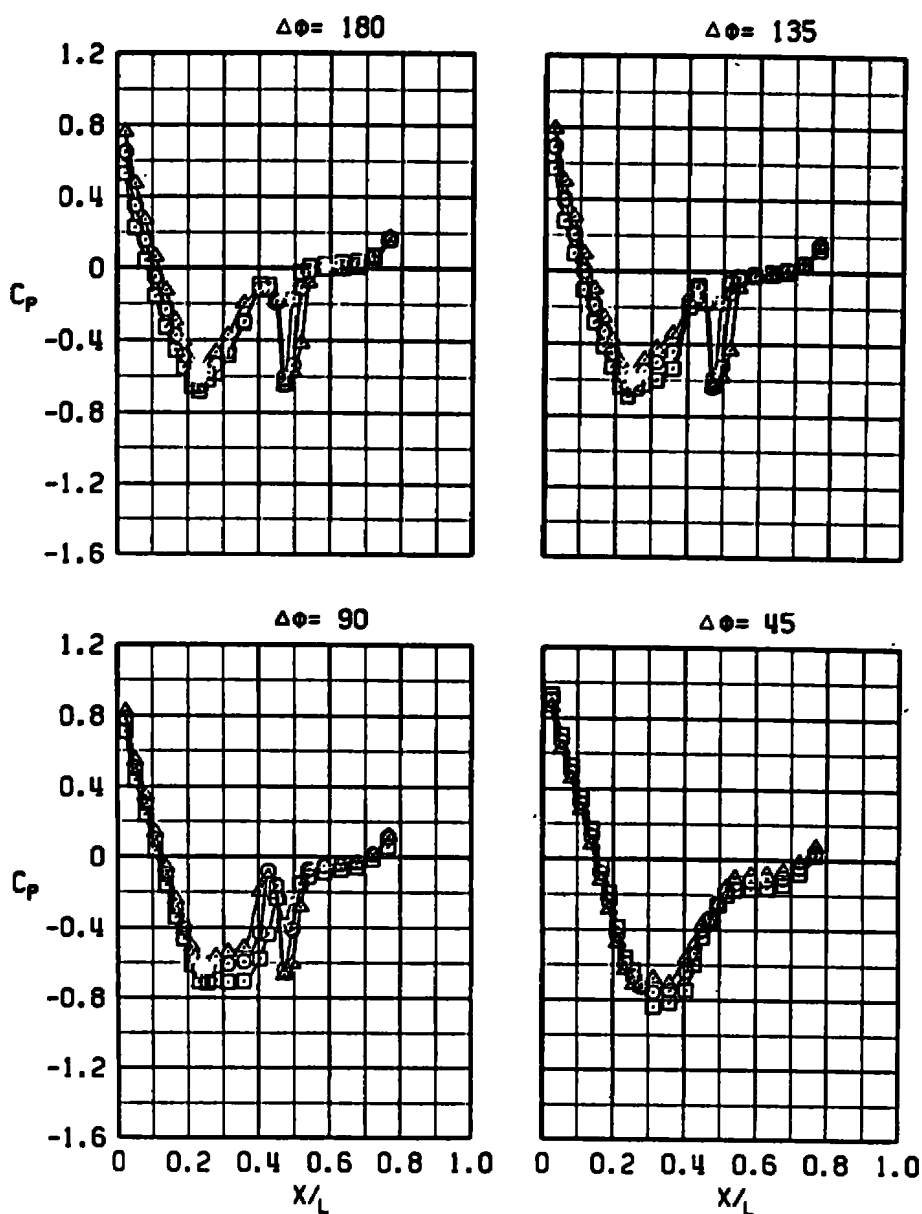
Figure 46. Effects of store pitch incidence angle for the standard M-117 bomb configuration, $M_\infty = 0.5$.

SYM	M_∞	α	$Re \times 10^{-6}$	CONF	FUSE	Z/D	$\Delta\theta$
○	0.5	0	3.02	4	NONE	0.5	0
□	0.5	0	3.02	4	NONE	0.5	-5
△	0.5	0	3.02	4	NONE	0.5	5



b. Negative roll
Figure 46. Concluded.

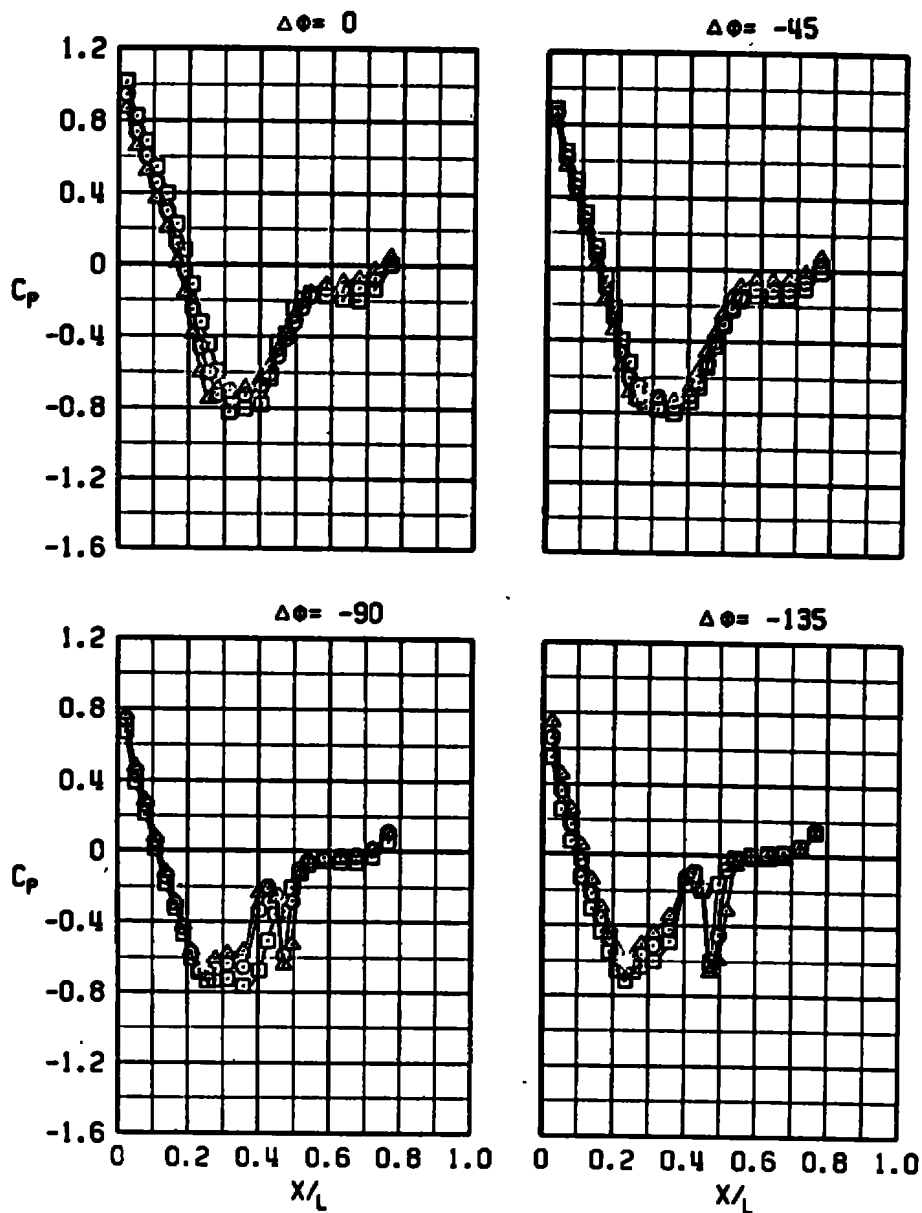
SYM	M_∞	α	$Re \times 10^{-6}$	CONF	FUSE	Z/D	$\Delta\theta$
○	0.9	0	2.37	4	NONE	0.5	0
□	0.9	0	2.37	4	NONE	0.5	-5
△	0.9	0	2.37	4	NONE	0.5	5



a. Positive roll

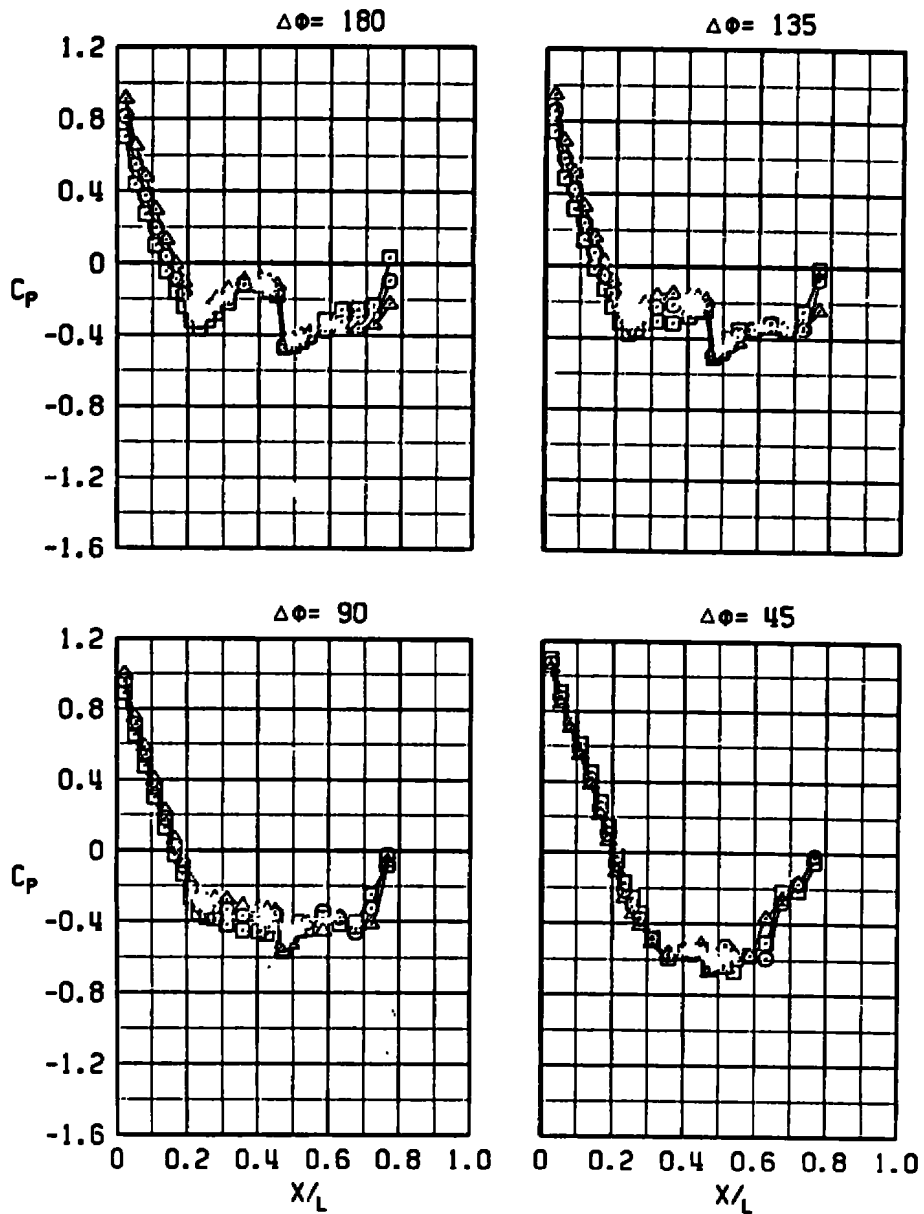
Figure 47. Effects of store pitch incidence angle for the standard M-117 bomb configuration, $M_\infty = 0.9$.

SYM	M_∞	α	$Re \times 10^{-6}$	CONF	FUSE	Z/D	$\Delta\theta$
○	0.9	0	2.37	4	NONE	0.5	0
□	0.9	0	2.37	4	NONE	0.5	-5
△	0.9	0	2.37	4	NONE	0.5	5



b. Negative roll
Figure 47. Concluded.

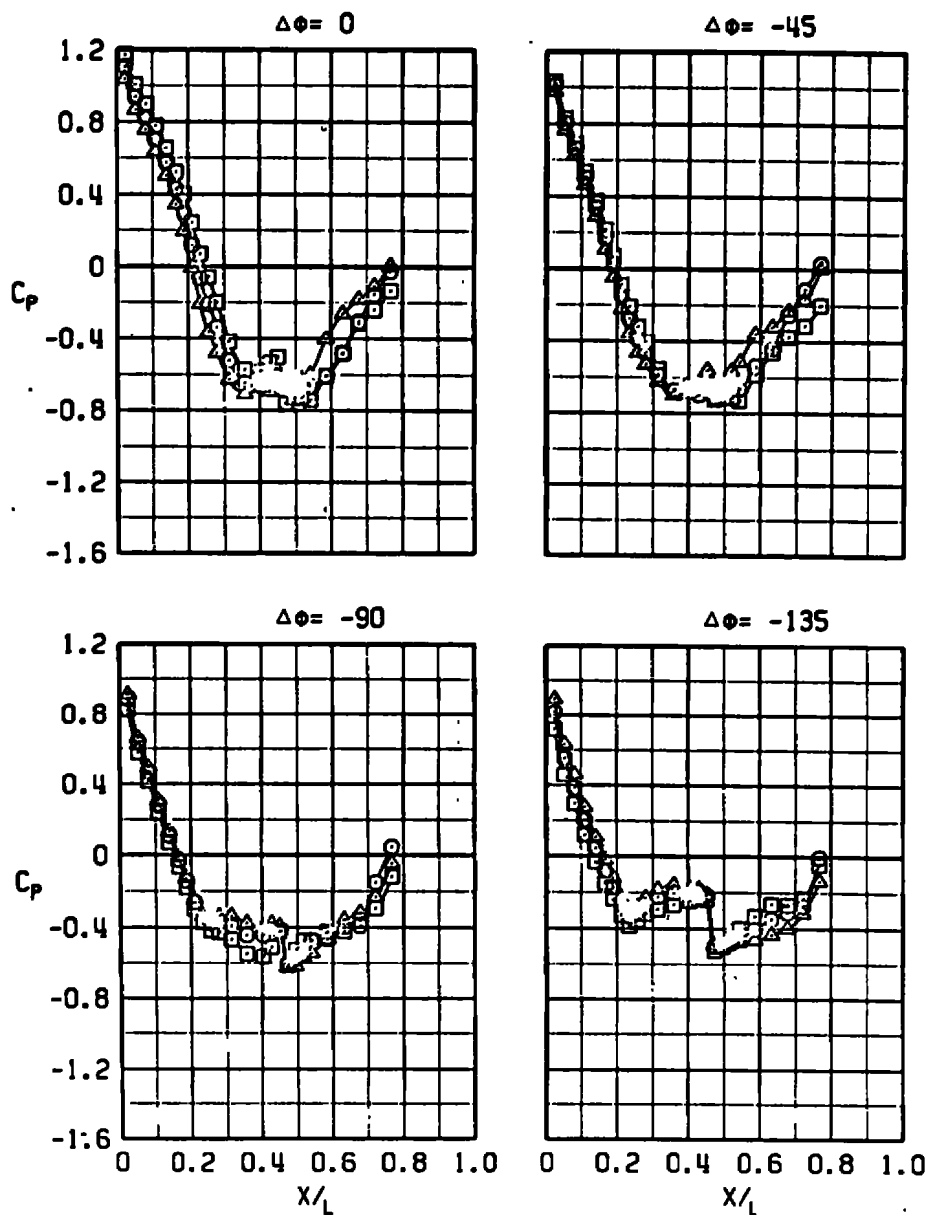
SYM	M_∞	α	$Re \times 10^{-6}$	CONF	FUSE	Z/D	$\Delta\theta$
○	1.1	0	2.49	4	NONE	0.5	0
□	1.1	0	2.49	4	NONE	0.5	-5
△	1.1	0	2.49	4	NONE	0.5	5



a. Positive roll

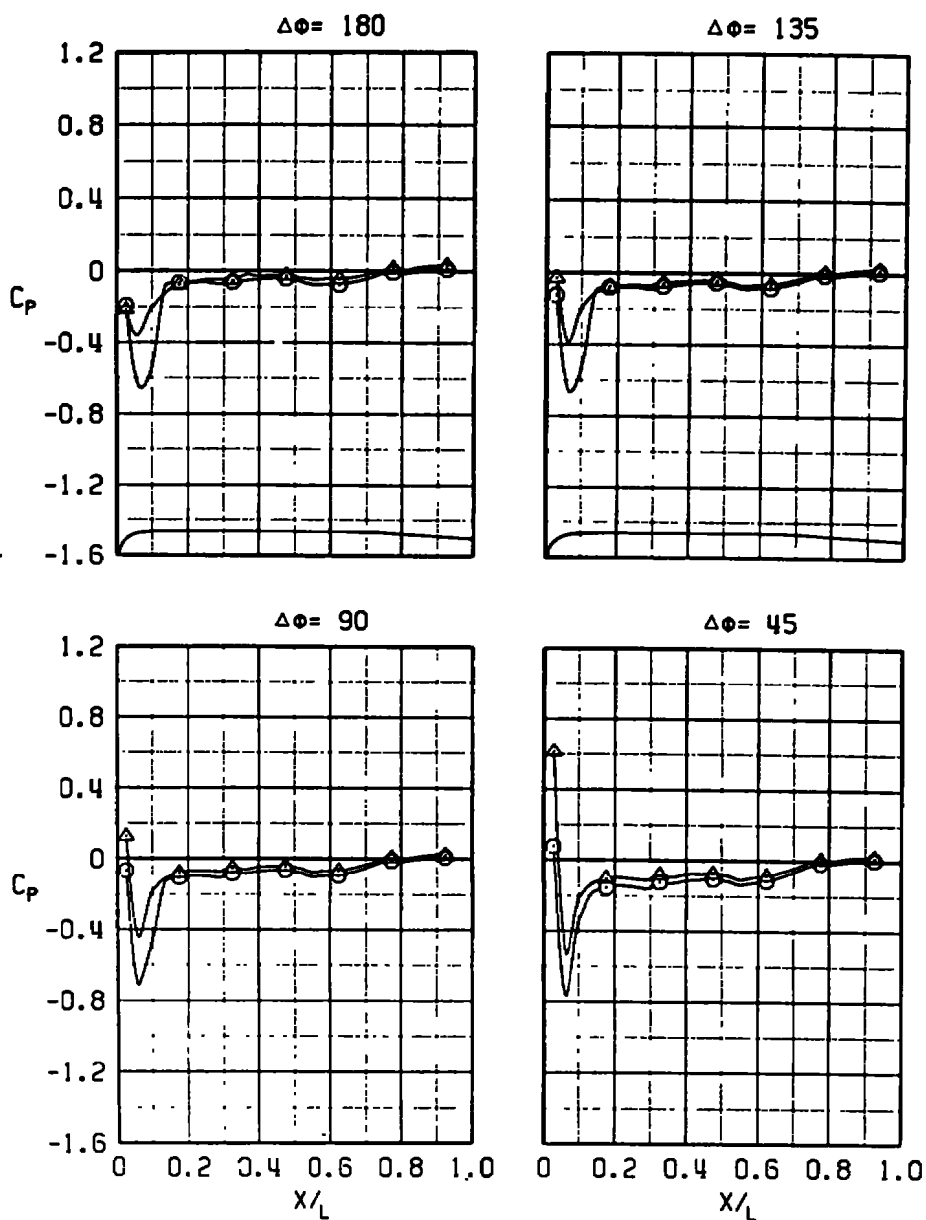
Figure 48. Effects of store pitch incidence angle for the standard M-117 bomb configuration, $M_\infty = 1.1$.

SYM	M_∞	α	$Re \times 10^{-6}$	CONF	FUSE	Z/D	$\Delta\theta$
○	1.1	0	2.49	4	NONE	0.5	0
□	1.1	0	2.49	4	NONE	0.5	-5
△	1.1	0	2.49	4	NONE	0.5	5



b. Negative roll
Figure 48. Concluded.

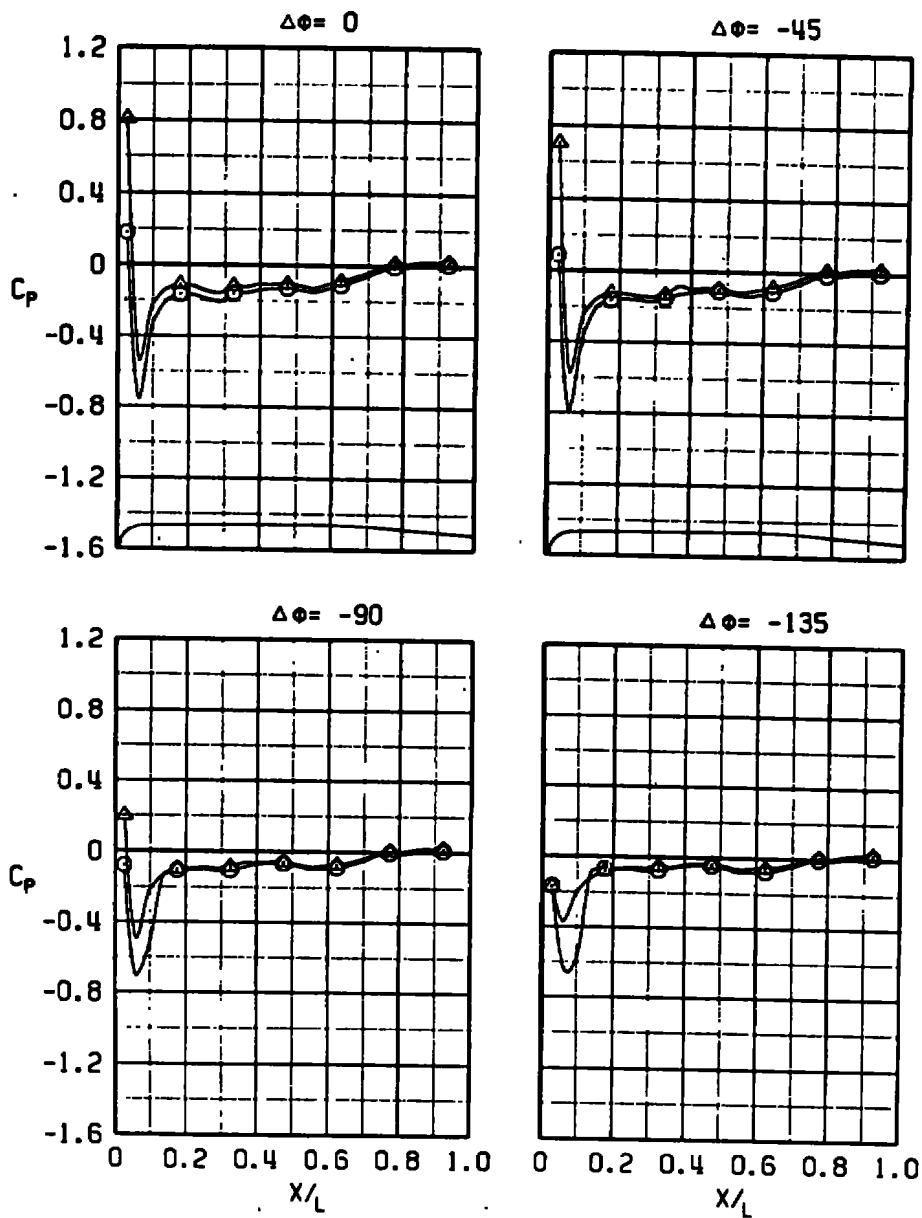
SYM	M_∞	α	$Re \times 10^{-6}$	CONF	FUSE	Z/D	$\Delta\theta$
○	0.5	-1	1.55	12	NONE	0.5	0
△	0.5	0	1.41	12	FMU-110	0.5	0



a. Positive roll

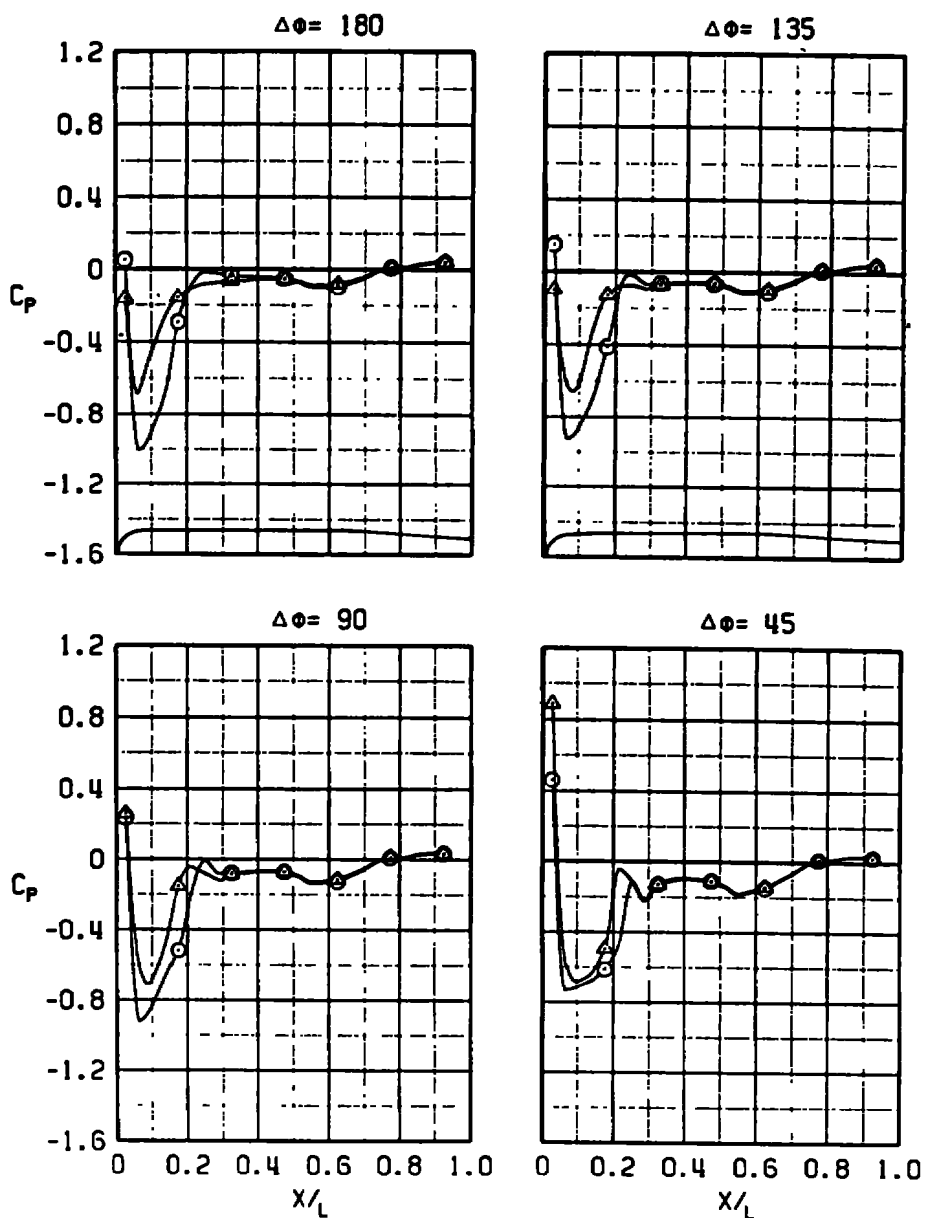
Figure 49. Effects of the FMU-110 fuse on the 12-in.-diam maximum volume bomb, $M_\infty = 0.5$.

SYM	M_∞	α	$Re \times 10^{-6}$	CONF	FUSE	Z/O	$\Delta\theta$
○	0.5	-1	1.55	12	NONE	0.5	0
△	0.5	0	1.41	12	FMU-110	0.5	0



b. Negative roll
Figure 49. Concluded.

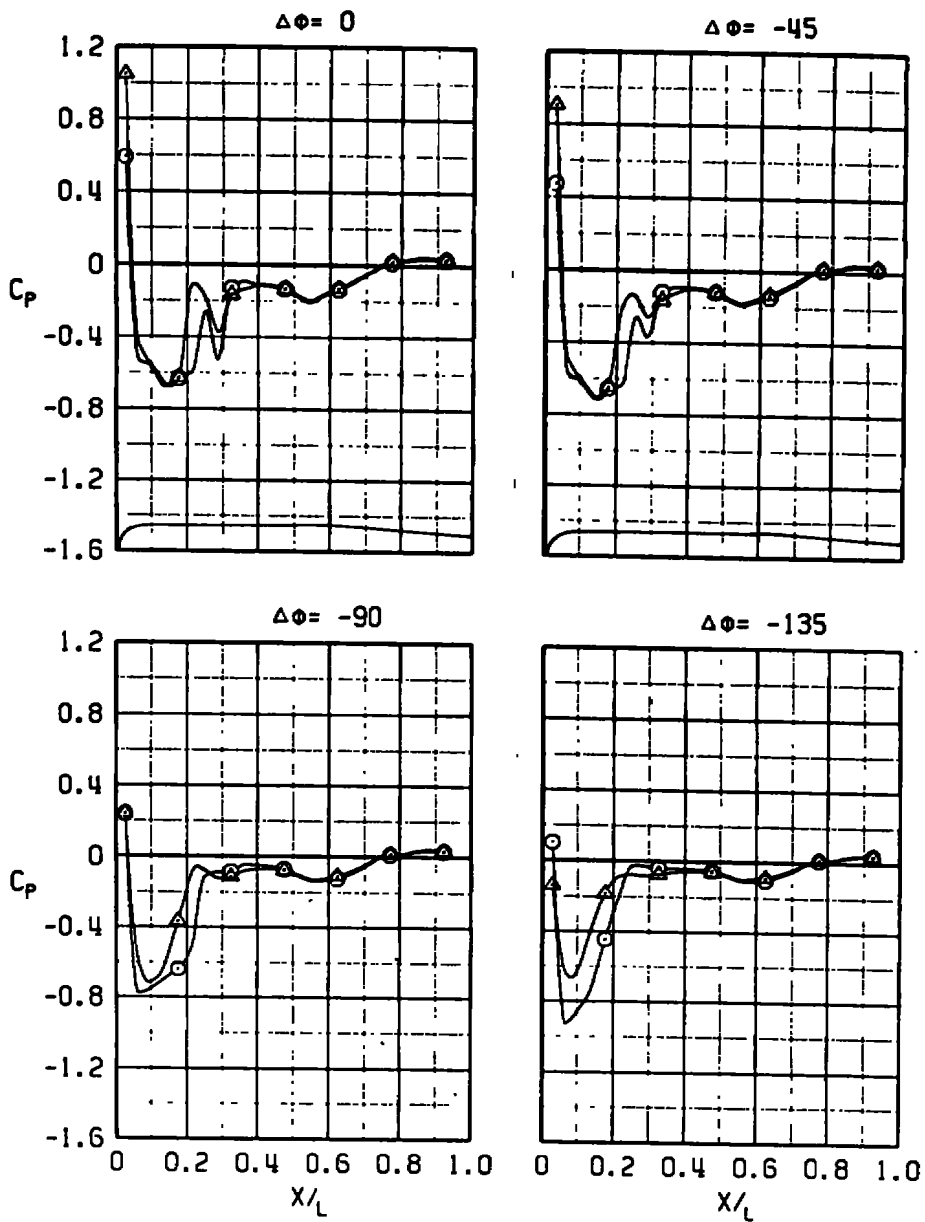
SYM	M_∞	α	$Re \times 10^{-6}$	CONF	FUSE	Z/D	$\Delta\theta$
○	0.9	0	1.99	12	NONE	0.5	0
△	0.9	0	2.04	12	FMU-110	0.5	0



a. Positive roll

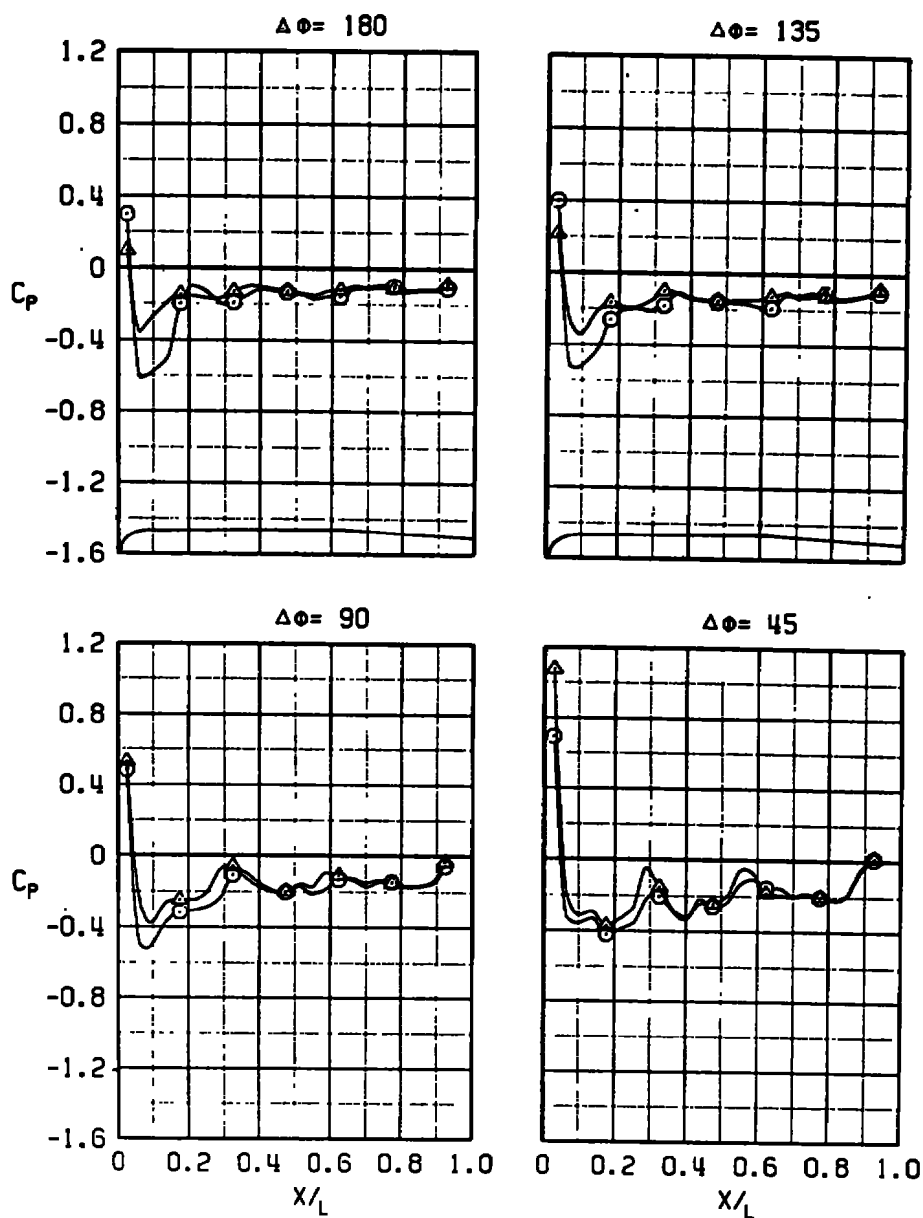
Figure 50. Effects of the FMU-110 fuse on the 12-in.-diam maximum volume bomb, $M_\infty = 0.9$.

SYM	M_∞	α	$Re \times 10^{-6}$	CONF	FUSE	Z/D	$\Delta\theta$
○	0.9	0	1.99	12	NONE	0.5	0
△	0.9	0	2.04	12	FMU-110	0.5	0



b. Negative roll
Figure 50. Concluded.

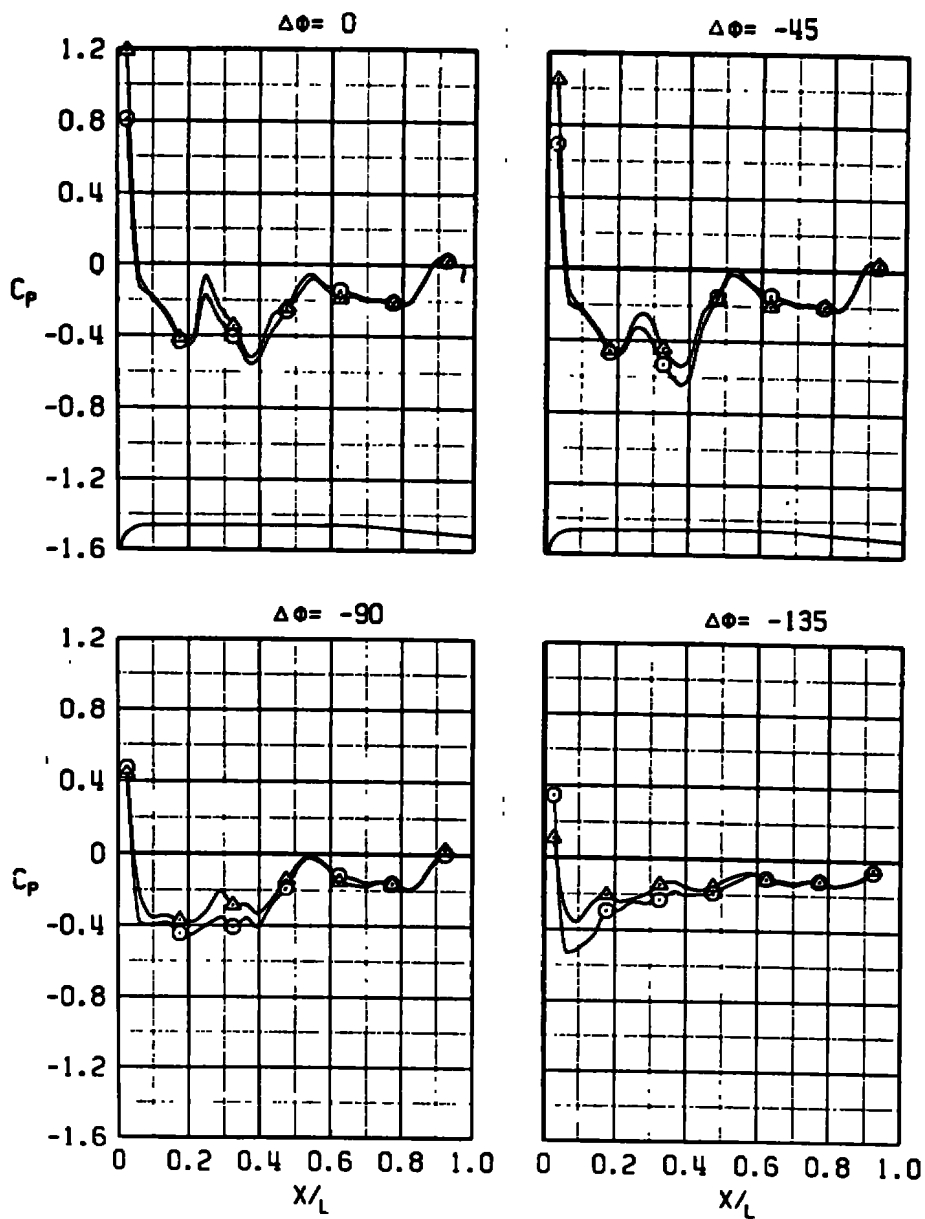
SYM	M_∞	α	$Re \times 10^{-6}$	CONF	FUSE	Z/D	$\Delta\theta$
○	1.1	0	2.23	12	NONE	0.5	0
△	1.1	0	2.25	12	FMU-110	0.5	0



a. Positive roll

Figure 51. Effects of the FMU-110 fuse on the 12-in.-diam maximum volume bomb, $M_\infty = 1.1$.

SYM	M_∞	α	$Re \times 10^{-6}$	CONF	FUSE	Z/D	$\Delta\theta$
○	1.1	0	2.23	12	NONE	0.5	0
△	1.1	0	2.25	12	FMU-110	0.5	0



b. Negative roll
Figure 51. Concluded.

Table 1. Store Trajectory Test Conditions

Config No.	Store Model	Fuse Type	Parent	M_∞	α , deg	Alt, ft	x_{cg} , ft
4	M-117 Standard	N/A	Wing-Pylon-TER	A	0	5000	32.88
6	M-117 Modified	N/A	↓	D	↓	↓	32.88
8	16-in. Max. Vol.	None	↓	B	↓	↓	30.00
10	14-in. Max. Vol.	↓	↓	C	↓	↓	32.88
10	14-in. Max. Vol.	↓	↓	E	↓	↓	20.88
12	12-in. Max. Vol.	↓	↓	A	↓	↓	32.88

Legend

A: $M_\infty = 0.5, 0.8, 0.9, 1.1, \text{ and } 1.3$
 B: $M_\infty = 0.5, 0.8, 0.9, \text{ and } 1.1$
 C: $M_\infty = 0.5, 0.8, \text{ and } 0.9$
 D: $M_\infty = 0.5 \text{ and } 0.8$
 E: $M_\infty = 0.9 \text{ and } 1.1$

Table 2. Aerodynamic Loads Test Conditions

Config No.	Store Model	Fuse Type	Parent	M_∞	α , deg	x_{cg} , deg	Store Position and Orientation	$\Delta\phi$, deg
1	M-117 Standard	N/A	Simulated TER	A	0	32.88	C	0
↓	↓	↓	Simulated TER	↓	5	↓	C	↓
3	↓	↓	Free Stream	N/A	↓	↓	D	↓
3	↓	↓	Wing-Pylon	0	↓	↓	C	↓
4	↓	↓	Wing-Pylon	5	↓	↓	↓	↓
4	↓	↓	Wing-Pylon-TER	0	↓	↓	↓	↓
4	↓	↓	↓	5	↓	↓	↓	↓
5	↓	↓	↓	0	↓	↓	↓	45
5	↓	↓	↓	5	↓	↓	↓	45
6	M-117 Modified	↓	↓	0	↓	↓	↓	0
↓	↓	↓	↓	5	↓	↓	C ⁺	↓
7	↓	↓	Free Stream	N/A	↓	↓	D	↓
7	↓	↓	Wing-Pylon-TER	0	↓	↓	C	45
8	16-in. Max. Vol.	None	↓	5	↓	↓	C ⁺⁺	45
↓	↓	None	↓	B	0	36.50	C	0
↓	↓	None	↓	A	5	↓	↓	↓
↓	↓	FMU-56	↓	0	↓	↓	↓	↓
↓	↓	FMU-56	↓	5	↓	↓	↓	↓
↓	↓	FMU-110	↓	0	↓	↓	↓	↓
↓	↓	FMU-110	↓	B	5	↓	↓	↓
↓	↓	None	Free Stream	A	N/A	↓	D	↓
10	14-in. Max. Vol.	↓	Wing-Pylon-TER	0	↓	↓	C	↓
↓	↓	↓	↓	5	↓	↓	↓	↓
↓	↓	FMU-56	↓	0	↓	↓	↓	↓
↓	↓	FMU-56	↓	5	↓	↓	↓	↓
↓	↓	FMU-110	↓	0	↓	↓	↓	↓
↓	↓	FMU-110	↓	5	↓	↓	↓	↓
↓	↓	None	Free Stream	N/A	↓	↓	D	↓
11	↓	↓	Wing-Pylon-Ter	0	↓	↓	C	45
11	↓	↓	↓	5	↓	↓	↓	45
12	12-in. Max. Vol.	↓	↓	0	35.00	↓	↓	0
↓	↓	↓	↓	5	↓	↓	↓	↓
↓	↓	FMU-56	↓	0	↓	↓	↓	↓
↓	↓	FMU-56	↓	5	↓	↓	↓	↓
↓	↓	FMU-110	↓	0	↓	↓	↓	↓
↓	↓	↓	Free Stream	5	↓	↓	D	↓
↓	↓	↓	↓	N/A	↓	↓	↓	↓

Legend
 A: $M_\infty = 0.5, 0.8, 0.9, 1.1, \text{ and } 1.3$
 B: $M_\infty = 0.5, 0.8, 0.9, \text{ and } 1.1$
 C: $Z/D = 0$ at $\Delta\theta = 0$, and $Z/D = 0.5$ and 1.0 at $\Delta\theta = -5, 0, \text{ and } 5$ deg
 D: $\alpha = -20$ to 20 deg in 4 -deg increments
 + Carriage Position only, at $M_\infty = 1.3$
 ++ Carriage Position only, at $M_\infty = 1.1$ and 1.3

Table 3. Aerodynamic Pressure Test Conditions

Config No.	Store Model	Fuse Type	Parent	M _∞	α, deg	X _{cg} , ft	Store Position and Orientation	Δφ, deg
1	M-117 Standard	N/A	Simulated TER	0.5	0	32.88	C	G
↓	↓	↓	↓	0.5	5	↓	↓	↓
↓	↓	↓	↓	0.8	0	↓	↓	↓
↓	↓	↓	↓	0.8	5	↓	↓	↓
↓	↓	↓	Free Stream	A	N/A	↓	N/A	↓
2	↓	↓	TER	0.5	0	↓	C	↓
↓	↓	↓	↓	0.5	5	↓	C	↓
↓	↓	↓	↓	0.8	0	↓	D	↓
↓	↓	↓	↓	0.8	5	↓	↓	↓
↓	↓	↓	↓	1.1	0	↓	↓	↓
↓	↓	↓	↓	1.1	5	↓	↓	↓
↓	↓	↓	↓	1.3	0	↓	F	↓
↓	↓	↓	↓	1.3	5	↓	D	↓
3	↓	↓	Wing-Pylon	B	0	↓	↓	↓
↓	↓	↓	↓	B	5	↓	↓	↓
↓	↓	↓	↓	1.3	0	↓	Carr. Pos.	↓
4	↓	↓	Wing-Pylon-TER	A	0	↓	D	↓
↓	↓	↓	↓	0.5	5	↓	↓	↓
↓	↓	↓	↓	0.8	↓	↓	↓	↓
↓	↓	↓	↓	0.9	↓	↓	↓	↓
6	M-117 Modified	↓	↓	A	0	↓	↓	↓
↓	↓	↓	↓	↓	5	↓	↓	↓
↓	↓	↓	Free Stream	↓	N/A	↓	N/A	↓
8	16-in. Max. Vol.	None	Wing-Pylon-TER	0	↓	36.50	E	↓
↓	↓	None	↓	5	↓	↓	↓	↓
↓	↓	FMU-56	↓	0	↓	↓	↓	↓
↓	↓	↓	↓	0.5	5	↓	↓	↓
↓	↓	↓	↓	0.8	5	↓	↓	↓
↓	↓	FMU-110	↓	A	0	↓	↓	↓
↓	↓	None	Free Stream	A	N/A	↓	N/A	↓
↓	↓	FMU-110	↓	0.5	↓	↓	↓	↓
↓	↓	FMU-110	↓	1.1	↓	↓	↓	↓
10	14-in. Max. Vol.	None	Wing-Pylon-TER	A	0	↓	E	↓
↓	↓	None	↓	↓	5	↓	↓	↓
↓	↓	FMU-56	↓	↓	0	↓	↓	↓
↓	↓	↓	↓	0.5	5	↓	↓	↓
↓	↓	↓	↓	0.8	5	↓	↓	↓

Table 3. Concluded

Config No.	Store Model	Fuse Type	Parent	M_∞	α , deg	x_{cg} , ft.	Store Position and Orientation	$\Delta\phi$, deg
10	14-in. Max. Vol.	FMU-110	Wing-Pylon-TER	A	0	36.50	E	G
				0.5	5			
				0.8				
				0.9				
				1.1			Carr. Pos.	
				1.3			E	
		None	Free Stream	A	N/A		N/A	
		FMU-56		0.5				
				0.9				
				1.1				
		FMU-110		0.5				
				0.9				
				1.1				
12	12-in. Max. Vol.	None	Wing-Pylon-TER	A	0	35.00	E	
				0.5	5		Carr. Pos.	
				0.8			E	
				0.9				
				1.1				
				1.3				
		FMU-56		A	0			
		FMU-56		A	5			
		FMU-110		0.5	0			
				0.8			Carr. Pos.	
				0.9			E	
				1.1			E	
		None	Free Stream	A	N/A		N/A	

Legend: A: $M_\infty = 0.5, 0.8, 0.9, 1.1$, and 1.3
 B: $M_\infty = 0.5, 0.8, 0.9$, and 1.1
 C: $Z/D = 0$ at $\Delta\theta = 0$, and $Z/D = 0.5$ and 1.0 at $\Delta\theta = -5, 0$, and 5 deg
 D: $Z/D = 0$ at $\Delta\theta = 0$, and $Z/D = 0.5$ at $\Delta\theta = -5, 0$, and 5 deg
 E: $Z/D = 0$ at $\Delta\theta = 0$, and $Z/D = 0.5$ at $\Delta\theta = -5$ and 0 deg
 F: $Z/D = 0.5$ and $\Delta\theta = -5, 0$, and 5 deg
 G: $\Delta\phi = 180$ to -135 deg in 45 -deg increments (At zero roll orientation, the pressure orifices along the model were in the $x_p - z_p$ plane with the orifices adjacent to the pylon or TER, position number one, surface.)

Table 4. Identification of Full-Scale Store Parameters

Parameter	M-117 Standard and Modified	16-in.-diam Maximum Volume	14-in.-diam Maximum Volume	12-in.-diam Maximum Volume
S	1.396	1.396	1.069	0.785
b	1.333	1.333	1.1667	1.00
\bar{m}	23.31	24.865	19.426	14.453
I_{xx}	4	4	2.5	1.5
I_{yy}	50	65	50	35
I_{zz}	50	65	50	35
I_{xz}	0	0	0	0
x_{cg}	32.88	See A	See A	See A
$C_{\ell p}$	0	-0.73	-1.13	-1.93
C_{mq}	-70	See B	See B	See B
C_{nr}	-70	See B	See B	See B
F_z	1200	1200	1200	1200
x_L	0	0	0	0
z_E	0.255	0.255	0.255	0.255

Legend A: x_{cg} Values Given in Tables 1 through 3

B:	Store	M_{∞}	C_{mq}	C_{nr}
	16-in.-diam	0.5, 0.8, 0.9	-30	-30
	↓	1.1	-56	-56
	↓	1.3	-80	-80
	14-in.-diam	0.5, 0.8, 0.9	-44	-44
	↓	1.1	-84	-84
	↓	1.3	-113	-113
	12-in.-diam	0.5, 0.8, 0.9	-58	-58
	↓	1.1	-112	-112
	↓	1.3	-146	-146

NOMENCLATURE

BL	Aircraft buttock line from plane of symmetry, in., model scale
b	Store reference dimension, ft, full scale
C_A	Store axial-force coefficient, axial force/ $q_\infty S$
C_ℓ	Store rolling-moment coefficient, rolling moment/ $q_\infty S b$
C_{ℓ_p}	Store roll-damping derivative, $dC_\ell/d(pb/2V_\infty)$
C_m	Store pitching-moment coefficient, referenced to the store cg, pitching moment/ $q_\infty S b$
C_{m_q}	Store pitch-damping derivative, $dC_m/d(qb/2V_\infty)$
C_N	Store normal-force coefficient, normal force/ $q_\infty S$
C_n	Store yawing-moment coefficient, referenced to the store cg, yawing moment/ $q_\infty S b$
C_{n_r}	Store yaw-damping derivative, $dC_n/d(rb/2V_\infty)$
C_p	Local pressure coefficient, $(p_\ell - p_\infty)/q_\infty$
C_Y	Store side-force coefficient, side force/ $q_\infty S$
FS	Aircraft fuselage station, in., model scale
F_Z	TER ejector force, lb
I_{xx}	Full-scale moment of inertia about the store X_B axis, slug-ft ²
I_{xz}	Full-scale product of inertia, X_B - Z_B axis, slug-ft ²
I_{yy}	Full-scale moment of inertia about the store Y_B axis, slug-ft ²
I_{zz}	Full-scale moment of inertia about the store Z_B axis, slug-ft ²
L	Length of the store\ model, in.
M_∞	Free-stream Mach number
\bar{m}	Full-scale store mass, slugs

p	Store angular velocity about the X_B axis, radians/sec
p_l	Local pressure measured at the model orifices, psfa
p_∞	Free-stream static pressure, psfa
q	Store angular velocity about the Y_B axis, radians/sec
q_∞	Free-stream dynamic pressure, psf
r	Store angular velocity about the Z_B axis, radians/sec
S	Store reference area, ft ² , full scale
t	Real trajectory time from initiation of trajectory, sec
V_∞	Free-stream velocity, ft/sec
X	Distance from nose of store model to location of a pressure orifice, measured parallel to the model axis, in.
X_{cg}	Full-scale cg location, ft from nose of store
X_L	Ejector piston location relative to the store cg, positive forward of store cg, ft, full scale
X_P	Separation distance of the store cg parallel to the pylon axis system X_P direction, ft, full scale measured from the prelaunch position
Y_P	Separation distance of the store cg parallel to the pylon axis system Y_P direction, ft, full scale measured from the prelaunch position
Z_P	Separation distance of the store cg parallel to the pylon-axis system Z_P direction, ft, full scale measured from the prelaunch position
Z_E	Ejector stroke length, ft, full scale
Z/D	Nondimensionalized separation distance of the store cg parallel to the pylon-axis system Z_P direction, Z_P /store diameter
α	Store, pylon, or TER model angle of attack relative to the free-stream velocity vector, deg

- $\Delta\theta$ Angle between the store longitudinal axis and its projection in the X_P - Y_P plane, positive when store nose is raised as seen by pilot, deg
- $\Delta\phi$ Angle between the projection of the store lateral axis in the Y_P - Z_P plane and the Y_P axis, positive for clockwise rotation when looking upstream, deg
- $\Delta\psi$ Angle between the projection of the store longitudinal axis in the X_P - Y_P plane and the Y_P axis, positive when the store nose is to the right as seen by the pilot, deg

PYLON-AXIS SYSTEM COORDINATES

Directions

- X_P Parallel to the store longitudinal axis in the carriage position, positive direction is forward as seen by the pilot
- Y_P Perpendicular to the pylon or TER plane of symmetry, positive is to the right as seen by the pilot
- Z_P Perpendicular to both the X_P and Y_P axes, positive is down as seen by the pilot

The pylon-axis system origin is coincident with the store cg in the carriage position. Both the origin and the direction of the coordinate axes remain fixed with respect to the pylon or TER.

STORE BODY-AXIS SYSTEM COORDINATES

Directions

- X_B Parallel to the store longitudinal axis, positive direction is upstream in the prelaunch position
- Y_B Perpendicular to the store longitudinal axis, and parallel to the pylon-axis system X_P - Y_P plane when the store is at zero roll angle, positive direction is to the right looking upstream when the store is at zero yaw and roll angles
- Z_B Perpendicular to both the X_B and Y_B axes, positive direction is downward as seen by the pilot when the store is at zero pitch and roll angles.

The store body-axis system origin is coincident with the store cg and moves with the store during separation from the parent airplane. The X_B , Y_B , and Z_B coordinate axes rotate with the store in pitch, yaw, and roll so that mass moments of inertia about the three axes are not time-varying quantities.